Czech Technical University in Prague
Faculty of Mechanical Engineering
Department of Mechanics, Biomechanics and Mechatronics

PHENOMENOLOGICAL MODELS FOR LIFETIME PREDICTION UNDER LOW-CYCLE FATIGUE AND THERMO-MECHANICAL FATIGUE LOADING CONDITIONS

by

Ing. Michal BARTOŠÁK

Doctoral Study Programme: Mechanical Engineering
Study Field: Mechanics of Rigid and Deformable Bodies and Environment

Supervisor: *Doc. Ing. Miroslav ŠPANIEL, CSc.*

A thesis submitted to
the Faculty of Mechanical Engineering, Czech Technical University in Prague,
in partial fulfilment of the requirements for the degree of Doctor.

Prague, March 2019

Thesis Supervisor:
Doc. Ing. Miroslav Španiel, CSc.
Department of Mechanics, Biomechanics and Mechatronics
Faculty of Mechanical Engineering
Czech Technical University in Prague
Technická 4
166 07 Prague 6
Czech Republic

Abstract

This works presents original research data for low-cycle fatigue and thermo-mechanical fatigue of SiMo 4.06 cast iron. The cast iron was subjected to a various strain rates and strain amplitudes in the temperature range of 20°C-750°C under low-cycle fatigue and thermo-mechanical fatigue loading conditions. The experiments were carried out on the newly in-house designed test stand for performing uniaxial low-cycle and thermo-mechanical fatigue tests. A unified viscoplastic material is implemented by the means of user defined material subroutine for Abaqus commercial finite element software. The anisothermal multiaxial formulation of unified viscoplastic material model used here is based on hyperbolic sine flow rule and the model incorporates isotropic hardening and non-linear kinematic hardening. The model is calibrated systematically with temperature on the basis of obtained experimental data. A new method is applied in order to calibrate the temperature dependent viscoplastic material model parameters. Numerical simulations of cyclic mechanical behaviour of SiMo 4.06 follows. Finally, a novel energy based fatigue criterion is proposed in order to take into account effect of mean stress, which usually appears during thermo-mechanical loading. A good correlation was achieved between the predicted results and the observed results.

Keywords:
viscoplasticity, thermo-mechanical fatigue, low-cycle fatigue, dissipated energy

Abstrakt

Tato disertační práce dokumentuje původní výsledky výzkumu nízkocyklové a teplotně-mechanické únavy tvárné litiny SiMo 4.06. Byly provedeny rozsáhlé mechanické zkoušky tohoto materiálu pro různé rychlosti a hladiny amplitud deformace, pro teploty v rozsahu 20°C-750°C. Mechanické zkoušky byly provedeny na nově navrženém zkušebním zařízení, které je určeno pro jednoosé zkoušky nízkocyklové a teplotně-mechanické únavy. Dále byl implementován unifikovaný viskoplastický materiálový model jako uživatelská funkce pro konečně-prvkový řešič Abaqus. Unifikovaný materiálový model je implementován pro případ multiaxiálního zatěžování za předpokladu proměnné teploty, konstitutivní vztah pro funkci tečení je založen na hyperbolickém sinu, model zahrnuje isotropní i nelineární kinematické zpevnění. Kalibrace modelu je provedena pro získané experimentální výsledky. Teplotně závislé parametry modelu jsou kalibrovány systematicky s využitím nových postupů. Zkalibrovaný materialový model je použit pro numerické simulace cyklického mechanického chování zkoumaného materiálu. Nakonec je navrženo nové kritérium pro hodnocení životnosti při nízkocyklové teplotně-mechanické únavě. Navržené kritérium je založeno na disipované hysterezní energii a zahrnuje vliv středního napětí, které je často pozorováno během mechanických zkoušek prováděných za proměnných teplot. Výsledky simulací dobře korelují s výsledky z experimentů.

Klíčová slova:
viskoplasticita, teplotně-mechanická únava, nízkocyklová únava, disipovaná energie

Acknowledgements

This work was supported by the ESIF, EU Operational Programme Research, Development and Education, and from the Center of Advanced Aerospace Technology (CZ.02.1.01/0.0/0.0/16_019/0000826), Faculty of Mechanical Engineering, Czech Technical University in Prague. The work also received support from the Technology Agency of the Czech Republic, grant No. TE01020020, and support from the Grant Agency of the Czech Technical University in Prague, grant No. SGS15/187/OHK2/3T/12.

Declaration

I hereby declare that I am the sole author of this dissertation thesis and that I have not used any sources other than those listed in the bibliography and identified as references.

.....

Ing. Michal Bartošák

March 2019

Contents

List of Figures

List of Tables

Nomenclature

Symbol	Description	Units
β	viscous material parameter	MPa^{-1}
x	backstress	MPa
α	viscous material parameter in Chapter 6; fatigue material parameter in Chapter 7	s^{-1}; $J \cdot mm^{-3}$
$\boldsymbol{\sigma}$	stress tensor	MPa
$\boldsymbol{\varepsilon}$	strain tensor	-
$\boldsymbol{\varepsilon}^e$	elastic strain tensor	-
$\boldsymbol{\varepsilon}^{pl}$	inelastic strain tensor	-
$\boldsymbol{E}$	fourth order elasticity tensor	-
$\boldsymbol{I}$	identity matrix	-
$\boldsymbol{s}$	deviatoric stress tensor	MPa
$\boldsymbol{x}$	backstress tensor	MPa
$\Delta\varepsilon$	axial strain range	-
$\dot{\sigma}$	axial stress rate	$MPa \cdot s^{-1}$
$\dot{\varepsilon}$	axial strain rate	s^{-1}
γ_i	kinematic hardening parameter	-
λ	Lame's constant	MPa
ν	Poisson's ratio	-
Ω	dissipation potential	MPa
σ	axial stress	MPa
σ_v	viscous part of stress	MPa
$\tilde{w}$	modified dissipated energy per loading cycle	$J \cdot mm^{-3}$
ε	axial strain	-
ε_a	axial strain amplitude	-
ε_m, ε_{mech}	mechanical strain	-

ε_{th}	thermal strain	-
ε_t	total strain	-
C_i	kinematic hardening parameter	MPa
E	elastic modulus	MPa
f	stress function	MPa
G	shear modulus	MPa
K	bulk modulus	MPa
k	initial yield stress	MPa
N_f	number of cycles to failure	-
p	effective viscoplastic (inelastic) strain	-
R	isotropic hardening function	MPa
R^2	coefficient of determination	-
R_σ	stress ratio	-
R_ε	strain ratio	-
T	temperature	$°C$
t	time	s
t_h	hold time	s
w	dissipated energy per loading cycle	$J \cdot mm^{-3}$

Abbreviation Description

FEA Finite Element Analysis

FEM Finite Element Method

HCF High-Cycle Fatigue

IP-TMF In-Phase Thermo-Mechanical Fatigue

LCF Low-Cycle Fatigue

OP-TMF Out-of-Phase Thermo-Mechanical Fatigue

SiMo Silicon-Molybdenum

TMF Thermo-Mechanical Fatigue

UMAT User Material Subroutine

Chapter 1

Introduction

Mechanical components are subjected to variable service conditions during their lifetime including start-up, stop, load, partial load and shut-down phases. Mechanical loading and temperature usually changes during the component service life. Repeated cyclic mechanical loading or static (over)loading may ultimately lead to a component to failure. Failure under cyclic mechanical loading is generally known as a fatigue failure. Fatigue failure mechanism is connected with cumulative damage in material, which is caused by the individual loading cycles. The time varying cyclic loading of the component can be deterministic or stochastic. It's widely accepted that damage for each individual loading cycle is treated separately with the use of signal decomposition methods such as rainflow method. Fatigue damage cumulation can be linear or non-linear. Linear fatigue damage cumulation (Palmgren-Miner hypothesis) is most frequently used for the fatigue life prediction of metal materials. The fatigue is referred to as Low-Cycle Fatigue (LCF) or High-Cycle Fatigue (HCF). The difference between LCF and HCF can be explained in the terms of mechanical deformation. LCF is governed by reverse plastic deformation mechanism (i.e. cyclic inelastic strain), whereas HCF is characterized by cyclic elastic strain. However, even for HCF, plastic deformation may occur, e.g. in notches, but the elastic deformation is still governing the component or specimen volume. The terms Low- and High- also means that number of cycles to failure is lower for LCF than for HCF. In the case of LCF number of cycles to failure is usually below 10^4, while for HCF it is typically above 10^6, however this is strongly related to the properties of the investigated material. Stress or strain amplitude of the loading versus number of cycles to failure (for this level of loading) is often plotted versus number of cycles to failure, i.e. strain-life or stress-life curve, respectively. Stress-life curve is also known as Basquin or Wöhler curve, while strain-life curve is referred to as Manson-Coffin-Basquin curve.

LCF and Thermo-Mechanical Fatigue (TMF) are usually caused by the start-up and stop phases during the service life of a high-temperature component. In addition, long dwell periods, which can occur during service life, may lead to effects such as a creep and a relaxation. The relaxation of stress and creep are both thermally dependent and thermally activated processes. The relaxation of stress usually occurs at moderate and high temperature during the strain hold period, relaxation can be referred to as a creep

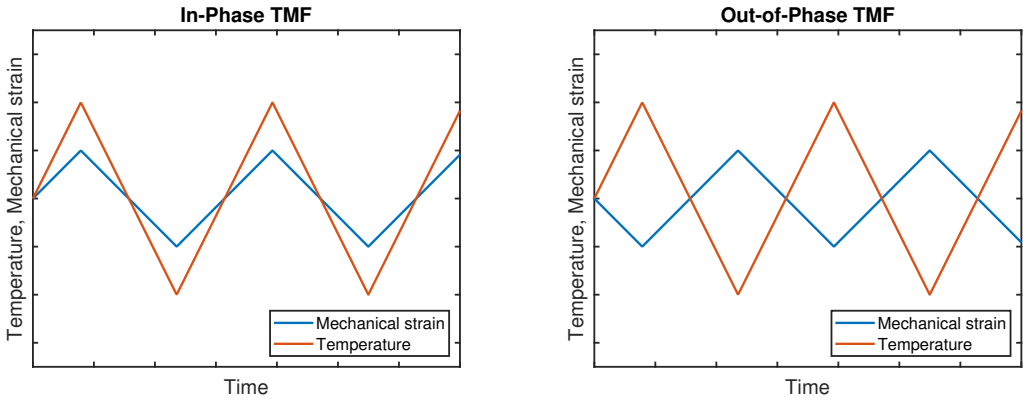

(a) (b)

Figure 1.1: Temperature and mechanical strain waveforms for in-phase (a) and out-of-phase (b) thermo-mechanical fatigue.

under varying stress. TMF and LCF are both characterized by cyclic and usually time-dependent inelastic strains and stresses. If the temperature changes significantly during the loading cycle, TMF should be considered for life assessment, whereas LCF can be used for loading cycles with constant temperature. TMF is caused primarily by cyclic thermal loading and additional mechanical loading. The thermal loading is caused by inhomogeneous temperature fields and kinematic boundary conditions of the component that constrain thermal expansion and contraction and lead to inelastic time-dependent strains and stresses. In combination with additional mechanical loading, this result in component failure after several loading cycles. The TMF cycle is usually characterized by the phase between mechanical and thermal strain, primarily in-phase and out-of phase TMF tests, Figs. 1.1a and 1.1b, respectively. High temperature LCF and TMF are important consideration in design phases of components in the course of variable service conditions, such as turbine housing of turbocharger, turbines, exhaust manifold, aircraft engine parts or fossil power-plant components. Reliable life prediction method is necessary in order to avoid over-dimensioning, and in order to guarantee functionality and safety of these components during their service life.

The classical strain-life approach often used for the life prediction of components subjected to LCF is generally not a reliable method for TMF life predictions, since there are changes in temperature during the loading cycle. The mechanical response of material and the strain-life curves are temperature dependent. In the case of TMF loading conditions, this leads to positive mean stress for an out-of-phase loading cycle or to negative mean stress for an in-phase cycle. The changes in temperature during the TMF loading cycle and the positive mean stress can result in considerably shorter life in comparison with LCF for equivalent amplitude of loading and for maximal or minimal temperature of the TMF loading cycle. The reliable LCF/TMF life prediction method for complex components,

i.e. components under complex loading conditions and components complex in geometry, should consist from following parts:

- Strain-controlled LCF and TMF experimental program for specimens manufactured from the investigated material,
- Constitutive material model derived from the material testing,
- Finite element analysis of the investigated component,
- Fatigue analysis of the component.

This work is structured as follows. First, current state of the problem is discussed in Chapter 2. This chapter consist of three section, where are discussed high temperature LCF and TMF experiments. Next, the overview of commonly used constitutive material models in terms of LCF and TMF is given. Finally, damage models for high temperature LCF and TMF are discussed in detail in this chapter.

Next, a brief overview of the methods that are used in the next chapters can be found in Chapter 3. Aims of the thesis, which were chosen on the basis of the conclusions of Chapter 2, are given in Chapter 4.

The original experimental data that were obtained for uniaxially loaded specimens are presented in Chapter 5. The experiments were performed on the newly in-house designed test stand at CTU in Prague, which can be used for LCF and TMF tests. Material of the specimens studied here is silicon-molybdenum cast iron (SiMo 4.06), which is used in the automotive industry for the production of turbine housings of a turbocharger and exhaust manifolds. The experimental data set consists of triangular LCF tests that were performed under variable mechanical strain rates and amplitudes, LCF test with hold time in tension and out-of-phase TMF tests. The uniaxial tests on specimens were performed for temperatures between 20°C and 750°C.

In Chapter 6, a unified viscoplastic constitutive material model is chosen on the basis of observed experimental results. The material model is calibrated in the selected temperature range on the basis of isothermal triangular LCF tests with and without hold time. A novel method for systematic calibration of temperature dependent material model parameters is proposed. From a practical point of view, the constitutive material model is implemented as user material subroutine (UMAT) for Abaqus commercial finite element software. An implicit integration of the constitutive equations is chosen and consistent material tangent stiffness is analytically derived on the basis of the used implicit integration scheme. Consistent material tangent stiffness is essential for time effective numerical simulation of large engineering problems using finite element method.

A novel fatigue criterion that is proposed on the basis of the observed lifetime behaviour of SiMo 4.06 is presented in Chapter 7. The proposed fatigue criterion can be used for LCF and TMF life prediction of complex engineering components. The criterion is based on the hysteresis energy, which is dissipated during the LCF or TMF loading cycle, the dissipated hysteresis energy is modified in order to take into account effect of changing

temperature during the loading cycle, which is observed by the means of positive mean stress for OP-TMF.

The theoretical and practical outcomes of the thesis, which can be used by other researchers and in industry, are described in Chapter 8. Finally, conclusions and possible topics for future research are given in Chapter 9.

Chapter 2

State of the art

2.1 Experimental approaches to LCF and TMF

LCF and TMF loading conditions are usually simulated on specimens under uniaxial or multiaxial loading. It's widely accepted that LCF and TMF tests are performed under strain control. LCF tests are usually triangular in order to keep constant strain rate over the loading cycle. This is particularity important at high temperatures, so that constant value of so-called viscous stress is generated throughout the loading cycle. Creep and plasticity interaction can be observed during the triangular LCF tests with hold time that can be in tension, or in compression or in both, these tests are also known as fatigue-creep tests, because creep is observed in the form of relaxation of stress during the dwell time. Triangular LCF tests with and without hold time are important for calibration of constitutive material models that are used to predict cyclic mechanical behaviour of the investigated material. TMF tests, which can be in-phase, out-of-phase or in different phase, can be triangular, but that is not so important as it's for LCF tests. The speed and shape of temperature waveform during the TMF loading cycle may be limited by the used method for heating and cooling of the specimens. Usually, induction heating or direct resistance heating is applied, active cooling of a specimen can be achieved, for example, by forced air blowing. High temperature extensometer with ceramic rods is most commonly used for strain control during LCF and TMF loading cycles. The temperature is usually measured by a thermocouple, pyrometry is not reliable method due to the changes in specimen surface that are caused by oxidation during the loading cycles [9, 37]. Thermocouple is usually spotwelded to the specimen or ribbon-typed to the specimen [9, 37]. Moreover, TMF and LCF tests should be maintained so that temperature and strain are uniform in the specimen gauge section, so that the area enclosed by extensometer rods represents material point under uniform loading conditions. High temperature LCF and especially TMF test conditions were discussed and described in detail in [37]. Generally, TMF tests require more expensive test stands in comparison with LCF. TMF test can be performed for different phasing between temperature and mechanical strain. Assuming uniaxial loading

conditions, the total strain, ε_t, which is measured by extensometer, is sum of mechanical strain, ε_{mech}, and thermal strain, ε_{th}:

$$\varepsilon_t = \varepsilon_{th} + \varepsilon_{mech} = \alpha_{th} (T - T_0) + \varepsilon_{mech}, \tag{2.1}$$

where T is temperature and T_0 is a reference temperature. The secant coefficient of thermal expansion, α_{th}, should be estimated before running TMF test in order to separate the mechanical and thermal strain during the TMF loading cycle, this should be done during the measurements preceding the test, i.e. by heating and cooling of specimen with zero load force.

Typical evolution of the global load with number of cycles for cyclic softening during strain-controlled isothermal LCF test is presented in Fig. 2.1. According to Skelton [79], the evolution shows three important phases that are defined by the stabilization point, N_{sta}, tangent point, N_{tan}, and final point, N_{fin}. The stabilization phase is defined until N_{sta} cycles, during this phase specimen is subjected to a plastic shakedown. After N_{sta} cycles, material behaviour is more or less stabilized until reaching N_{tan}, when existing cracks reach a macroscopic length scale and become mechanically important. Failure usually occurs at N_{fin} after reaching a small number of cycles after N_{tan}. In order to evaluate lifetime, the end life criterion [37] is usually defined as 5% or 10% decrease in maximal load of the cycle in comparison with the load observed at N_{tan} or at mid-life, which can be calculated as mean value from N_{sta} and N_{tan}. The number of cycles to failure is usually referred to as N_f.

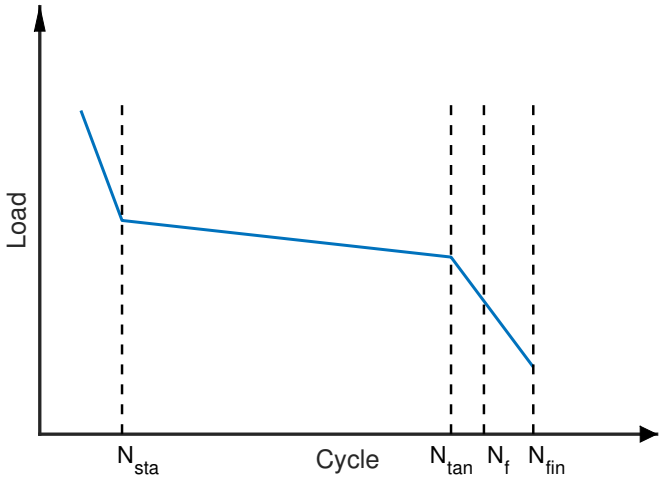

Figure 2.1: Evolution of the maximum global load of the cycle with number of cycles.

Great progress has been achieved in recent decades in the experimental investigations of metal materials mechanical behaviour under high temperature LCF and TMF loading conditions. Tabibian et al. [82] compared behaviour of lost foam cast aluminium alloy

in aged and not-aged condition during LCF and TMF tests. Beck et al. [8] studied behaviour of Inconel superalloy under LCF and TMF loading. Heat resistant austenitic Sanicro 25 steel behaviour under OP-TMF and IP-TMF loading was studied by Petráš et al. [71]. Wu et al. [85] studied TMF behaviour of cast iron in temperature range up to 800°C. Guth et al.[35] investigated effect of hold time TMF life of nickel superalloy, it was shown that the dwell period decreased significantly lifetime under IP-TMF and OP-TMF loading. Other interesting finding was that gauge length may exhibit transverse creep deformation under action of the force applied by the extensometer rods during compressive dwell times in OP TMF tests. Influence of hold time on fatigue behaviour of Inconel 718 superalloy was studied in [34, 55]. Brookes et al. [14] studied TMF behaviour of TiAl alloy under non-propotional thermo-mechanical loading, it was found that the non-proportional axial–torsional OP TMF test lead to shortest lifetimes in comparison with mechanically and thermally in-phase tests. LCF and TMF behaviour of 316L stainless steel between 300–650°C was studied by Nagesha et al. [57]. Norman et al. [66] studied behaviour of three different types of silicon-molybdenum cast iron, which are used for manufacturing exhaust manifolds.

2.2 Constitutive models used for LCF and TMF

A suitable constitutive material model derived from material testing creates substantial part of the life prediction methods for high temperature LCF and TMF. High temperature components are often subjected to a great temperature changes during their lifetime, for example, exhaust manifold operates between -20°C - 800°C [29]. A constitutive model used for accurate and reliable predictions of strain and stress fields should take into account change of mechanical properties for the investigated material that are observed with temperature. Mechanical behaviour of most metal material is purely elastic-plastic at room temperature, whereas considerable time-dependent behaviour can be observed at moderate temperatures, while the mechanical behaviour is almost purely viscous at high temperatures. It is generally accepted that viscoplastic material model is capable of describing such changes in the mechanical behaviour. Viscoplastic constitutive material models are often divided into two groups, unified and non-unified viscoplastic material models. Non-unified viscoplastic material models partition creep strain and plastic strain and treat them separately [48]. Non-unified models have been subject of research for several authors, e.g. [17, 30, 45, 56]. Advantage of this kind of material models is fast and easy calibration from experimental data, for example these models can be calibrated from tensile tests and creep rupture tests. Disadvantages of non-unified viscoplastic material models are such that they not well suited for cyclic loading conditions, and also the use of such models often leads to convergence issues during the simulations of cyclic loading. Further, the ratcheting prediction may be inaccurate [2, 31]. The development of non-unified models can be attributed to a lack of experimental data that show creep and fatigue interaction [24]. In contrast, unified viscoplastic constitutive material models do not partition creep and plasticity, but consider them in single quantity referred to as inelastic strain, i.e. viscoplastic strain, as

they occur simultaneously [22, 24, 48]. A unified viscoplastic model can be used to obtain response of materials under complex cyclic loading conditions and for monotonic loading conditions, such as the creep, thermo-mechanical fatigue, isothermal LCF with dwell times or under isothermal LCF with different strain rates. The viscoplastic strain rate is determined by the chosen flow rule, which allow to take time-dependent viscoplastic effects into account, i.e. the creep, the relaxation of stress or the strain rate sensitivity. The unified constitutive material models are well suited for modelling viscoplastic behaviour of metal materials subjected to cyclic loading conditions.

Phenomenological constitutive material models for describing viscoplastic or plastic behaviour of metals are usually based on isotropic and kinematic hardening rules. Furthermore, associated flow rule and von Mises yield surface are usually assumed. Isotropic hardening allows elastic domain to expand or contract in dependence on accumulated inelastic strain or other internal variable of the model, so that cyclic softening or hardening is modelled. Kinematic hardening rule describe yield surface center displacement in stress space. Elastic domain is introduced as $f \leq 0$ in order to determine if plastic or viscoplastic behaviour occurs. f is the stress function and yield surface is defined for $f = 0$. The stress function f can be obtained in the case of von Mises yield surface as follows:

$$f = \sqrt{\frac{3}{2}\left(\boldsymbol{s} - \boldsymbol{x_D}\right) : \left(\boldsymbol{s} - \boldsymbol{x_D}\right)} - R - k, \tag{2.2}$$

where R is isotropic hardening function, k is the initial yield stress, $\boldsymbol{s}$ is deviatoric stress tensor and $\boldsymbol{x_D}$ is deviatoric backstress tensor. Backstress $\boldsymbol{x}$ describes kinematic hardening, i.e. location of the center of yield surface, and R is the isotropic increase of yield surface size. In the case of rate-independent, i.e. plastic, behaviour stress could not be located outside the elastic domain. However, for the viscoplastic behaviour, the stress state can go outside elastic domain and correspond to the value of overstress [22, 24], i.e. viscous stress $\sigma_v = f > 0$.

In the framework of unified viscoplastic models, the viscoplastic strain rate is determined on the basis of chosen viscosity function. The relation between the the viscoplastic strain rate and the viscous stress is usually non-linear for metal materials. Chaboche [22] used power-law function in the developed unified model:

$$\dot{p} = \left\langle \frac{f}{D} \right\rangle^n = \left\langle \frac{\sigma_v}{D} \right\rangle^n, \tag{2.3}$$

where $\dot{p}$ is the effective viscoplastic strain rate, D and n are temperature dependent material parameters. The flow rule in 2.3 correspond to the classical Norton law that is widely used to describe secondary creep behaviour. Regarding the power-law viscosity function, hyperbolic sine flow rule or exponential Norton law are other possible choices for viscosity function. Chaboche also generalized the viscoplastic behaviour with the use of so-called viscoplastic potential, Ω [22, 24, 48].

Kinematic hardening in plastic and viscoplastic constitutive equations can be modelled in various ways. Prager introduced linear kinematic hardening [72]. However, the linearity

between kinematic hardening and plastic strain is rarely observed for metals. Therefore, non-linear kinematic hardening was proposed by Frederick and Armstrong [5] by introducing so-called recall term, which is also known as dynamic recovery, in evolution equation of backstress as:

$$\dot{\boldsymbol{x}} = \frac{2}{3} C \dot{\boldsymbol{\varepsilon}}^{\boldsymbol{pl}} - \gamma_i \boldsymbol{x} \dot{p}, \tag{2.4}$$

where the first term correspond to the Prager linear kinematic rule and second term is the recall term that introduces non-linearity into the evolution law. C and γ are material dependent data, and $\dot{\boldsymbol{\varepsilon}}^{\boldsymbol{pl}}$ is plastic strain rate tensor. The non-linear kinematic hardening better corresponds with the experimental observations. Based on the Frederick and Armstrong work, Chaboche [21, 22, 48] showed that use of multiple backstress components improves the prediction of the hysteresis loop shape:

$$\boldsymbol{x} = \sum_{i=1}^{N} \boldsymbol{x}_i, \tag{2.5}$$

where usually three backstress components are sufficient. A general rule for kinematic hardening parameters is as follows, the first backstress term represents large (initial) plastic modulus of stress-strain curve, the second term corresponds to moderate segment of stress-strain curve. Finally, the third term describes constant hardening observed for large strains [48].

Chaboche also introduced the temperature term in the evolution law of backstress component [22, 24]:

$$\dot{\boldsymbol{x}}_{\boldsymbol{i}} = \frac{2}{3} C_i \dot{\boldsymbol{\varepsilon}}^{\boldsymbol{pl}} - \gamma_i \boldsymbol{x}_{\boldsymbol{i}} \dot{p} + \frac{1}{C_i} \frac{\partial C_i}{\partial T} \boldsymbol{x}_{\boldsymbol{i}} \dot{T}, \tag{2.6}$$

which is useful for modelling elastic-plastic mechanical response during the loading cycles with variable temperature, i.e. TMF loading conditions, and it also states that C and γ could be calibrated from the isothermal LCF data.

Cyclic hardening or softening can be taken into account by the means of isotropic hardening function that is usually considered in the following form:

$$\dot{R} = b \left(Q - R \right) \dot{p}, \tag{2.7}$$

where b and Q are temperature dependent material parameters. Eqs. 2.3, 2.5, 2.6 and 2.7 are generally known as Chaboche unified viscoplastic material model.

The non-linear kinematic hardening was subject of next study and possible modification were introduced. Ohno and Wang proposed modifications of dynamic recovery term in order to study ratcheting behaviour [69]. Ratcheting was studied by Jiang and Sehitoglu [43] and by other authors [38]. Chaboche introduced threshold term in order to predict mean stress relaxation and ratcheting [23]. Strain range dependent isotropic hardening was observed for selected materials during LCF tests. Therefore, Chaboche et al. introduced the plastic strain memory surface [20], this was later modified by Nouailhas et al. [67]. Furthermore, Chaboche introduced static recovery term in the kinematic hardening rule

[22] in order to better describe response for LCF tests with very long hold times. Static recovery for isotropic hardening was subject of research in [19, 68].

The unified Chaboche viscoplastic model and its modification have been used frequently in last few decades in order to obtain cyclic mechanical response under high temperature LCF and TMF loading conditions. Modifications of this type of model are usually not available by default in commercial finite element software, e.g. Abaqus and Ansys, however user is allowed to implement his own material model on the material point level by the means of user material subroutine [1]. Implicit backward Euler, which is also known as radial return algorithm, is usually used for integration of non-linear constitutive equations [32]. Kullig and Wipler [47] implemented isothermal version of unified Chaboche viscoplastic model with static recovery for kinematic hardening rule in the framework of finite element method, and the effect of consistent tangent stiffness [78] on the speed of convergence was underlined. Barrett et al. [7] showed advantages of hyperbolic sine flow rule in the framework of Chaboche type model for P91 steel under LCF and TMF loading conditions in order to obtain accurate cyclic mechanical response under various strain rates. Analytical derivation of consistent tangent stiffness for semi-implicit integration scheme of this model was studied in [6]. Ahmed et al. [2] used modified unified Chaboche based model with power-law flow rule for modelling response of Haynes 230 alloy under isothermal LCF and fatigue-creep loading conditions, where the creep fatigue interaction was studied during the strain hold time in compression.

Besides unified Chaboche viscoplastic model, Constantinescu et al. [29] used two-layer viscoplasticity material model for modelling mechanical behaviour of cast iron in order to predict TMF of exhaust manifold. The two-layer viscoplasticity material model was originally proposed by Kichenin [46], later the model was implemented in commercial finite element software Abaqus [1]. This model consists of two parallel networks, i.e. viscous and plastic network, and the total stress tensor, $\boldsymbol{\sigma}$, is obtained as:

$$\boldsymbol{\sigma} = \boldsymbol{\sigma}_p + \boldsymbol{\sigma}_v, \tag{2.8}$$

where $\boldsymbol{\sigma}_p$ and $\boldsymbol{\sigma}_v$ are the parts of total stress tensor in viscous and plastic part, respectively. The two-layer viscoplasticity material model may be classified as non-unified viscoplastic material model, because it treats the plastic part and the viscous part separately. However, this model can be used for cyclic loading conditions.

Other type of unified viscoplastic material models was developed by Miller [52]. Miller used one backstress, elastic domain reduced into one point together with viscosity function that consisted of combination of hyperbolic sine flow rule and power-law flow rule. The unified viscoplastic constitutive theory was also developed by Bodner et al. [11], where viscosity function was proposed as a combination of exponential function and power function. Later Bodner extended the materiel model with directional hardening [10]. Unified material models were also developed by other authors, e.g. [18, 73].

Nagode et al. [61] used Prandtl hysteresis operators for modelling stress-strain response for anisothermal elastoplasticity and later extended this approach with viscoplastic approximation based on the non-linear Maxwell model [60, 62]. The viscoplastic approximation

was then applied to elastic-plastic finite element analysis of turbocharger turbine housing and exhaust downpipes [62, 63]. Nagode approach will be further discussed in next section. The Prandtl hysteresis operators with viscoplastic approximation may be called classified as non-unified viscoplastic material model. This model is suitable for cyclic loading, because it assumes only strain control [60, 62]. Furthermore, effect of the used constitutive material model on TMF life prediction was studied by Mao et al. [50], where best prediction was obtained for unified viscoplastic material model.

2.3 LCF and TMF life predictions methods

There have been several approaches to TMF life prediction in last few decades. It is known that the oxidation, fatigue and creep are the main damage mechanisms involved in TMF and damage of each mechanism can be treated separately [64, 65, 74]. Then, total damage damage of the loading cycle, D_{total}, can be obtained by additive superposition of the individual damage mechanisms involved in TMF [64, 65, 74]:

$$D_{total} = D_{oxidation} + D_{fatigue} + D_{creep}, \tag{2.9}$$

where $D_{oxidation}$ is oxidation damage, $D_{fatigue}$ is fatigue damage and D_{creep} is creep damage. Fatigue damage in material is closely related to the microscopic and macroscopic crack growth. Creep damage is caused by the formation and growth of creep voids in the microstructure. Whereas oxidation damage is connected with chemical changes in the material surface due to environmental effects. The oxidized material is more brittle and prone to crack initiation. Contribution of individual mechanism on total damage depends on the length of the loading cycle and primarily on temperature. It is known that at low temperatures major contribution is due to fatigue mechanism, oxidation takes more effect at moderate temperatures and during OP-TMF, whereas creep is more significant during IP-TMF. At high temperature and IP-TMF all three mechanisms take apart. Neu and Sehitoglu proposed calculation of individual damage mechanism in Eq. 2.9, where fatigue damage can be obtained on the basis of classical strain-life curve as follows:

$$\frac{\Delta\varepsilon_{mech}}{2} = \frac{\sigma'_f}{E}\left(2N_f^{fatigue}\right)^b + \varepsilon'_f\left(2N_f^{fatigue}\right)^c, \tag{2.10}$$

where temperature dependent parameters are usually determined from low-temperature LCF tests, ε'_f, σ'_f, b and c are parameters of strain-life curve, E is elastic modulus and $N_f^{fatigue}$ is number of cycles to failure observed in these tests. A damage of the cycle is related to number of cycles to failure as $D_{fatigue} = 1/N_f^{fatigue}$. The oxidation damage, $D_{oxidation}$, reflects the oxidation induced crack nucleation and growth and its calculation is proposed by Neu and Sehitoglu [64, 65, 74] as follows:

$$D_{oxidation} = \left[\frac{h_{cr}\delta_0}{B\Phi^{ox}K_p^{eff}}\right]^{-\frac{1}{\beta}} \frac{2\left(\Delta\varepsilon_{mech}\right)^{(2/\beta+1)}}{\dot{\varepsilon}^{1-(\alpha/\beta)}}, \tag{2.11}$$

where the parameter h_{cr} describes the critical oxide layer thickness, α is the strain rate sensitivity constant, B is the coefficient, δ_0 responds to the ductility of the oxide layers and β controls the oxide layer growth. The values of all above constants are determined by experiments. Φ^{ox} is a phasing factor for environmental damage and is defined as:

$$\Phi^{ox} = \frac{1}{t_c} \int_0^{t_c} \phi^{ox} dt, \tag{2.12}$$

$$\phi^{ox} = \exp\left[-\frac{1}{2} \left(\frac{\dot{\varepsilon}_{th}/\dot{\varepsilon}_m + 1}{\xi^{ox}} \right)^2 \right], \tag{2.13}$$

where $\dot{\varepsilon}_{th}/\dot{\varepsilon}_m$ is the ratio of thermal strain rate to mechanical strain rate. ξ^{ox} is a constant defined as a measure of the relative amount of oxidation damage for different ratios of thermal strain rate to mechanical strain rate and is obtained from the experimental data. Moreover, K_p^{eff} is a oxidation constant and can be calculated as:

$$K_p^{eff} = \frac{1}{t_c} \int_0^{t_c} D_0 \exp\left(-\frac{Q}{RT(t)} \right) dt, \tag{2.14}$$

where D_0 is the diffusion constant for oxidation, Q is the activation energy for oxidation, t_c is the cycle period, R is the universal gas constant and $T(t)$ is the temperature as a function of time. Finally, creep damage calculation is proposed in Neu and Sehitoglu damage model [64, 65, 74] as follows:

$$D_{creep} = \Phi^{creep} \int_0^{t_c} A \exp\left(-\frac{\Delta H}{RT(t)} \right) \cdot \left(\frac{\alpha_1 \bar{\sigma} + \alpha_2 \sigma_H}{K} \right)^m dt, \tag{2.15}$$

where $\bar{\sigma}$ is the effective stress, σ_H is the hydrostatic stress, K is the drag stress, α_1 and α_2 are scaling factors that represent the relative amount of damage occurring in tension and compression, ΔH is the activation energy for the rate-controlled creep mechanism, and A and m are material constants. Φ^{creep} is a phasing factor for creep and is defined in a same way as for oxidation as:

$$\Phi^{creep} = \frac{1}{t_c} \int_0^{t_c} \phi^{creep} dt, \tag{2.16}$$

$$\phi^{creep} = \exp\left[-\frac{1}{2} \left(\frac{\dot{\varepsilon}_{th}/\dot{\varepsilon}_m + 1}{\xi^{creep}} \right)^2 \right], \tag{2.17}$$

where ξ^{creep} defines the sensitivity of the phasing to the creep damage. Sehitoglu et al. [44, 74, 75] applied model to predict TMF life of MAR-M247 nickel super-alloy and 1070 steel alloy with good correlation. Minichmayr [53] used the Neu-Sehitoglu damage model in order to predict TMF lifetime of aluminium alloy, where the model was calibrated up to 300°C from LCF tests obtained at different temperatures and at various strain rates, the LCF tests were also performed in argon atmosphere, finally multiple IP-TMF and OP-TMF tests were performed in order to calibrate model.

However, the separation of the three damage mechanisms requires material tests that are performed in ambient air and also in vacuum in order to separate oxidation damage. Also, considerable amount of material parameters must be calibrated in this method. This requires environmental chamber as a part of the test stand and relatively large amount of test data in order to calibrate the damage model. Therefore, it can be deduced that the damage model proposed by Neu and Sehitoglu is not well suited for engineering predictions and applications. This lead into that the oxidation effect is taken into account indirectly in most life prediction methods, because material tests are usually performed only under ambient conditions and not in vacuum. It's widely accepted that linear damage accumulation, which is based on Palmgren-Miner work, is used for LCF and TMF life prediction.

The classical strain-life approach is based on the work of Manson-Coffin, Ostergen and Smith-Watson-Topper [28, 39, 49, 70, 81]. Well known Manson-Coffin fatigue criterion is written as:

$$\Delta\varepsilon_{pl} N_f^{\beta} = c, \tag{2.18}$$

where c and β are material dependent parameters and calibrated from the available test data. $\Delta\varepsilon_{pl}$ is the plastic strain range of the loading cycle and N_f is number of cycles to failure. Ostergen proposed following fatigue criterion:

$$\sigma_{max}\Delta\varepsilon_{pl} N_f^{\beta} = c, \tag{2.19}$$

where σ_{max} is peak tensile stress in the cycle. Smith-Watson-Topper taken mean stress into account in following form:

$$\sqrt{E\sigma_{max}\Delta\varepsilon} N_f^{\beta} = c, \tag{2.20}$$

where E is the elastic modulus and $\Delta\varepsilon$ is the mechanical strain range of the cycle. Both Ostergen and Smith-Watson-Topper taken effect of mean stress into account in their proposed criteria. Another classical criterion is strain range partitioning proposed by Halford and Manson [39].

The classical strain-life approach used for the life prediction of components subjected to low-temperature LCF is generally not a reliable method for TMF life predictions, since there are changes in temperature during the loading cycle. The material response and also the strain-life curves change with temperature during TMF loading conditions, resulting in positive mean stress for an out-of-phase cycle or resulting in negative mean stress for an in-phase cycle. Furthermore, observed TMF lifetime in comparison with observed LCF lifetime, which is obtained for equivalent loading, is usually different and often reduced. TMF life prediction is generally more challenging than LCF life predictions. It's common practice that TMF life prediction methods are also applicable for isothermal LCF loading. The changes in temperature during the TMF loading cycle and the observed mean stress can be taken into account in various ways. Multiple phenomenological TMF damage criteria can be found in literature, e.g. energy based damage models, damage models based on fracture mechanics or models based on the classical strain-life approach.

In the framework of isothermal low-cycle fatigue, Ostergen [70] studied isothermal LCF with different frequency of a cycle and showed that damage is dependent on a test frequency. Chaboche and Gallerneau [25] studied continuum damage mechanics for aero-engine single-crystal super-alloy under isothermal and thermo-mechanical loading conditions. Chaboche and Gallerneau studied two different damage models, a creep–fatigue damage model and creep–fatigue–oxidation model. The interaction between fatigue and creep damage was suggested in the creep–fatigue–oxidation damage model, this was achieved by separating micro-initiation and micro-propagation stages for fatigue.

Rainflow cycle counting and linear damage cumulation is widely used in strain-life approach that is used for isothermal LCF in order to treat damage of each loading cycle separately. Taira [83] proposed equivalent temperature of the loading cycle in order to take variable temperature during the loading cycle into account. The classical strain-life approach was considerably improved by Nagode et al.[61] for anisothermal loading cycles. Nagode introduced so-called Damage Operator Approach (DOA), where Prandtl hysteresis operators were used in order to model cyclic fatigue damage cumulation during the loading cycle and extended the theory for a cycle with variable temperature. The DOA is based on the fundamentals of mathematical theory of hysteresis operators and continuous rainflow method [12, 13]. The approach proposed by Nagode enables continuous fatigue and creep damage calculation for loading cycles with variable temperatures. Creep damage and fatigue damage are treated separately. Creep damage, D_{creep}, is computed by well known time-fraction rule that is also known as Robinson's rule:

$$D_{creep}(t) = \int_0^t \frac{dt}{t_R(\sigma(t), T(t))} \tag{2.21}$$

where t_R is the time to rupture for current stress $\sigma(t)$ and temperature $T(t)$, which is determined from the creep master curves. The oxidation effect is taken into account indirectly in creep and fatigue damages under the assumption that material tests were performed under ambient conditions. Nagode et al. also used hysteresis operators for modelling temperature dependent elastic-plastic response of material [59, 61]. Consequently, Nagode et al. proposed viscoplastic approximation in order to predict TMF life from the elastic-plastic constitutive model [60, 62]. Nagode et al. then applied his approach on TMF life predictions of engineering components [62, 63, 76]. Mean-stress correction was represented by Smith-Watson-Topper damage parameter [81] that needs to be calculated on-line in this approach [58]. Nagode et al. compared von Mises equivalent stress with equivalent stress computed by critical plane approach for DOA in [62]. The Nagode approach is based on the isothermal LCF data and static creep rupture tests. Key steps of so-called damage operator approach are discussed in detail below.

The equivalent stress $\sigma_i(t_i)$ and the temperature history $T_i(t_i)$ are obtained from the structural FEA that was performed for investigated component. First step is the uniaxial instantaneous strain $\varepsilon_i(t_i)$ that can be expressed in the form of a Prandtl type operator

[62] as:

$$\varepsilon_i(t_i) = \sum_{j=1}^{n_r} \alpha_j(T_i)\sigma_{\alpha j}(t_i) \tag{2.22}$$

for $0 \leqslant t_1 \leqslant t_2 \leqslant ... \leqslant t_i \leqslant ...$, where $T_i = T(t_i)$ is the current temperature and $\sigma_{\alpha j}(t_i)$ is the play operator with a general initial value defined as follows:

$$\sigma_{\alpha j}(t_i) = max\{\sigma_i(t_i) - r_j, min\{\sigma_i(t_i) + r_j, \frac{\alpha_j(T_{i-1})}{\alpha_j(T_i)}\sigma_{\alpha j}(t_{i-1})\}\} \tag{2.23}$$

$\sigma_{\alpha j}(t_i)$ is the backstress, and follows kinematic hardening rules. r_j are the yield stresses of the segment sliders, and $\alpha_j(T_k)$ are temperature dependent Prandtl densities, which can be derived from the available cyclically stable cyclic stress-strain curves obtained at high strain rates, Fig. 2.2. High strain rate is recommended in order to separate creep damage. Next step depends on the constitutive model that was used in FEA. The elastic-plastic

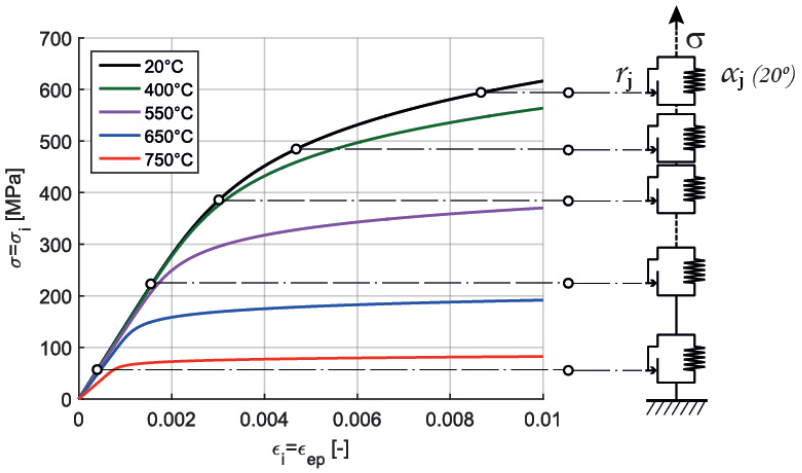

Figure 2.2: Temperature dependent cyclically stable cyclic stress-strain curves obtained at high strain rates, and the associated stress-controlled spring-slider model according to Nagode et al.

strain, $\varepsilon_{ep}(t_i)$, contributes to the fatigue damage, and is separated from the total mechanical strain using Eq. 2.22 for the viscoplastic material model, because the stress obtained from FEA is real stress. Nagode et al. proposed viscoplastic approximation for elastic-plastic constitutive model in order to take into account time dependent effects represented by stress relaxation. The viscoplastic approximation is based on strain controlled model, scheme is presented in Fig. 2.3.

Finally, the real stress $\sigma_i(t_i)$ and the elastic-plastic strain $\varepsilon_{ep}(t_i)$ are transferred into the selected damage parameter $P_i(t_i)$. Fatigue damage can be expressed as the total variation:

$$D_f(t_i) = D_f(t_{i-1}) + |\mathcal{D}(t_i) - \mathcal{D}(t_{i-1})| \tag{2.24}$$

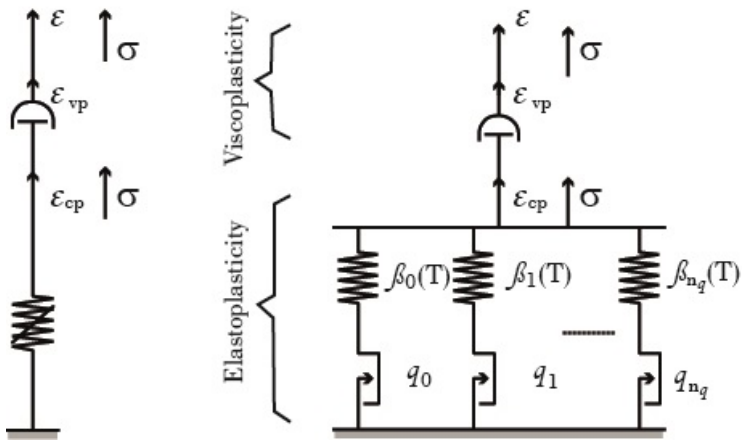

Figure 2.3: Non-linear strain controlled Maxwell model according to Nagode et al.

The damage operator $\mathcal{D}(t_i)$ introduces the cyclic damage evolution and follows the Masing and memory rules. The damage operator is expressed as:

$$\mathcal{D}(t_i) = \sum_{j=1}^{n_p} \mathcal{D}_j(t_i) = \sum_{j=1}^{n_p} \gamma_j(T_i) P_{\gamma_j}(t_i) \tag{2.25}$$

for $0 \leqslant t_1 \leqslant t_2 \leqslant ... \leqslant t_i \leqslant ...$, where $P_{\gamma j}$ is the play operator with a general initial value given as:

$$P_{\gamma_j}(t_i) = max\{P(t_i) - p_j, min\{P(t_i) + p_j, \frac{\gamma_j(T_{i-1})}{\gamma_j(T_i)} P_{\gamma_j}(t_{i-1})\}\} \tag{2.26}$$

$P_{\gamma_j}(t_i)$ represents the backstress and follows kinematic hardening, p_j are the yield stresses of the segment sliders, $\gamma_j(T_k)$ are the temperature dependent Prandtl densities that are obtained from the temperature dependent strain-life or damage parameter - life curves, which need to have been transformed, Fig. 2.4. The fatigue damage is modelled similarly to the cyclic plasticity using hysteresis operators. The total damage is obtained as follows:

$$D(t) = D_c(t) + D_f(t). \tag{2.27}$$

In the framework of energy based TMF and LCF prediction models, a key point is a hysteresis energy, w, i.e. dissipated energy over the loading cycle, which can be obtained by the numerical integration as follows:

$$w = \int_{cycle} \boldsymbol{\sigma} : \dot{\boldsymbol{\varepsilon}} \, dt, \tag{2.28}$$

where $\boldsymbol{\sigma}$ is the stress tensor and $\dot{\boldsymbol{\varepsilon}}$ is the mechanical strain rate tensor. Hysteresis energy is usually integrated from the stabilized hysteresis loop in order to predict fatigue. Generally,

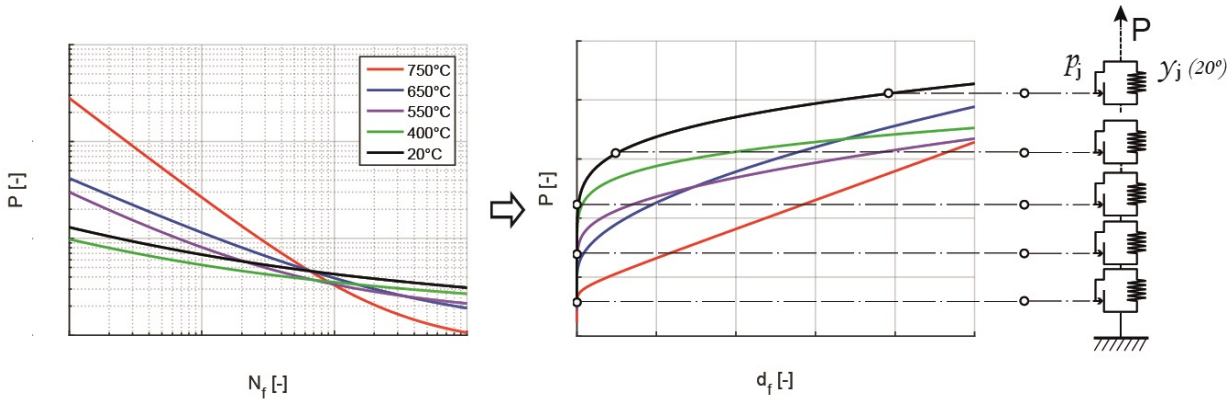

Figure 2.4: Temperature dependent PN and PD curves with the associated spring-slider model for test temperatures according to Nagode et al.

energy based damage models are closely related to fracture mechanics. Feltner et al. introduced energy based models in [33] and asserted interesting idea: *"... to start with a specimen in one piece and then after the application of a finite number of load cycles find it to be in two pieces, requires a conversion of energy. The energy necessary to cause fracture is collected in small amounts during the course of the cyclic loading and is observable in terms of strain hysteresis"*. Skelton [79, 80] showed that the accumulated dissipated energy until stabilization in the loading cycle can be considered constant for a given material and can be used as a crack initiation criterion in LCF. Furthermore, Skelton et al. [80] expressed crack growth rate as a function of the accumulated energy to saturation. Charkaluk and Constantinescu discussed Skelton findings for cast iron in [27]. Constantinescu et al. [29] used classical hysteresis energy based criterion defined as:

$$wN_f^{\beta} = c. \tag{2.29}$$

Constantinescu et al. also predicted possible modification of this criterion in order to take mean stress into account. Moreover, computational approach to TMF was presented in [29] in order to calculate lifetime by Eq. 2.29 of different prototypes of exhaust manifold. Classical hysteresis energy based criterion was modified in [41] as follows:

$$\left(dw + b\frac{(\Delta\sigma_{eff})^2}{2E} \right) N_f^{\beta} = c, \tag{2.30}$$

where σ_{eff} is effective stress amplitude defined as:

$$\sigma_{eff} = \Delta\sigma \cdot e \cdot (3 - R)^f, \quad R = \frac{\sigma_{min}}{\sigma_{max}}, \tag{2.31}$$

where b, d, e and f are material dependent parameters, and elastic modulus, E, is usually determined as a mean value from the values of elastic modulus at minimum and maximum temperature of the loading cycle. Amiable et al. [3, 4] studied different constitutive models

and different fatigue criteria in order to predict lifetime of specimens exhibited to thermal shock. Amiable et al. proposed modified hysteresis energy criterion:

$$(w + \alpha P_{max})\, N_f^{\beta} = c, \tag{2.32}$$

where α is the material dependent parameter that is calibrated from the isothermal LCF data. P_{max} is the maximal hydrostatic pressure achieved over the loading cycle:

$$P_{max} = \max_t P(t). \tag{2.33}$$

Tabibian et al.[82] predicted LCF and OP-TMF lifetime of lost foam casting A319 aluminum alloy for temperatures between 100-250°C, where selected criteria from Eqs. 2.28, 2.30 and 2.32, were discussed and best correlation was achieved for criterion with maximal hydrostatic pressure, Eq. 2.32.

2.4 Discussion and conclusion

High temperature LCF and particularly TMF tests require expensive test stands with heating of the specimen and with independent temperature and strain control during the loading cycles. High temperature extensometers with ceramic rods are usually used in order to control strain, whereas thermocouples are used in the control of specimen temperature. High temperature LCF and TMF test data are not available for most materials in a literature, therefore the tests for specimens that are manufactured from the investigated material must be performed in order to obtain fatigue data, represented for example by strain-life curves, and in order to calibrate constitutive material model that is used in finite element analysis, which is substantial for lifetime predictions of complex components under LCF and TMF loading conditions.

A unified viscoplastic constitutive material model according to Chaboche that incorporates viscous behaviour together with non-linear kinematic hardening and isotropic hardening has been used frequently in order to simulate mechanical behaviour of metals subjected to LCF and TMF loading conditions. The material model was frequently used in its original version and as well as in its modified form. The unified viscoplastic material models are usually not implemented or are implemented in basic version in commercial finite element software packages. However, the user is allowed to implement his own material model by the means of user defined subroutine. Several implementations of such models in the framework of finite element method were published, however derivation of consistent tangent stiffness is mostly not published, although it is harder part of the implementation process of constitutive material model. Consistent tangent stiffness is essential in order to solve large engineering problems. In the framework of unified material model calibration, Chaboche [24] introduced basic steps in order the calibrate model. Usually material parameters are calibrated for each temperature separately and then interpolated, although this may lead to slow convergence or convergence issues for anisothermal loading, especially in the case of non-linear hardening parameters. However, Hosseini et al. [42] proposed interesting idea to systematically calibrate the kinematic hardening material parameters for a range of temperatures.

Sehitoglu and Neu proposed TMF and LCF damage model, where oxidation damage, fatigue damage and creep damage are treated separately. The model is probably most accurate for lifetime predictions under LCF and TMF. However, that is related to large amount of model parameters that require large amount of experimental data. In addition, material test should be attained in vacuum or inert gas atmosphere in order to calibrate this damage model, this requires expensive test stands and equipment. Sehitoglu-Neu damage model hardly fits industrial constraints, which tends to push the design phase of components to lower times. Therefore, several other approaches were proposed. It can be observed that carrying material tests only under ambient condition and taking oxidation into account indirectly is in common for these methods. Nagode et al. proposed TMF life prediction that is based on isothermal test data, the method is based on mathematical theory of hysteresis operators. This approach can be used together with the viscoplastic approximation, which was also proposed by Nagode et al., for life predictions from elastic-

plastic material model, which should be used in previous finite element analysis of the investigated component. However, the viscoplastic approximation together with the critical plane approach to multiaxial fatigue may lead to very long computational times as the damage and the viscoplastic approximation must be calculated in every assumed plane[1]. Furthermore, the Nagode approach is based on the strain partitioning into elastic-plastic and creep, this is questionable for the unified viscoplastic material models, as creep and plasticity occurs simultaneously and interact with each other during high temperature LCF and TMF loading conditions. The approach proposed by Nagode may also be very hard to interpret due to its mathematical formulation.

Furthermore, several energy based LCF and TMF life prediction methods were proposed. It is naturally appropriate to use energy-based criterion together with a unified viscoplastic material model. The proposed energy based criteria not always correctly reflected mean stress effect on the lifetime. Moreover, calculation of dissipated energy under multiaxial loading conditions is much more time efficient in comparison with critical plane approach. Energy based LCF/TMF lifetime methods are therefore possible subject of research.

[1]This method was analysed and presented together with new results in [A.4].

Chapter 3

Methods

3.1 The radial return algorithm

Implicit backward Euler is usually chosen for numerical integration of the constitutive equations of von Mises plasticity and viscoplasticity due to its absolute stability, and is chosen for integration of constitutive equation of the selected viscoplastic material model in this work, Chapter 6. The method is also known as radial return algorithm. The overview of the method is given below, although reader more interested in computational plasticity is redirected to e.g. [32, 77].

A basic principle of the method is to compute a trial elastic stress increment, this yields new updated trial stress tensor (elastic predictor), $\boldsymbol{\sigma}^{tr}_{t+\Delta t}$, outside yield surface. Then the stress tensor is updated with a plastic correction (plastic corrector) in order to bring it back onto the yield surface at time $t+\Delta t$, in the case of viscoplasticity it is surface defined by overstress [22]. The plastic correction term is always directed towards the centre of the yield surface. Therefore, the technique become to be known as the radial return method. The quantities at the start of the increment shall be noted with subscript $_t$ and quantities at the end of increment shall be noted without special subscript.

The Hooke's law can be written in following form:

$$\boldsymbol{\sigma} = 2G\boldsymbol{\varepsilon}^e + \lambda Tr(\boldsymbol{\varepsilon}^e)\boldsymbol{I}, \tag{3.1}$$

where G is the shear modulus and λ is the Lamé constant. The elastic strain tensor at the end of increment can be written as:

$$\boldsymbol{\varepsilon}^e = \boldsymbol{\varepsilon}^e_t + \Delta\boldsymbol{\varepsilon}^e = \boldsymbol{\varepsilon}^e_t + \Delta\boldsymbol{\varepsilon} - \Delta\boldsymbol{\varepsilon}^{pl}, \tag{3.2}$$

where $\Delta\boldsymbol{\varepsilon}^{pl}$ is the plastic strain tensor increment. Substituting Eq. 3.2 into Eq. 3.1, assuming $Tr(\Delta\boldsymbol{\varepsilon}^{pl}) = 0$, gives:

$$\boldsymbol{\sigma} = \underbrace{2G\left(\boldsymbol{\varepsilon}^e_t + \Delta\boldsymbol{\varepsilon}\right) + \lambda Tr\left(\boldsymbol{\varepsilon}^e_t + \Delta\boldsymbol{\varepsilon}\right)\boldsymbol{I}}_{Elastic\ predictor} - \underbrace{2G\Delta\boldsymbol{\varepsilon}^{pl}}_{Plastic\ corrector}. \tag{3.3}$$

The stress tensor can be rewritten from Eq. 3.3 as a function of trial stress, i.e. elastic predictor, and effective plastic strain increment, Δp, as follows:

$$\boldsymbol{\sigma} = \boldsymbol{\sigma}^{tr} - 2G\Delta\boldsymbol{\varepsilon}^{pl} = \boldsymbol{\sigma}^{tr} - 2G\Delta p\boldsymbol{n}, \tag{3.4}$$

where $\boldsymbol{n}$ is the stress normal [32]. Furthermore, von Mises equivalent stress, σ_e, can be rewritten in the terms of trial von Mises equivalent stress, σ_e^{tr}, as follows:

$$\sigma_e^{tr} = \sigma_e + 3G\Delta p. \tag{3.5}$$

Assuming multiaxial yield condition:

$$f = \sigma_e - R - k = \sigma_e^{tr} - 3G\Delta p - R - k = 0. \tag{3.6}$$

This generally leads to a non-linear equation in Δp that is usually solved by Newton iterative method:

$$f + \frac{\partial f}{\partial \Delta p} d\Delta p + \cdots = 0. \tag{3.7}$$

The form of equation depends on the used constitutive model. Finally, after obtaining effective plastic strain increment by Newton method, the elastic strain tensor increment is obtained on the basis of plastic strain tensor increment as:

$$\Delta\boldsymbol{\varepsilon}^e = \Delta\boldsymbol{\varepsilon} - \Delta\boldsymbol{\varepsilon}^{pl} \tag{3.8}$$

so that stress tensor increment is obtained on the basis of Hooke's law as:

$$\boldsymbol{\sigma} = 2G\Delta\boldsymbol{\varepsilon}^e + \lambda\boldsymbol{I}\Delta\boldsymbol{\varepsilon}^e : \boldsymbol{I}. \tag{3.9}$$

3.2 Minimum of constrained non-linear multi-variable function

Function *fmincon* (*Find a minimum of constrained non-linear multi-variable function*) from Matlab optimization toolbox [51] is used in order to optimize values of kinematic hardening parameters with temperature in Chapter 6. The main objective is to finds the minimum of a problem specified as:

$$\min_x f(x), \text{subject to } h(x) = 0 \text{ and } g(x) \leq 0, \tag{3.10}$$

where g and h are vector functions representing all inequality and equality constraints, respectively. and $f(x)$ is a scalar function, which is formulated as sum of squares of differences between test and model data. The interior-point algorithm is adopted in order

to solve the problem. Main principle is to solve a sequence of approximate minimization problems. For each μ, the approximate problem can be written as:

$$\min_x f_\mu(x,s) = \min_x f_\mu(x) - \mu \sum_i \ln(s_i), \text{ subject to } h(x) = 0 \text{ and } g(x) + s = 0. \quad (3.11)$$

Number of slack variables s_i equals to number of inequality constraints g. The s_i are restricted to be positive to keep $ln(s_i)$ bounded. As μ decreases to zero, the minimum of f_μ should approach the minimum of f. The logarithmic term is called a barrier function. The approximate problem, Eq. 3.11, is a sequence of equality constrained problems, which are easier to solve than the original inequality-constrained problem, Eq. 3.10. To solve the approximate problem, the algorithm uses one of two main types of steps at each iteration:

- A direct step,
- A conjugate gradient step.

By default, the algorithm first attempts to take a direct step. If it cannot, it attempts a conjugate gradient step. Only when the approximate problem is not locally convex near the current iterate, the algorithm doesn't take a direct step. The algorithm decreases a target function at each iteration. If an attempted step does not decrease the target function, the algorithm rejects the attempted step, and attempts a new step. More about the method can be found in [15, 16, 51, 84].

3.3 Non-linear least square method

Non-linear least square method is used for calibration of fatigue criteria and for calibration of the constitutive material model, therefore brief overview is given. Non-linear least-squares solver available in MATLAB [51] is used in order to solve non-linear least-squares curve fitting problems of the following form:

$$\min_x \|f(x)\|_2^2 = \min_x \left(f_1(x)^2 + f_2(x)^2 + \cdots + f_n(x)^2\right), \quad (3.12)$$

on the components of x, where the function, $f(x)$, is usually defined as difference between data points and model function. Lower and upper bounds are used here, therefore the trust-region-reflective least squares algorithm [51, 54] is applied. The basic principle of the algorithm is to approximate f with a simpler function q, which appropriately reflects the behaviour of function f in a neighbourhood N around the point x, this neighbourhood is the trust region. A trial step s is computed by minimizing over N. This is the trust-region sub-problem:

$$\min_s \{q(s), s \in N\}. \quad (3.13)$$

The current point is updated to be $x + s$ if $f(x + s) < f(x)$, otherwise, the current point remains unchanged and the region of trust, is shrunk and the trial step computation is repeated.

$$\min\{\frac{1}{2}s^T Hs + s^T g \text{ such that } \|Ds\| \leqslant \Delta\}, \tag{3.14}$$

where g is the gradient of f at the current point x, H is the Hessian matrix, D is a diagonal scaling matrix, Δ is a positive scalar, and $\|.\|$ is the 2-norm. Algorithms for solving Eq. 3.14 are described in [54].

Finally, the trust-region algorithm can be summarized into four steps that are repeated until convergence is obtained:

1. Formulate of the two-dimensional trust-region sub-problem,
2. Solve Eq. 3.14 in order to determine s,
3. If $f(x + s) < f(x)$, then $x = x + s$,
4. Adjust Δ.

3.4 Prediction bounds

Prediction bounds [40] are used in Chapter 7.2. The bounds are used to measure the confidence that the new observation lies in the interval given by a single predictor value:

$$y \pm t_{1-\alpha/2} s \sqrt{1 + x \left(X^T X\right)^{-1} x^T}, \tag{3.15}$$

where s is the standard error, $t_{1-\alpha/2}$ denotes the inverse of Student cumulative distribution in dependence on confidence level. X is the design vector of explanatory variables. y is the fitted or predicted value of predictor x.

The standard error is given as:

$$s = \frac{\sum_{i=1}^{n} \left(y_i - y_{i\ obs}\right)}{\sqrt{n - p}}, \tag{3.16}$$

where $y_{i\ obs}$ are the values of observations, p is the number of fitted coefficients, and n is the number of degrees of freedom.

Chapter 4

Aims of the thesis

Aims of the thesis were chosen on the basis of conclusions defined in the previous chapter 2. The aims can be summarized into the following points:

1. Proposal of a novel energy based fatigue criterion that can be used for lifetime predictions under LCF and TMF loading conditions and that is calibrated across the obtained LCF and TMF test data. Main requirements for the criterion are that it is robust and usable for lifetime predictions of complex engineering structures.

2. Development of the control algorithms for the newly in-house designed test stand, which was designed with a view of cost-effectiveness, and that can be used for uniaxial strain controlled LCF and TMF tests.

3. Experimental research of SiMo 4.06 cast iron mechanical behaviour under TMF and LCF loading conditions. Acquirement of new and original experimental data that are usable for calibration of a viscoplastic material model and a damage model that can be both used in LCF/TMF life prediction method for engineering components.

4. Implementation and numerical integration of the selected unified viscoplastic material model by the means of user material subroutine for commercial finite element software. Formulation and analytical derivation of consistent tangent stiffness that is a key point for solving large engineering problems. Validation of the consistent tangent stiffness.

5. Development of the calibration tool for the selected unified viscoplastic material model. Proposal of a novel method for calibration of temperature dependent material parameters. Calibration of the constitutive material model on the basis of original LCF and TMF test data. Validation of the calibrated material model on the basis of obtained experimental data.

Chapter 5

Experiments

This chapter is divided into five sections. First, new in-house designed test stand is introduced in Section 5.1. The test stand can be used for uniaxial LCF and TMf tests. Next, properties of investigated material are briefly commented in Section 5.2. Test conditions are described in Section 5.3. The experimental results of LCF and TMF of SiMo 4.06 are presented in Section 5.4. Finally, results from this chapter are discussed in Section 5.5.

5.1 A new test stand

The material tests were carried out on an in-house designed test stand [A.1, A.9, A.11, A.12, A.13, A.16], Fig. 5.1. The test stand was designed as a jig to an Instron PL 160 K servo-hydraulic actuator. The structure of the device in terms of its connecting dimensions and geometry can be modified for other actuators of similar parameters. The advantage of the solution described here is that the actuator is not tied to the heating-clamping device, but can be dismounted and used for other material tests or structural tests, if required. The proposed test stand consists of a mechanical part and an electrical part. The specimen is heated by direct electrical resistance heating. The setup consists of two steel parts. The inner part is under voltage, and is in contact with the specimen. The outer part is attached both to the actuator body and to the piston. The parts of the setup are secured with bolts and are separated using ceramic insulation. This design enables the force to be transferred between actuator and specimen, while the actuator is protected from any external voltage.

The maximum achievable load for the test stand is 160 kN, and the maximum allowable temperature of the specimen is up to 1200°C. The temperature is measured and controlled by the K-type spot-welded thermocouple in the center of the specimen; pyrometry was avoided [9, 37]. The strain is controlled by the axial high temperature extensometer (usable up to 1200°C) with a gauge length of 8.9 mm. The force is measured by the built-in Instron load cell. The PC based system is connected with a NI-DAQ measurement card that collects the data from the sensors. The card is also used for temperature control and for strain control. Closed-loop control is achieved by a combination of LabView and Instron control software, Fig. 5.2 [A.1, A.9, A.11, A.12, A.13].

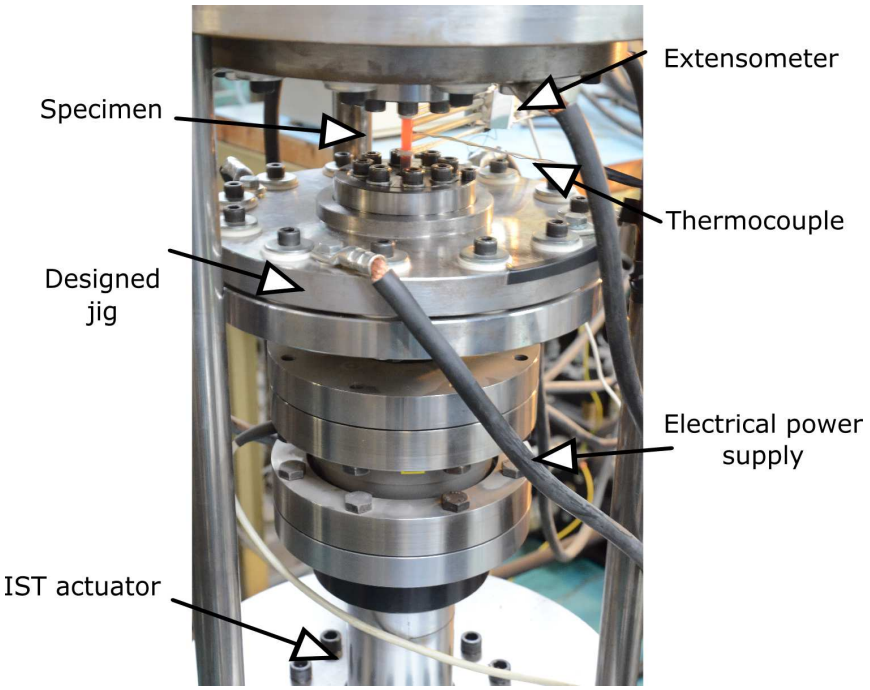

Figure 5.1: Test stand for LCF/TMF testing.

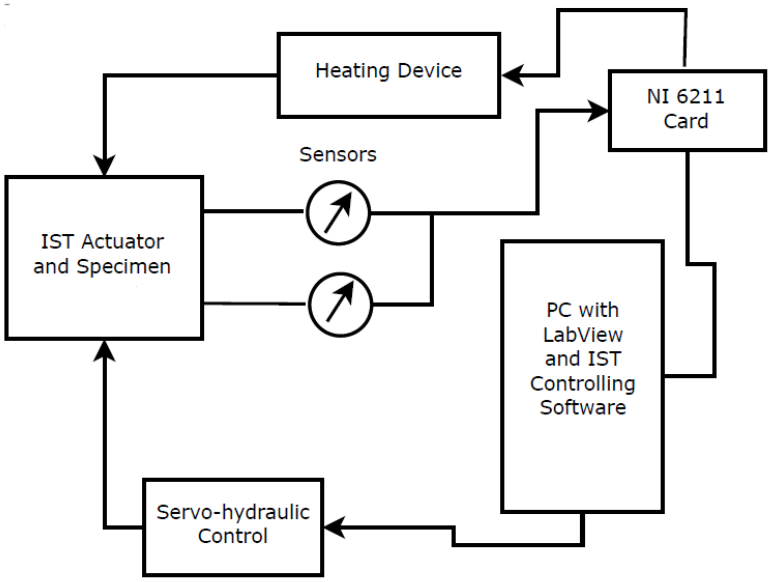

Figure 5.2: Closed-loop control of the LCF/TMF test stand.

The temperature distribution of the heated specimen was analyzed experimentally by infrared thermography, Fig. 5.3, and also with the use of thermocouples, to verify the temperature uniformity in the gauge length of the specimen. The experimental results for steady-state temperature distribution with 623°C in the center of specimen are presented in Fig. 5.4 [A.1]. The temperature deviation from the maximum temperature is less than 2% in the gauge length. The radial temperature gradients are assumed to be negligible due to the small diameter of the specimen, and due to the high thermal conductance of the investigated material. This should ensure that the measured part of the specimen is homogeneous, i.e. represents one material point, in accordance with [36, 37].

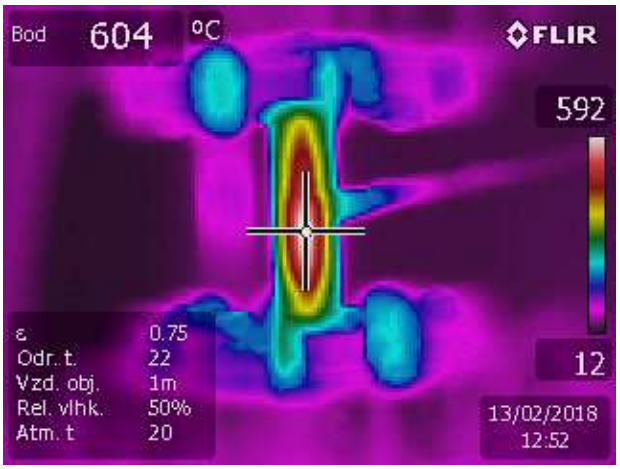

Figure 5.3: Infrared thermographic analysis of the temperature distribution.

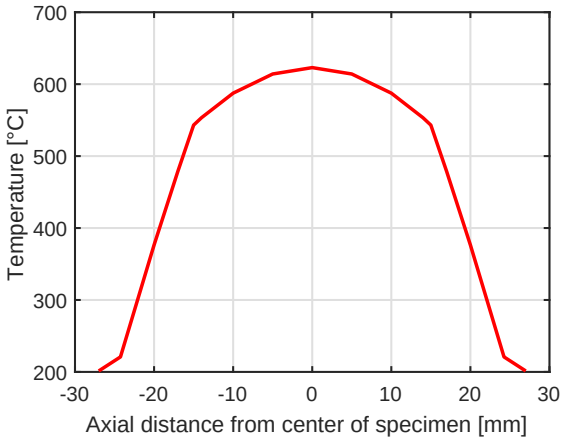

Figure 5.4: Measured temperature distribution on the axis of the specimen.

Table 5.1: Chemical composition of Si-Mo cast iron.

Si [%]	C [%]	Mo [%]	Mn [%]	Cr [%]	Cu [%]	Mg [%]	P [%]	Ni [%]	Al [%]
4.10	3.21	0.555	0.394	0.085	0.066	0.048	0.038	0.024	0.018

5.2 Investigated material

The material under investigation is silicon molybdenum cast iron with a spherical graphite, annealed. Good cast-ability and relatively low price makes silicon-molybdenum cast iron a good and popular choice in the automotive industry, where it is used in the production of turbine housings and exhaust manifolds. The nominal chemical composition of the material is given in Tab. 5.1. The addition of silicon increases heat-resistance by forming a protective layer on the surface, which provides protection to high-temperature oxidation. Molybdenum is added in order to improve creep and stress rupture properties of the cast iron. The spherical graphite was approximately 15 micrometers in size for the investigated material, Fig. 5.5. Tests were performed for cylindrical specimens with a gauge diameter of 6.5 mm, parallel length 24 mm and gauge length 8.9 mm, Fig. 5.6. It should be noted that each specimen was cast separately and then machined. This may possibly lead differences in a mechanical response of single specimens [A.1].

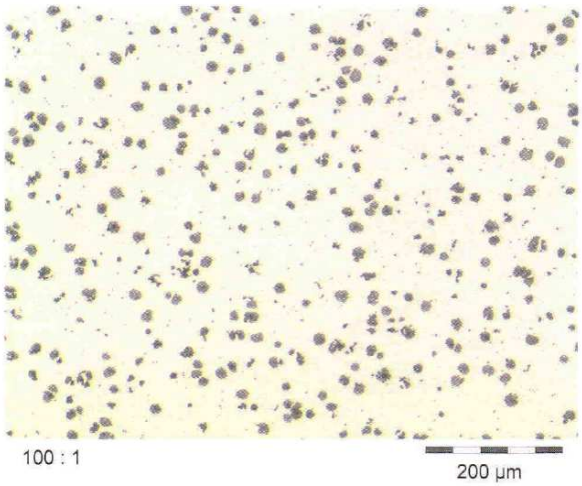

Figure 5.5: Microstructure of the SiMo cast iron at room temperature.

5.3 Test conditions

Strain-controlled LCF and TMF tests were performed under ambient conditions for cylindrical specimens. The LCF tests were performed with and without a dwell time. LCF tests with no dwell time were carried out at 20°C, 400°C, 550°C, 650°C and 750°C, fully

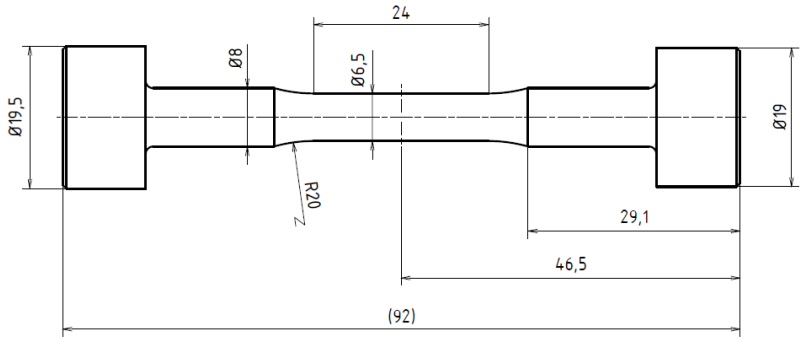

Figure 5.6: Geometry of the cylindrical specimen used for the LCF and TMF tests.

reversed (R_ε =-1), for variable mechanical strain ranges $\Delta\varepsilon_m$ from 0.005 to 0.025. The LCF tests with 300 s hold time in tension were carried out at various temperatures between 300°C and 750°C for mechanical strain range $\Delta\varepsilon_m$= 0.012. The LCF tests were performed with a constant mechanical strain rate, $\dot{\varepsilon}_m = 0.003\ s^{-1}$.

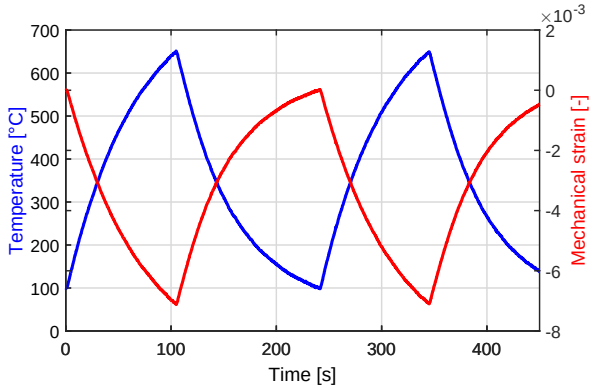

Figure 5.7: The temperature-strain-time path for the OP-TMF test.

The TMF tests were performed with a minimum test temperature of 100°C and with a maximum test temperature of 650°C. The TMF tests were performed with no dwell periods as out-of-phase tests (OP-TMF). The thermal strain was totally suppressed for the tests, so the total strain ε_t was kept constant. The mechanical strain ε_m, according to the condition $\varepsilon_t = \varepsilon_{th} + \varepsilon_m$, was then shifted against the thermal strain ε_{th} by 180°, with the amplitude equal to the thermal strain amplitude. For the TMF tests, the heating phase lasted 104 s, followed by cooling in air, 240 s total time. The temperature and strain histories are presented in Fig. 5.7 [A.1, A.9, A.11, A.12, A.14, A.15]. The thermal expansion coefficient was obtained from the five preceding heating-cooling cycles that were performed with zero load force.

5.4 New experimental results

The cyclic mechanical behaviour of SiMo is presented in Figs. 5.8-5.13 [A.1, A.3, A.9, A.15]. The stabilized hysteresis loops at mid-life for the LCF tests at 400°C and 650°C are presented in Fig. 5.8, and the stabilized hysteresis loops at 550°C and 750°C are presented in Fig. 5.10. The maximum and minimum stress as a function of the number of cycles is presented in Fig. 5.9 for LCF tests at 400°C and 650°C, and in Fig. 5.11 for LCF tests at 550°C and 750°C. The stabilized hysteresis loop at mid-life for the OP-TMF test between 100°C and 650°C is presented in Fig. 5.12. The evolution of the maximum, minimum and also mean stress with the number of cycles for the OP-TMF test is presented in Fig. 5.13 [A.1, A.3, A.9].

If we compare the LCF tests results in Figs. 5.9 and 5.11, we can observe cyclic hardening at and below 400°C, and cyclic softening for temperatures at and above 550°C [A.1, A.2, A.3, A.9]. Next, if we compare the peak (i.e. maximum) stresses for the stabilized hysteresis loops, we can see that the maximum stress at 400°C is almost 500 MPa, whereas at 750°C the maximum stress is about 75 MPa. The difference in terms of maximum stress during cyclic loading between 400°C and 750°C is over 400 MPa, and is significant. The significant decrease in maximum stress achieved during the LCF test, and also the transition between cyclic hardening and softening in the LCF tests can be observed at around 500°C. It should also be noted that the difference in the cyclic mechanical behaviour for temperatures below 400°C is almost negligible for the LCF tests.

Moreover, the cyclic mechanical response stabilizes after a few cycles in the case of the OP-TMF test, and no further hardening or softening is observed [A.1, A.9], Fig. 5.13. The OP-TMF tests were conducted between 100°C and 650°C. This leads to significant changes in the mechanical properties of the material during the loading cycle. As a result maximum stress of 476 MPa in tension is observed at the minimum temperature of the cycle, i.e. 100°C, minimum stress of 193 MPa in compression is observed at temperatures around 500°C, which was observed to be the temperature of transition between cyclic hardening and softening; and 76 MPa in compression at the maximum temperature of the cycle, i.e. 650°C, Fig. 5.12. Finally, a positive mean stress around 141 MPa is observed during the OP-TMF test.

The evolution of the elastic modulus with temperature for SiMo is presented in Fig. 5.16, where the values for a specific temperature are obtained by averaging the results obtained in the measured strain range [A.1]. A slowly decreasing trend can be observed in the elastic modulus between 20°C and 550°C. However, a great decrease is observed above 550°C, resulting in a 50% decrease at 750°C in comparison with 20°C. The results presented here also imply that the decrease in the elastic modulus with temperature is shifted by about 100°C towards the higher temperature in comparison with the temperature of transition between cyclic hardening and softening, which is equal to 500°C.

Fig. 5.14 [A.1] presents the results of the LCF tests with 300 s hold time in tension in the form of the evolution of the relaxed part of the stress in comparison with the total stress, i.e. the peak stress, with temperature. The relaxed part of the stress corresponds to the viscous part of the stress. Fig. 5.15 presents data obtained for the LCF test with

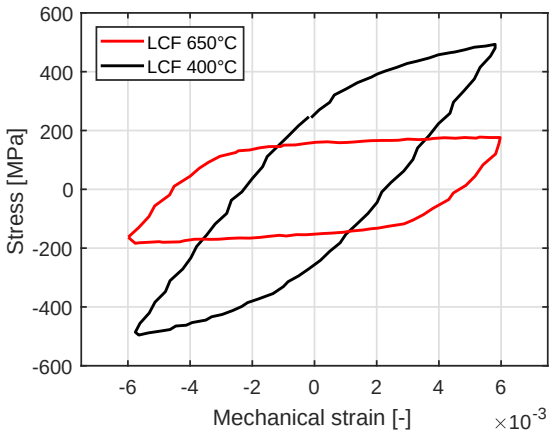

Figure 5.8: Stabilized hysteresis loops at 400°C and 650°C.

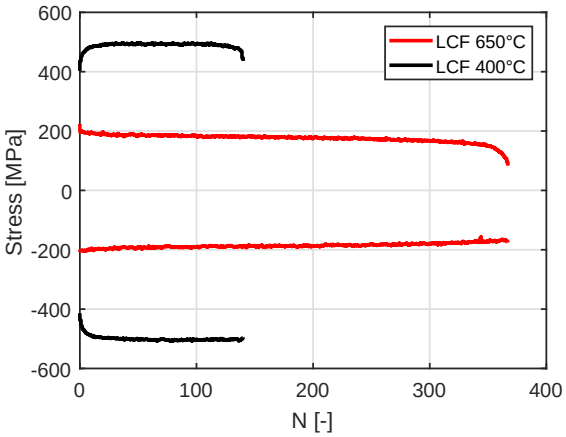

Figure 5.9: Maximum and minimum stress as a function of the number of cycles for the LCF tests at 400°C and 650°C..

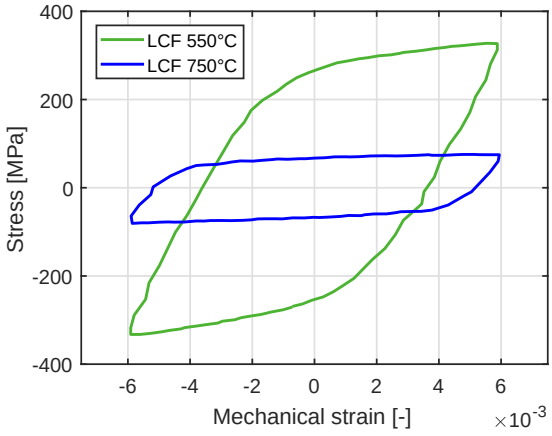

Figure 5.10: Stabilized hysteresis loops at 550°C and 750°C.

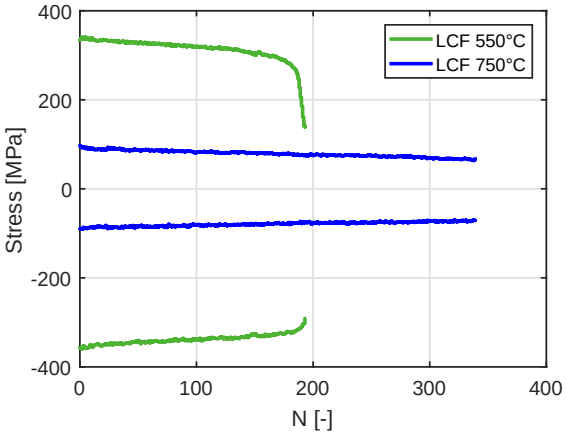

Figure 5.11: Maximum and minimum stress as a function of the number of cycles for the LCF tests at 550°C and 750°C.

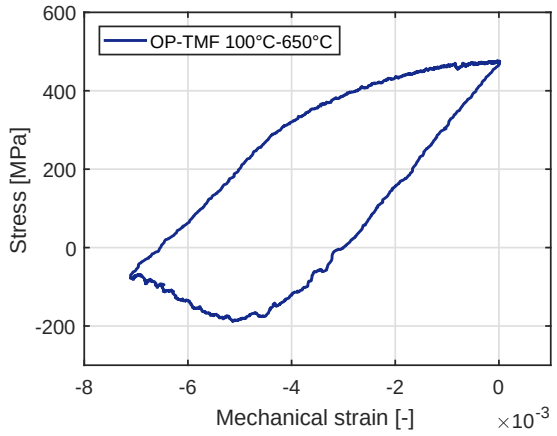

Figure 5.12: Stabilized hysteresis loop for the OP-TMF test between 100°C and 650°C.

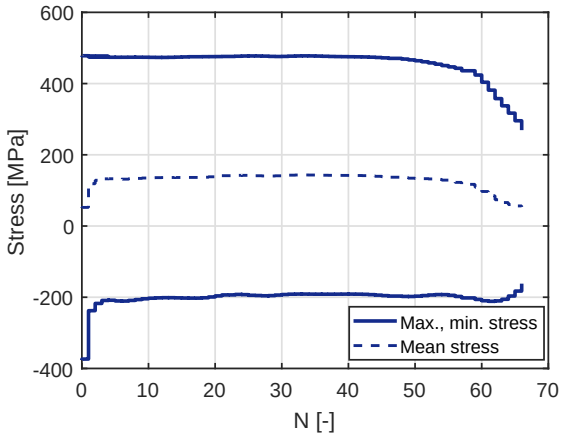

Figure 5.13: Maximum, minimum and mean stress as a function of the number of cycles for the OP-TMF test.

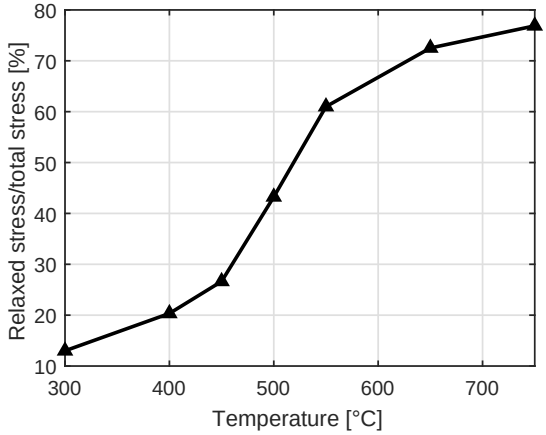

Figure 5.14: Evolution of the relaxed stress compared to the total stress with temperature in the LCF tests with a hold time in tension.

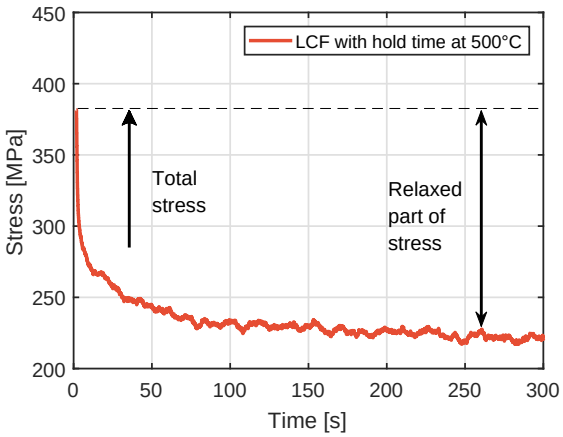

Figure 5.15: Cyclic relaxation test at 500°C.

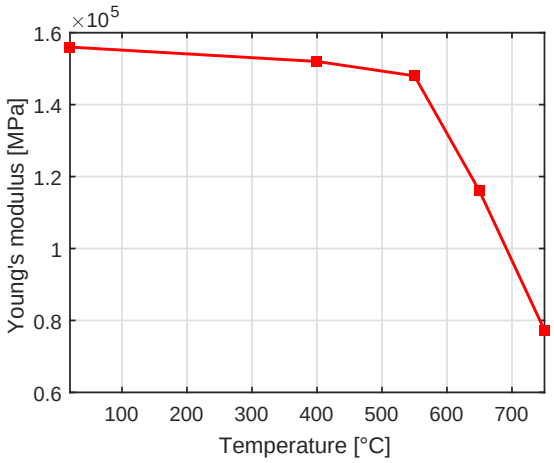

Figure 5.16: Evolution of the Young's modulus with temperature.

300 s hold time in tension at 500°C [A.1]. It can be observed that the relaxed part of the stress is more significant for temperatures above 500°C. At 750°C, the viscous stress is almost 80% of the total axial stress. By contrast, the viscous stress is almost negligible below 300°C. A purely elastic-plastic response is observed at room temperature.

The LCF results (without a hold time), and also the TMF results, for cylindrical specimens are presented in Tab. 5.2 [A.1, A.9, A.15], where w denotes the dissipated energy per cycle, $\Delta\varepsilon_m$ is the mechanical strain range and N_f are cycles to failure, determined when a 5% drop in peak stress occurred in comparison with the stabilized state. The dissipated energy per cycle, also known as the hysteresis energy, can be obtained by a numerical integration over the stabilized cycle, as follows:

$$w = \int_{cycle} \boldsymbol{\sigma} : \dot{\boldsymbol{\varepsilon}}_m dt, \tag{5.1}$$

where $\boldsymbol{\sigma}$ is the stress tensor and $\dot{\boldsymbol{\varepsilon}}_m$ is the mechanical strain rate tensor. The dissipated energy per cycle for the cylindrical specimens under LCF and TMF loading conditions was calculated from the experimental data at mid-life.

5.5 Discussion and conclusion

The in-house designed LCF/TMF test stand [A.1, A.9, A.11, A.12, A.13, A.16] presented here can be used for performing uniaxial TMF/LCF tests on cylindrical and notched specimens under passive cooling under ambient air. However, it is planned to install cooling air jets to ensure a faster cooling rate for the TMF tests. The proposed design is significantly less expensive than commercial LCF/TMF test stands.

Under uniaxial LCF loading conditions, SiMo 4.06 showed cyclic hardening below 500°C and cyclic softening above 500°C. The cylindrical specimens showed increasing durability in the high strain ranges with increasing test temperature. However, the durability for the low

Table 5.2: Summary of the LCF and TMF test results for specimens.

Specimen	Test	T [°C]	$\Delta\varepsilon_m$	w [J.mm^{-3}]	N_f
1	LCF	20	0.0051	0.14	33120
2	LCF	20	0.0078	1.32	777
3	LCF	20	0.0080	1.06	2089
4	LCF	20	0.0119	3.82	205
5	LCF	20	0.0120	4.71	110
6	LCF	20	0.0120	3.97	257
7	LCF	20	0.0159	7.40	61
8	LCF	20	0.0160	6.54	105
9	LCF	20	0.0204	10.83	47
10	LCF	20	0.0208	10.83	31
11	LCF	20	0.0244	13.57	14
12	LCF	400	0.0077	1.48	762
13	LCF	400	0.0079	1.46	377
14	LCF	400	0.0118	3.68	141
15	LCF	400	0.0121	4.73	30
16	LCF	400	0.0157	6.99	49
17	LCF	550	0.0051	0.72	3682
18	LCF	550	0.0080	2.09	481
19	LCF	550	0.0114	4.24	118
20	LCF	550	0.0120	4.09	158
21	LCF	550	0.0160	6.87	124
22	LCF	550	0.0197	9.52	102
23	LCF	550	0.0239	10.92	58
24	LCF	650	0.0049	0.54	4366
25	LCF	650	0.0075	1.22	1037
26	LCF	650	0.0078	1.48	877
27	LCF	650	0.0120	2.81	330
28	LCF	650	0.0200	5.17	129
29	LCF	650	0.0240	6.57	108
30	LCF	750	0.0047	0.31	1837
31	LCF	750	0.0077	0.65	1061
32	LCF	750	0.0119	1.35	340
33	LCF	750	0.0155	2.14	96
34	LCF	750	0.0197	2.93	192
35	LCF	750	0.0200	3.08	223
36	LCF	750	0.0239	2.92	136
37	OP-TMF	100-650	$-\Delta\varepsilon_{th}$	2.19	40
38	OP-TMF	100-650	$-\Delta\varepsilon_{th}$	1.94	59
39	OP-TMF	100-650	$-\Delta\varepsilon_{th}$	1.93	48

strain range tests decreased with increasing test temperature. The investigated material undergoes strong time-dependent effects with increasing temperature, as is observed in the relaxation tests. In addition, a significant decrease in the maximum axial stress during the loading cycle and in the elastic modulus with increasing temperature is observed for triangular LCF tests. The OP-TMF test results for cylindrical specimens demonstrate the negative effect of positive mean stress on the lifetime of SiMo 4.06. The lifetime is significantly reduced in comparison with the LCF test results for the same strain range or for the same dissipated energy per cycle [A.1, A.9].

The experimental results presented in this chapter will be further used for a calibration of constitutive material model in Chapter 6 and for fatigue analysis in Chapter 7.

Chapter 6

A unified viscoplastic material model

In this chapter, constitutive equations for unified viscoplastic Chaboche model with hyperbolic sine flow rule are given in Section 6.1. Then the model is implemented as a material subroutine for Abaqus finite element software. Numerical algorithm is based on implicit backward Euler integration. Consistent material tangent operator for the implemented constitutive material model is derived in this work and its effect on computational speed is shown for the numerical example, Section 6.2. The implemented viscoplastic material model is calibrated for the temperatures between 20°C and 650°C from the isothermal LCF tests, including the test with dwell time, that were obtained for the SiMo 4.06 cast iron. New experimental results for the lower strain rates are presented in this chapter in order to validate the material model. Fast engineering calibration procedure for the estimation of model parameters is proposed in this work. In addition, dependency between kinematic hardening parameters and temperature is suggested as Boltzmann function, Section 6.3. Then, the constitutive model is validated for the isothermal LCF tests obtained at different strain rates and for the out-of-phase TMF (OP-TMF) test. The results are presented in Section 6.4.

6.1 Viscoplastic constitutive material model

The first point is additive decomposition of the mechanical strain rate tensor, $\dot{\boldsymbol{\varepsilon}}$, into the elastic part, $\dot{\boldsymbol{\varepsilon}}^{\boldsymbol{e}}$, and into the inelastic part, $\dot{\boldsymbol{\varepsilon}}^{\boldsymbol{pl}}$, as follows:

$$\dot{\boldsymbol{\varepsilon}} = \dot{\boldsymbol{\varepsilon}}^{\boldsymbol{e}} + \dot{\boldsymbol{\varepsilon}}^{\boldsymbol{pl}}. \tag{6.1}$$

For the sake of simplicity, symbol $\boldsymbol{\varepsilon}$ denotes the mechanical strain tensor in this chapter. The stress rate tensor is obtained on the basis of the generalized Hooke law as:

$$\dot{\boldsymbol{\sigma}} = \boldsymbol{E} : \dot{\boldsymbol{\varepsilon}}^{\boldsymbol{e}}, \tag{6.2}$$

where $\boldsymbol{E}$ is the fourth order elasticity tensor, which is described here by the elastic modulus E and by the Poisson's ratio ν. The dissipation potential [48], denoted as Ω, is used to

obtain the effective viscoplastic strain rate, $\dot{p}$, in Eq. 6.3 and the inelastic strain tensor rate in Eq. 6.4.

$$\dot{p} = \frac{\partial \Omega}{\partial f} = \alpha \sinh\left(\beta f\right), \tag{6.3}$$

$$\dot{\boldsymbol{\varepsilon}}^{\boldsymbol{pl}} = \frac{\partial \Omega}{\partial \boldsymbol{\sigma}} = \frac{\partial \Omega}{\partial f}\frac{\partial f}{\partial \boldsymbol{\sigma}} = \dot{p}\boldsymbol{n} = \frac{3}{2}\dot{p}\frac{\boldsymbol{s} - \boldsymbol{x_D}}{J\left(\boldsymbol{\sigma} - \boldsymbol{x}\right)}, \tag{6.4}$$

where α and β are temperature and material dependent model parameters. $\boldsymbol{s}$ is the stress tensor deviator, and $\boldsymbol{n}$ is the tensor normal. $\boldsymbol{x}$ is the kinematic hardening tensor (backstress), and $\boldsymbol{x_D}$ is its deviator. It should be noted that backstress is a deviatoric quantity, i.e. $\boldsymbol{x} = \boldsymbol{x_D}$, so that there is no need to differentiate between the quantities. The stress function, f, is defined as:

$$f\left(\boldsymbol{\sigma} - \boldsymbol{x}\right) = J\left(\boldsymbol{\sigma} - \boldsymbol{x}\right) - k - R, \tag{6.5}$$

where k is the initial yield stress and R denotes the isotropic hardening or softening function. $f \leqslant 0$ defines the elastic domain and $\dot{p}$, in Eq. 6.3, is equal to zero, whereas for $f \geq 0$ the behaviour is viscoplastic and $\dot{p}$ is determined by the selected flow rule. $J\left(\boldsymbol{\sigma} - \boldsymbol{x}\right)$ is the von Mises invariant, defined as:

$$J\left(\boldsymbol{\sigma} - \boldsymbol{x}\right) = \left[\frac{3}{2}\left(\boldsymbol{s} - \boldsymbol{x_D}\right) : \left(\boldsymbol{s} - \boldsymbol{x_D}\right)\right]^{\frac{1}{2}} \tag{6.6}$$

The non-linear kinematic hardening model rule proposed by Chaboche [21, 22] states that the overall backstress (the kinematic hardening tensor) is composed of multiple backstress components, as follows:

$$\boldsymbol{x} = \sum_{i=1}^{N} \boldsymbol{x}_i. \tag{6.7}$$

The non-isothermal evolution law of the backstress component is defined as:

$$\dot{\boldsymbol{x_i}} = \frac{2}{3}C_i\dot{\boldsymbol{\varepsilon}}^{\boldsymbol{pl}} - \gamma_i \boldsymbol{x_i}\dot{p} + \frac{1}{C_i}\frac{\partial C_i}{\partial T}\boldsymbol{x_i}\dot{T} \tag{6.8}$$

where C_i and γ_i are temperature-dependent and material-dependent parameters. The first term in Eq. 6.8 corresponds to the linear kinematic hardening term. The second term is a recall term, and introduces nonlinearity into the evolution law. The last term is the temperature rate term.

The isotropic hardening (or softening) evolution used here is defined in a classical way as follows:

$$\dot{R} = b\left(Q - R\right)\dot{p} + \left(\frac{1}{b}\frac{\partial b}{\partial T} + \frac{1}{Q}\frac{\partial Q}{\partial T}\right)R\dot{T}, \tag{6.9}$$

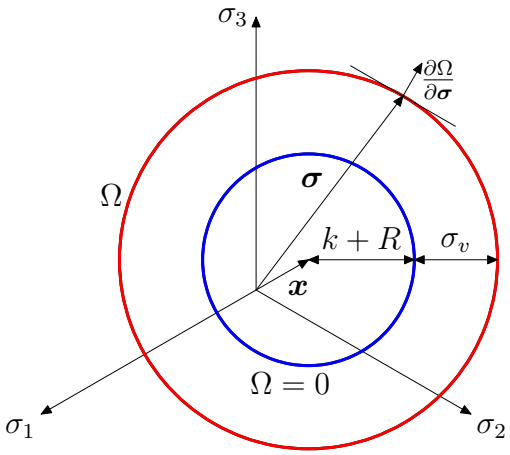

Figure 6.1: The elastic domain ($\Omega = 0$) and the viscoplastic domain (Ω) in 3D stress space.

where b and Q are temperature and material dependent parameters. The last term is the temperature rate term. The temperature terms in Eqs. 6.8 and 6.9 state that $\boldsymbol{x}$ and R also change, when inside elastic domain and change in temperature occurs.

Moreover, the rate-dependent (i.e. viscoplastic) behaviour is defined by $\Omega \geq 0$, whereas the rate-independent (i.e. plastic) behaviour is defined for $\Omega = 0$, Fig. 6.1. The viscoplastic potential surface, Ω, corresponds to the value of the overstress, σ_v, which is also known as the viscous part of the stress. σ_v defines the time-dependent part of the stress, and corresponds to the value of stress function f. The overall stress can be obtained by additive superposition of the backstress, $\boldsymbol{x}$, the initial yield stress k, the hardening function R, and the overstress σ_v.

6.2 FEM implementation of viscoplastic material model

6.2.1 Numerical integration of constitutive equations

The implicit integration scheme, which is also known as the radial return method, is used in this work [A.3, A.5]. The basic principle of this method is to obtain the trial stress increment on the basis of the generalized Hooke law under the assumption that the strain increment is purely elastic, i.e. the elastic predictor, and then to update the stress with the the plastic correction, i.e. the plastic corrector, if plastic behaviour is observed. The stress tensor can therefore be rewritten as [7, 32]:

$$\boldsymbol{\sigma} = \boldsymbol{\sigma}^{tr} - 2G\Delta p\boldsymbol{n}, \tag{6.10}$$

where G is the shear modulus, Δp denotes the increment in the effective viscoplastic strain and superscript $\boldsymbol{\sigma}^{tr}$ denotes the trial stress tensor. The von Mises equivalent stress σ_e can be obtained on the basis of the trial von Mises stress σ_e^{tr} as follows:

$$\sigma_e = J\left(\boldsymbol{\sigma} - \boldsymbol{x}\right) = \sigma_e^{tr} - 3G\Delta p \tag{6.11}$$

The trial von Mises stress is obtained as follows:

$$\sigma_e^{tr} = \left[\frac{3}{2}\left(\boldsymbol{s^{tr}} - \boldsymbol{x_D}\right) : \left(\boldsymbol{s^{tr}} - \boldsymbol{x_D}\right)\right]^{\frac{1}{2}}, \tag{6.12}$$

where $\boldsymbol{s^{tr}}$ is the deviatoric trial stress tensor. Then, the stress normal can be rewritten as a function of the trial quantities:

$$\boldsymbol{n} = \frac{3}{2}\frac{\boldsymbol{s} - \boldsymbol{x_D}}{J\left(\boldsymbol{\sigma} - \boldsymbol{x}\right)} = \frac{3}{2}\frac{\boldsymbol{s^{tr}} - \boldsymbol{x_D}}{J\left(\boldsymbol{\sigma^{tr}} - \boldsymbol{x}\right)}. \tag{6.13}$$

The effective viscoplastic strain increment is obtained as follows:

$$\dot{p} = \frac{\Delta p}{\Delta t} = \phi\left(\Delta p, \boldsymbol{x}, R\right) = \alpha \sinh \beta \left(\sigma_e^{tr} - 3G\Delta p - R - k\right) \tag{6.14}$$

Eq. 6.14 can be rewritten in the incremental form that can be employed for the Newton iterative method, which is used to obtain the increment in the effective viscoplastic strain:

$$\varphi = \Delta p - \phi\left(\Delta p, \boldsymbol{x}, R\right)\Delta t = 0 \tag{6.15}$$

Eq. 6.15 is a non-linear equation in effective viscoplastic strain Δp, which can be solved by the Newton iterative method:

$$\varphi + \frac{\partial \varphi}{\partial \Delta p}\Delta p + \frac{\partial \varphi}{\partial \boldsymbol{x}} : d\boldsymbol{x} + \frac{\partial \varphi}{\partial R}dR = 0 \tag{6.16}$$

Rearranging Eq. 6.16 gives:

$$\varphi + \left(1 - \frac{\partial \phi}{\partial \Delta p}\Delta t\right)\Delta p - \frac{\partial \phi}{\partial \boldsymbol{x}}\Delta t : d\boldsymbol{x} - \frac{\partial \phi}{\partial R}\Delta t dR = 0 \tag{6.17}$$

Evaluating the partial derivatives in Eq. 6.17 gives:

$$\frac{\partial \phi}{\partial \Delta p} = -3G\alpha\beta \cosh \beta \left(\sigma_e^{tr} - 3G\Delta p - R - k\right) = -3GZ \tag{6.18}$$

$$\frac{\partial \phi}{\partial \boldsymbol{x}} = -\frac{\partial \phi}{\partial \sigma_e}\frac{\partial \sigma_e}{\partial \boldsymbol{x}} = -\alpha\beta \cosh \beta \left(\sigma_e^{tr} - 3G\Delta p - R - k\right)\boldsymbol{n} = -Z\boldsymbol{n} \tag{6.19}$$

$$\frac{\partial \phi}{\partial R} = -\alpha\beta \cosh \beta \left(\sigma_e^{tr} - 3G\Delta p - R - k\right) = -Z \tag{6.20}$$

Substituting Eq. 6.15 and the partial derivatives from Eqs. 6.18,6.19 and 6.20 into Eq. 6.17 gives the iterative form [7]:

$$d\Delta p = \frac{\phi - (\Delta p/\Delta t) - Z\boldsymbol{n} : \boldsymbol{x_i}\frac{1}{C_i}\frac{\partial C_i}{\partial T}\Delta T - Z\left(\frac{1}{b}\frac{\partial b}{\partial T} + \frac{1}{Q}\frac{\partial Q}{\partial T}\right)RdT}{\frac{1}{\Delta t} + 3GZ + ZC_i - Z\boldsymbol{n} : \boldsymbol{x_i}\gamma_i + Zb\,(Q-R)} \tag{6.21}$$

$$\Delta p = \Delta p + d\Delta p \tag{6.22}$$

The increment in the effective viscoplastic strain, Eq. 6.22, is updated until convergence is obtained. It should be noted that the stress normal, Eq. 6.32, isotropic hardening function R and backstress $\boldsymbol{x}$ are refreshed in each iteration for the implicit integration scheme. The increments in R and $\boldsymbol{x}$ are obtained on the basis of the effective viscoplastic strain increment, as follows:

$$\Delta R = \frac{b\,(Q - R^t)\,\Delta p}{1 + b\Delta p} + \frac{\left(\frac{1}{b}\frac{\partial b}{\partial T} + \frac{1}{Q}\frac{\partial Q}{\partial T}\right)R^t\Delta T}{1 - \left(\frac{1}{b}\frac{\partial b}{\partial T} + \frac{1}{Q}\frac{\partial Q}{\partial T}\right)\Delta T} \tag{6.23}$$

$$\Delta \boldsymbol{x}_i = \frac{\frac{2}{3}C_i\Delta p\boldsymbol{n} - \gamma_i\boldsymbol{x}_i^t\Delta p + \frac{1}{C_i}\frac{\partial C_i}{\partial T}\Delta T\boldsymbol{x}_i^t}{1 + \gamma_i\Delta p - \frac{1}{C_i}\frac{\partial C_i}{\partial T}\Delta T} \tag{6.24}$$

where the quantities with superscript ^{t} denote values from the previous increment. Eqs. 6.23 and 6.24 states that the values of R and $\boldsymbol{x}$ also change when only the temperature changes [A.3, A.5].

Moreover, when the increment in the effective viscoplastic strain, Δp, is obtained, the increment in the plastic strain tensor, $\Delta\boldsymbol{\varepsilon}^{pl}$, can be obtained on the basis of Eq. 6.4. The increment in the elastic strain tensor is obtained as:

$$\Delta\boldsymbol{\varepsilon}^e = \Delta\boldsymbol{\varepsilon} - \Delta\boldsymbol{\varepsilon}^{pl} \tag{6.25}$$

Finally, the stress increment is obtained on the basis of the generalized Hooke law as follows:

$$\Delta\boldsymbol{\sigma} = \boldsymbol{E} : \Delta\boldsymbol{\varepsilon}^e \tag{6.26}$$

6.2.2 Consistent material tangent operator

When implementing the material model within finite element software such as Abaqus, the user needs to provide a material subroutine that contains integration of the constitutive equations together with the Jacobian matrix, i.e. a material tangent operator that is used in the global Newton method in minimizing the force residual. The consistent material

tangent operator should be used in order to preserve the quadratic convergence of the global Newton method. The formulation of the consistent material tangent operator depends on the integration scheme that is selected, and on the constitutive equations. It should be noted that a consistent material tangent operator for complex material models sometimes cannot be derived analytically, Approximate Jacobian matrices are therefore often used for these cases. In this study, the consistent material tangent operator is analytically derived on the basis of the implicit integration scheme that is used [A.3, A.5].

The following equations are used throughout the derivation of the consistent material tangent operator. Applying differential operator δ to Eqs. 6.10 and 6.11 gives:

$$\delta\sigma_e^{tr} = \delta\sigma_e + 3G\delta\Delta p = \boldsymbol{n} : \delta\left(\boldsymbol{s}^{tr} - \boldsymbol{x}\right), \tag{6.27}$$

$$\delta\boldsymbol{\sigma} = \delta\boldsymbol{\sigma}^{tr} - 2G\delta\Delta p\boldsymbol{n}. \tag{6.28}$$

Eq. 6.28 can be written for the deviatoric stress tensor, as follows:

$$\delta\boldsymbol{s} = \delta\boldsymbol{s}^{tr} - 2G\delta\Delta p\boldsymbol{n}. \tag{6.29}$$

The deviatoric stress tensor can be written in terms of the stress tensor and the strain tensor as:

$$\delta\boldsymbol{s} = \delta\boldsymbol{\sigma} - K\boldsymbol{I}\boldsymbol{I} : \delta\boldsymbol{\varepsilon}, \tag{6.30}$$

and the trial deviatoric stress tensor can be written in terms of the strain tensor:

$$\delta\boldsymbol{s}^{tr} = 2G\delta\boldsymbol{\varepsilon} - \frac{2}{3}G\left(\delta\boldsymbol{\varepsilon} : \boldsymbol{I}\right)\boldsymbol{I} \tag{6.31}$$

where K is the bulk modulus and $\boldsymbol{I}$ denotes the identity matrix.

The first point in the derivation of the consistent material tangent operator is the stress tensor normal:

$$\frac{3}{2}\frac{\boldsymbol{s} - \boldsymbol{x_D}}{\sigma_e} = \frac{3}{2}\frac{\boldsymbol{s^{tr}} - \boldsymbol{x_D}}{\sigma_e^{tr}} \tag{6.32}$$

It is admissible to write $\boldsymbol{x}$ instead of $\boldsymbol{x_D}$, as the backstress tensor is deviatoric by nature. Rearranging Eq. 6.32 gives:

$$\boldsymbol{s} = \boldsymbol{x} + \frac{\sigma_e}{\sigma_e^{tr}}\left(\boldsymbol{s}^{tr} - \boldsymbol{x}\right) \tag{6.33}$$

Applying the differential operator to Eq. 6.33 gives the following form:

$$\delta\boldsymbol{s} = \left(1 - \frac{\sigma_e}{\sigma_e^{tr}}\right)\delta\boldsymbol{x} + \frac{\sigma_e}{\sigma_e^{tr}}\delta\boldsymbol{s}^{tr} + \frac{\boldsymbol{s}^{tr} - \boldsymbol{x}}{\sigma_e^{tr}}\left(\frac{\sigma_e^{tr}\delta\sigma_e - \sigma_e\delta\sigma_e^{tr}}{\sigma_e^{tr}}\right) \tag{6.34}$$

Eq. 6.34 can be rewritten after rearrangement as:

$$\begin{gathered}\delta\sigma = K\boldsymbol{II} : \delta\boldsymbol{\varepsilon} + \frac{\sigma_e}{\sigma_e^{tr}}\left(2G\delta\boldsymbol{\varepsilon} - \frac{2}{3}G\boldsymbol{II} : \delta\boldsymbol{\varepsilon}\right) + \left(1 - \frac{\sigma_e}{\sigma_e^{tr}}\right) \\ \left(\frac{2}{3}C_i\delta\Delta p\boldsymbol{n} - \gamma_i\boldsymbol{x_i}\delta\Delta p + \frac{1}{C_i}\frac{\partial C_i}{\partial T}\boldsymbol{x_i}\Delta T\right) + \frac{\boldsymbol{s}^{tr} - \boldsymbol{x}}{\sigma_e^{tr}}\left(\delta\sigma_e - \frac{\sigma_e}{\sigma_e^{tr}}\delta\sigma_e^{tr}\right)\end{gathered} \tag{6.35}$$

At this point, the derivation of $\delta\Delta p$ in Eq. 6.35 is required. The increment in the effective viscoplastic strain is obtained on the basis of the selected flow rule, written in a general form as:

$$\Delta p = \phi\left(\boldsymbol{\sigma}, \boldsymbol{x}, R\right)\Delta t \tag{6.36}$$

Applying the differential operator in Eq. 6.36 gives:

$$\delta\Delta p = \left(\frac{\partial\phi}{\partial\boldsymbol{\sigma}} : \delta\boldsymbol{\sigma} + \frac{\partial\phi}{\partial\boldsymbol{x}} : \delta\boldsymbol{x} + \frac{\partial\phi}{\partial R}\delta R\right)\Delta t \tag{6.37}$$

The partial derivatives in Eq. 6.37 can be expressed as:

$$\begin{gathered}\frac{\partial\phi}{\partial R} = -\alpha\beta\cosh\left(\sigma_e^{tr} - 3G\Delta p - R - k\right) = -Y \\ \frac{\partial\phi}{\partial\boldsymbol{x}} = \frac{\partial\phi}{\partial\sigma_e}\frac{\partial\sigma_e}{\partial\boldsymbol{x}} = -Y\boldsymbol{n} \\ \frac{\partial\phi}{\partial\boldsymbol{\sigma}} = \frac{\partial\phi}{\partial\sigma_e}\frac{\partial\sigma_e}{\partial\boldsymbol{\sigma}} = Y\boldsymbol{n}\end{gathered} \tag{6.38}$$

Substituting the partial derivatives from Eq. 6.38 into Eq. 6.37 gives, after rearrangement [A.3, A.5]:

$$\delta\Delta p = \frac{Y\boldsymbol{n} : \delta\boldsymbol{\sigma}^{tr} + Y\boldsymbol{n} : \frac{1}{C_i}\frac{\partial C_i}{\partial T}\boldsymbol{x}_i\Delta T - Y\left(\frac{1}{b}\frac{\partial b}{\partial T} + \frac{1}{Q}\frac{\partial Q}{\partial T}R\Delta T\right)}{\frac{1}{\Delta t} + 3GY + YC_i - Y\boldsymbol{n} : \boldsymbol{x}_i\gamma_i + Yb\left(Q - R\right)} = \frac{Y}{D}\boldsymbol{n} : \delta\boldsymbol{\sigma}^{tr} + \frac{H}{D} \tag{6.39}$$

Substituting $\delta\Delta p$ from Eq. 6.39 into Eq. 6.35 and rearranging gives [A.3, A.5]:

$$\begin{gathered}\delta\boldsymbol{\sigma} = Z_1\delta\boldsymbol{\varepsilon} + Z_2\boldsymbol{II} : \delta\boldsymbol{\varepsilon} + \boldsymbol{n}Z_3\boldsymbol{n}\delta\boldsymbol{\varepsilon} + \boldsymbol{n}\left(\boldsymbol{n} : I\right)Z_4\boldsymbol{I} : \boldsymbol{\varepsilon} - \boldsymbol{x}_iZ_{5i}\boldsymbol{n} : \boldsymbol{\varepsilon} + \\ \boldsymbol{x}_iZ_{6i}\left(\boldsymbol{n} : \boldsymbol{I}\right) : \delta\boldsymbol{\varepsilon} + \left(\boldsymbol{s}^{tr} - \boldsymbol{x}\right)Z_7\boldsymbol{n} : \delta\boldsymbol{\varepsilon} - \left(\boldsymbol{s}^{tr} - \boldsymbol{x}\right)Z_8\left(\boldsymbol{n} : \boldsymbol{I}\right)\boldsymbol{I} : \delta\boldsymbol{\varepsilon} + \\ \left(1 - \frac{\sigma_e}{\sigma_e^{tr}}\right)\left[\frac{H}{D}\left(\frac{2}{3}C_i\boldsymbol{n} - \gamma_i\boldsymbol{x}_i\right) + \frac{1}{C_i}\frac{\partial C_i}{\partial T}\boldsymbol{x}_i\Delta T\right] + \\ \frac{\boldsymbol{s}^{tr} - \boldsymbol{x}}{\sigma_e^{tr}}\left[\frac{H}{D}\left(1 - \frac{\sigma_e}{\sigma_e^{tr}}\right)\left(C_i - \gamma_i\boldsymbol{n} : \boldsymbol{x}_i\right) + \frac{H}{D}3G - \left(1 - \frac{\sigma_e}{\sigma_e^{tr}}\right)\frac{1}{C_i}\frac{\partial C_i}{\partial T}\boldsymbol{n} : \boldsymbol{x}_i\Delta T\right]\end{gathered} \tag{6.40}$$

The terms used in Eq. 6.40 are listed below [A.3, A.5]:

$$
\begin{aligned}
Z_1 &= \frac{\sigma_e}{\sigma_e^{tr}} 2G \\
Z_2 &= \left(K - \frac{2}{3} G \frac{\sigma_e}{\sigma_e^{tr}} \right) \\
Z_3 &= \left(1 - \frac{\sigma_e}{\sigma_e^{tr}} \right) \frac{2}{3} C_i \frac{Y}{D} 2G \\
Z_4 &= \left(1 - \frac{\sigma_e}{\sigma_e^{tr}} \right) \frac{2}{3} C_i \frac{Y}{D} \left(\frac{2}{3} G - K \right) \\
Z_{5i} &= \gamma_i \left(1 - \frac{\sigma_e}{\sigma_e^{tr}} \right) 2G \frac{Y}{D} \\
Z_{6i} &= \gamma_i \frac{Y}{D} \left(\frac{2}{3} G - K \right) \left(1 - \frac{\sigma_e}{\sigma_e^{tr}} \right) \\
Z_7 &= \frac{1}{\sigma_e^{tr}} \left[\frac{2}{3} G \left(1 - \frac{\sigma_e}{\sigma_e^{tr}} \right) - \left(1 - \frac{\sigma_e}{\sigma_e^{tr}} \right) 2G \frac{Y}{D} \left(C_i - \gamma_i \boldsymbol{n} : \boldsymbol{x}_i \right) - 6G^2 \frac{Y}{D} \right] \\
Z_8 &= \frac{1}{\sigma_e^{tr}} \left[\frac{2}{3} G \left(1 - \frac{\sigma_e}{\sigma_e^{tr}} \right) - \left(1 - \frac{\sigma_e}{\sigma_e^{tr}} \right) \left(\frac{2}{3} G - K \right) \frac{Y}{D} \left(C_i - \gamma_i \boldsymbol{n} : \boldsymbol{x}_i \right) - 3G \left(\frac{2}{3} G - K \right) \frac{Y}{D} \right]
\end{aligned}
\tag{6.41}
$$

Finally, the Jacobian matrix is obtained from Eq. 6.40, as follows:

$$
\boldsymbol{J} = \frac{\partial \delta \boldsymbol{\sigma}}{\partial \delta \boldsymbol{\varepsilon}} \tag{6.42}
$$

It should be noted that the temperature dependent terms, H/D, in Eq. 6.40 vanish after the application of a partial derivative in Eq. 6.42 as they are independent on $\delta\boldsymbol{\varepsilon}$ [A.3, A.5].

6.3 A novel calibration of viscoplastic material model

In this section, the implemented material model is calibrated from the LCF experimental data that were obtained for SiMo 4.06 [A.1, A.3, A.9, A.11, A.14, A.15]. The model is used for a numerical description of the cyclic mechanical behaviour of the studied material using FEM. The selected constitutive material model requires ten temperature-dependent material parameters to be calibrated: $k, E, C_{1-3}, \gamma_{1-3}, \alpha, \beta$. The Poisson ratio ν is set to a constant value equal to 0.28. The material parameters are obtained by a step-by-step procedure from the available experimental data [A.3, A.5]. The key assumption is that the kinematic hardening parameters, viscous parameters and isotropic hardening parameters can be calibrated separately and only the value of yield stress is corrected for each step in calibration process [24]. The triangular isothermal tests and the triangular isothermal tests with hold time are sufficient for the calibration of the selected material model, therefore

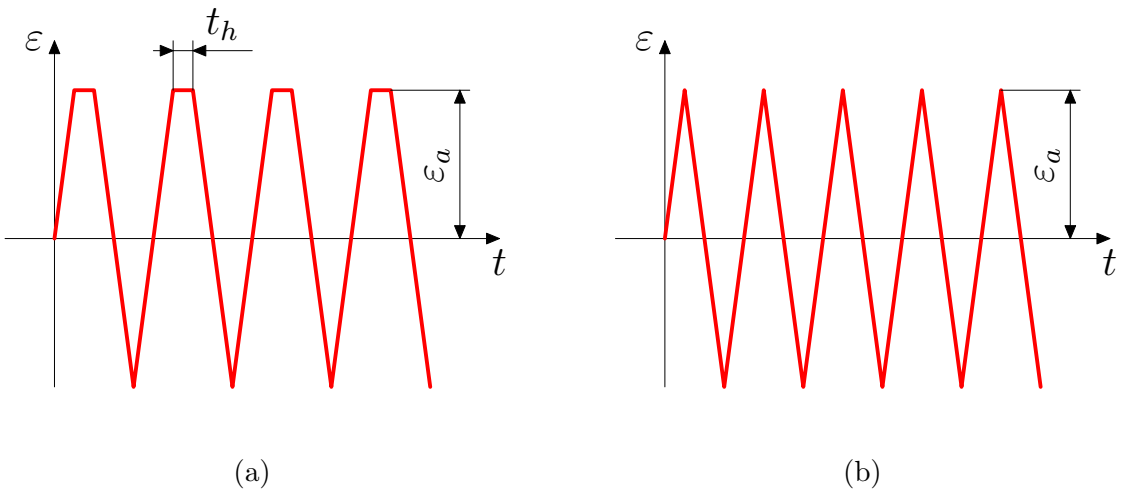

(a) (b)

Figure 6.2: Isothermal triangular LCF loading history with the hold time in tension (a) and without the hold time (b).

the material model is calibrated from the triangular isothermal LCF tests obtained at strain rate $\dot{\varepsilon} = 0.003\ s^{-1}$ and from the isothermal LCF tests with hold time in tension $t_h = 300\ s$, both tests were attained at four different temperatures between 20°C and 650°C and for the mechanical strain amplitude $\varepsilon_a = 0.006$, Figs. 6.2a and 6.2b [A.3, A.5]. The TMF tests, which were performed as out-of-phase and LCF tests that were performed at different strain rates are used for the validation purposes in the next section. The more detailed description of the experimental set-up and the experimental results for the SiMo 4.06 was given in Chapter 5, except the experimental results for the LCF tests performed at different strain rates, which were additionally performed for this study.

The first step is to calibrate the elastic modulus. The elastic modulus was calibrated from the unloading parts of the above-mentioned stress-strain hysteresis loops at mid-life of the LCF tests obtained at the temperatures 20°C, 400°C, 550°C and 650°C. The end-life was determined when 5% drop in tensile load occurred in comparison with the stabilized state. The temperature dependent elastic modulus was calibrated to follow a monotonic downward trend on temperature [A.2, A.3, A.4, A.5, A.7, A.8, A.10, A.11, A.15], as follows:

$$E = e_{01}\left(1 - e_{02}\exp\left(\frac{T}{e_{03}}\right)\right), \tag{6.43}$$

where e_{01-03} are the calibrated parameters.

The next step is to determine the kinematic hardening properties. First, for the purposes of calibration, time-independent plasticity is assumed. The kinematic hardening parameters are calibrated on the basis of stabilized state at mid-life. Here, the number of backstress terms is considered to be 3. The tensile part of the corresponding hysteresis curve can therefore be written as follows:

$$\sigma = k'' + \frac{C_1}{\gamma_1}\left(1 - 2\exp\left(-\gamma_1\varepsilon_{pl}\right)\right) + \frac{C_2}{\gamma_2}\left(1 - 2\exp\left(-\gamma_2\varepsilon_{pl}\right)\right) + C_3, \varepsilon_{pl} \tag{6.44}$$

where ε_{pl} is the uniaxial inelastic strain. k'' is the yield stress that meanwhile also incorporates the viscous part of the stress, because the tests were performed at a constant strain rate.

In this study, temperature dependent non-linear kinematic hardening parameters C_{1-3} and γ_{1-2} were calibrated to follow a monotonic downward trend at temperature, T, described mathematically as the Boltzmann function [A.2, A.3, A.4, A.5, A.7, A.8, A.10, A.11, A.14, A.15]:

$$C_{1-3}(T) = \frac{a_{01-03} - a_{04-06}}{1 + \exp(\frac{T - a_{07}}{a_{08}})} + a_{04-06} \tag{6.45}$$

$$\gamma_{1-2}(T) = \frac{b_{01-02} - b_{03-04}}{1 + \exp(\frac{T - b_{05}}{b_{06}})} + b_{03-04} \tag{6.46}$$

where a_{01-08} and b_{01-06} are the calibrated parameters. γ_3 is considered to be zero. In the calibration process, five stabilized hysteresis loops for different temperatures at mid-life, at strain rate $\dot{\varepsilon} = 0.003s^{-1}$ for mechanical strain amplitude $\varepsilon_a = 0.006$, were selected from the isothermal LCF tests. The hysteresis loop obtained at 750°C was additionally used for calibrating the kinematic hardening parameters. The principle was to search the global minimum of the objective function, which was defined as the sum of squares of the percentage differences between the tested and the simulated stress. In addition, a general rule for kinematic hardening parameters was used in the process for calibrating the kinematic hardening parameters: $C_1 \gg C_2 \gg C_3$ and $\gamma_1 \gg \gamma_2 \gg \gamma_3$. The first backstress term represents the large (initial) plastic modulus of the stress-strain curve, and the second term corresponds to a moderate segment of stress-strain curve. Finally, the third term describes the constant hardening observed for large strains [48], Fig. 6.3. The kinematic parameters calibrated in such way were also used for two-layer viscoplastic material model in [A.2, A.4] or elastic-plastic material model in [A.4, A.8, A.10].

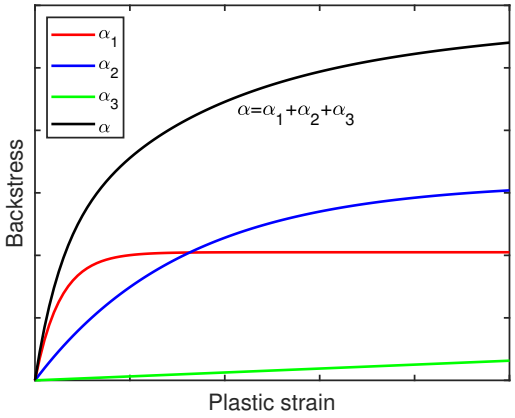

Figure 6.3: The additive superposition of individual backstress components.

The next step is to determine the temperature-dependent viscous parameters from the isothermal LCF tests with the hold time in tension. The mechanical strain is constant during the hold period of the test:

$$\dot{\varepsilon} = \dot{\varepsilon}_{el} + \dot{\varepsilon}_{pl} = 0. \tag{6.47}$$

The stress can also be decomposed for the uniaxial isothermal loading case, as follows:

$$\sigma = x + R + k + \sigma_v. \tag{6.48}$$

The stress as a function of time during the strain hold period can be derived analytically from Eq. 6.47 for the uniaxial case as follows:

$$\sigma\left(t\right) = x + R + k + \frac{2}{\beta}\tanh^{-1}\left(\tanh\left(\frac{\beta\left(\sigma_{peak} - x - R - k\right)}{2}\right)e^{-\alpha\beta E t}\right), \tag{6.49}$$

where σ_{peak} is the maximum stress value, i.e. the value of stress at the start of the dwell period. Moreover, the strain rate is related to the viscous part of the stress for the uniaxial case, as follows:

$$\sigma_v = \frac{1}{\beta}\sinh^{-1}\left(\frac{\dot{\varepsilon}_0}{\alpha}\right), \tag{6.50}$$

where $\dot{\varepsilon}_0$ is the uniaxial strain rate. Eq. 6.49 can therefore be rearranged for the purposes of calibration, as follows:

$$\sigma\left(t\right) = \sigma_{peak} - \sigma_{0v} + \frac{2}{\beta}\tanh^{-1}\left(\tanh\left(\frac{\beta\sigma_{0v}}{2}\right)exp\left(\frac{-\beta E\dot{\varepsilon}_0 t}{\sinh\left(\beta\sigma_{0v}\right)}\right)\right), \tag{6.51}$$

where $\dot{\varepsilon}_0$ is the uniaxial strain rate during the loading and unloading part of the cycle, which is constant for the triangular waveform and is equal to 0.003 for the cycles with the hold period in this study. σ_{0v} is the viscous stress value generated during the loading period of the cycle and is also equal to the stress that can be relaxed during the dwell period. The value of $\sigma_{peak} - \sigma_{0v}$ is equal to $x + R + k$ [A.3, A.5].

Then the calibrated parameters are the viscous part of the stress σ_{0v} and β. They are obtained by the non-linear least square method from the experimental data, and the value of α is then obtained on the basis of Eq. 6.50. However the value of σ_{0v} should be chosen carefully. It can be observed that the viscous parameters can be obtained separately from the other material model parameters [A.3, A.5]. Moreover, the variation of β is presented in Fig. 6.4, where the value of α is computed on the basis of Eq. 6.50, so that the value σ_{0v} is kept constant. Parameter β controls the rate of stress relaxation during the dwell period. The parameters related to the viscous behaviour are calibrated for each temperature separately, and are then interpolated in this study [A.3, A.5]. The initial value of yield stress k'' should be corrected after the parameters controlling viscous behaviour have been estimated, i.e. $k' = k'' - \sigma_{0v}$.

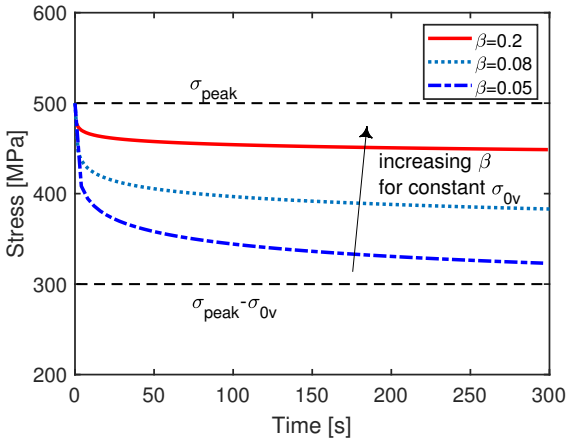

Figure 6.4: The variation of viscous parameter β for a constant relaxed stress value.

The last step in the calibration process is to determine the isotropic hardening properties, Q and b. The evolution of isotropic hardening or softening function R with accumulated inelastic strain p can be derived explicitly from Eq. 6.9 for the isothermal case as follows:

$$R(p) = Q\left(1 - e^{-bp}\right). \tag{6.52}$$

Parameter Q defines the saturated value of R, and parameter b controls the saturation rate. The initial values of b and Q can be obtained directly from the experimental data. The accumulated inelastic strain p can be written as a function of the number of loading cycles N:

$$p(N) \approx 2N\Delta\varepsilon_{pl}, \tag{6.53}$$

where the inelastic strain range value $\Delta\varepsilon_{pl}$ can be obtained for each loading cycle from the available experimental data. The values of the isotropic hardening parameters of b and Q can therefore be obtained by fitting Eq. 6.52 to the experimental data. This usually provides reasonable accuracy, but the parameters can be optimized the parameters e.g. by linking Abaqus with the Matlab optimization toolbox with the Python script. It should be noted that the final yield stress value k must be calibrated together with the isotropic hardening parameters, i.e. the value k' obtained from the previous calibration step needs to be changed within this step [A.3, A.5].

6.4 Results

6.4.1 Cyclic mechanical behaviour of SiMo 4.06

The constitutive material model parameters were estimated by a step-by-step procedure [A.3, A.5]. The temperature dependent kinematic hardening parameters were determined from the stabilized hysteresis loops at mid-life, which were obtained at five different temperatures for mechanical strain amplitude $\varepsilon_a = 0.006$ and mechanical strain rate $\dot{\varepsilon} = 0.003\ s^{-1}$. The temperature-dependent kinematic hardening parameters are presented in Tab.6.1 [A.2, A.3, A.5, A.8, A.15], and plotted in Figs. 6.6a-6.6e. The parameters follow a monotonic trend, described mathematically as the Boltzmann function, Eqs. 6.45 and 6.46. The hysteresis loops for temperatures of 20°C, 400°C, 550°C and 650°C were also used in order to obtain temperature-dependent isotropic hardening parameters, the elastic modulus and the yield stress, Tab.6.2 [A.3, A.5]. The temperature-dependent elastic modulus is presented in Fig. 6.5. It should be noted that the values presented in previous chapter for the whole measured strain range. Finally, the temperature-dependent viscous parameters were obtained from isothermal LCF tests with a hold time in tension, which were obtained for various temperatures between 300°C and 650°C, Tab.6.3.

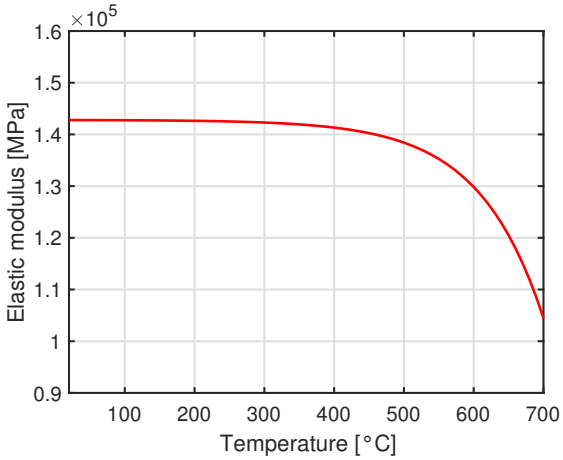

Figure 6.5: The temperature-dependent elastic modulus.

In addition, the viscous part of the stress at 20°C is close to zero. The viscous parameter values for 20°C are added therefore artificially, so that the response at this temperature is elastic-plastic. The values of the constitutive model parameters between the test temperatures are obtained by interpolation, i.e. the values of the isotropic hardening parameters and the viscous parameters, Tab.6.2 and Tab.6.3 [A.3, A.5].

The simulated and experimental hysteresis loops [A.1, A.3, A.5] at 20°C in the 10th and 100th cycle for mechanical strain rate $\dot{\varepsilon} = 0.003\ s^{-1}$ are presented in Figs. 6.7a and 6.7b, respectively. The simulated and experimental results are presented in Figs. 6.8a and 6.8b for 400°C, and in Figs. 6.9a and 6.9b for 550°C. Finally, the simulated and experimental

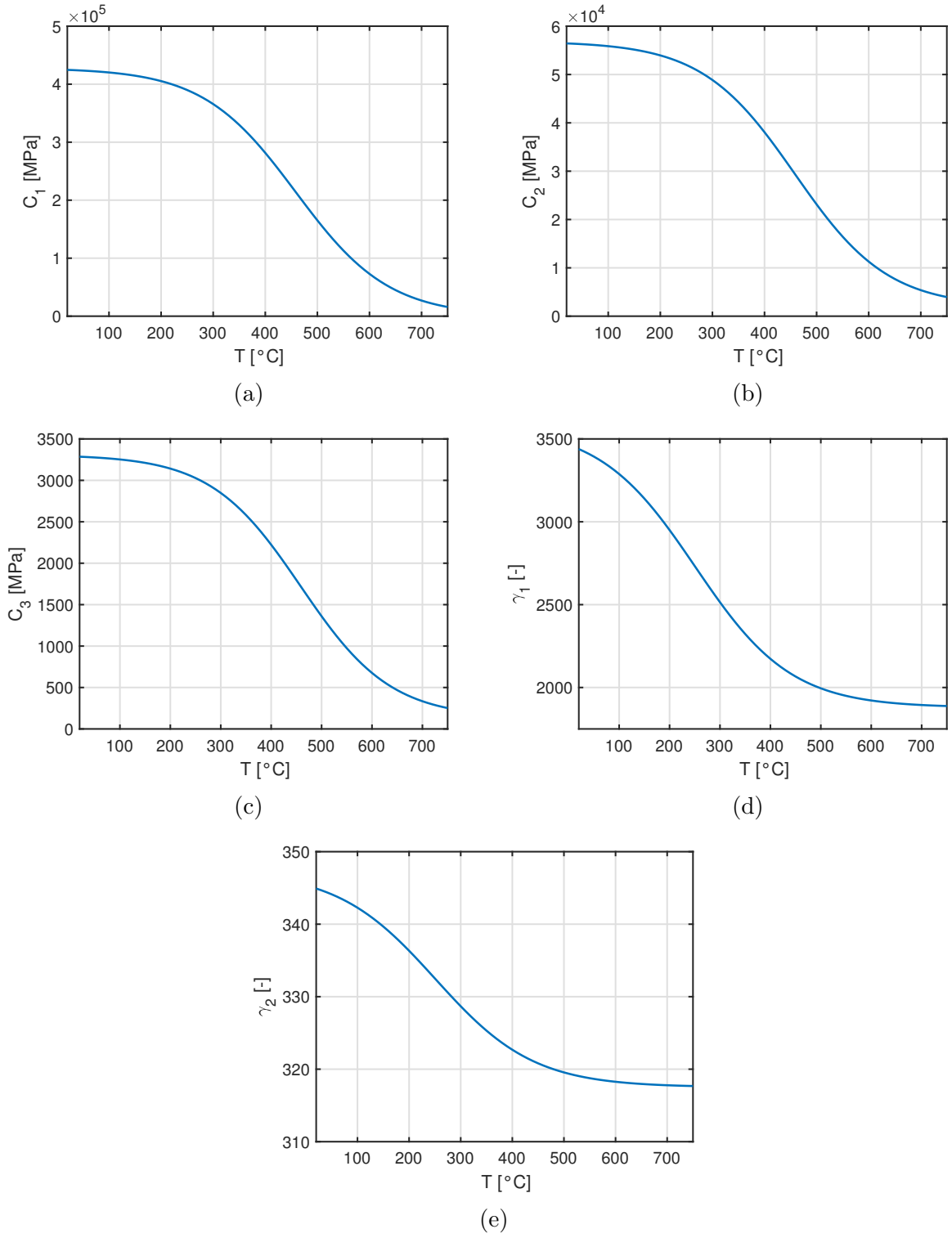

Figure 6.6: Temperature dependency of the kinematic hardening parameter C_1 (a), C_2 (b), C_3 (c), γ_1 (d) and γ_2 (e).

Table 6.1: Temperature dependent kinematic hardening parameters for SiMo 4.06.

$T\ [°C]$	$C_1\ [MPa]$	γ_1	$C_2\ [MPa]$	γ_2	$C_3\ [MPa]$	γ_3
20	424658.51	3438.77	56437.38	344.92	3285.50	0
400	281526.14	2173.07	38064.26	322.68	2223.43	0
550	113148.59	1949.75	16450.56	318.76	974.02	0
650	44991.81	1904.61	7701.65	317.96	468.28	0
750	15826.97	1888.21	3957.92	317.67	251.87	0

Table 6.2: Temperature dependent elastic modulus, yield stress and isotropic hardening parameters for SiMo 4.06.

$T\ [°C]$	$E\ [MPa]$	$k\ [MPa]$	b	$Q\ [MPa]$
20	142775.88	256.71	0.306	42.64
400	141316.16	127.79	15.951	49.69
550	135256.78	37.33	0.501	-33.09
650	120498.37	18.85	0.715	-18.75

Table 6.3: Temperature dependent viscous parameters for SiMo 4.06.

$T\ [°C]$	$\alpha\ [s^{-1}]$	$\beta\ [MPa^{-1}]$
20	5.939E-06	0.900
300	5.939E-06	0.116
400	6.080E-07	0.092
500	1.892E-06	0.050
550	3.929E-06	0.035
650	2.451E-05	0.042

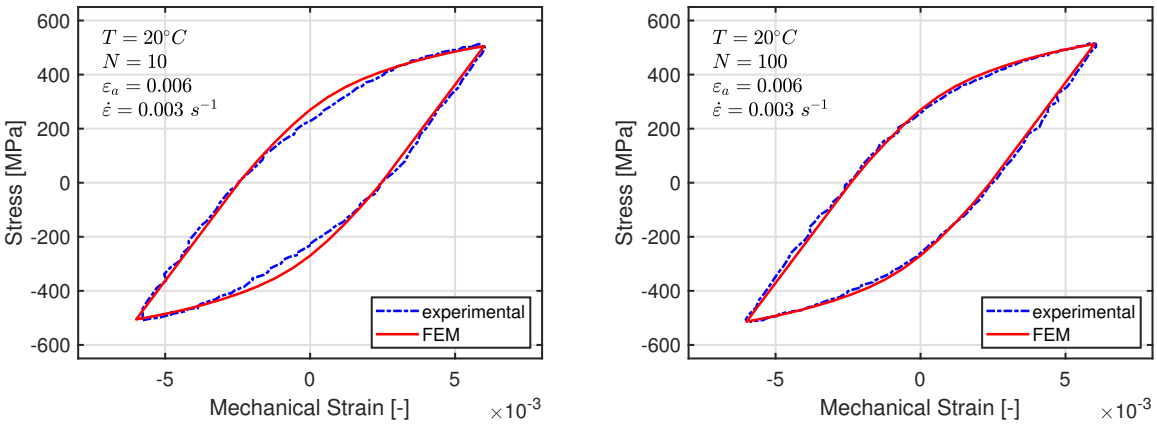

Figure 6.7: LCF response at 20°C for strain rate 0.003 s^{-1}, hysteresis loop for the 10th cycle (a) and for the 100th cycle (b).

hysteresis loops obtained at 650°C for mechanical strain rate $\dot{\varepsilon} = 0.003\ s^{-1}$ are presented in Figs. 6.10a and 6.10b for the 10th and 200th loading cycle, respectively. Good correlation was achieved between the predicted results and the observed results at 20°C, 400°C, 550°C and 650°C for the high mechanical strain rate, $\dot{\varepsilon} = 0.003\ s^{-1}$. However, small differences between the predicted hysteresis loop shapes and the observed hysteresis loop shapes can be seen for the 10th cycle at 20°C.

The simulated and observed cyclic evolution of the maximum stress during the LCF tests without hold time is presented in Figs. 6.11a, 6.11b, 6.11c and 6.11d for temperatures of 20°C, 400°C, 550°C and 650°C, respectively [A.3]. Isotropic hardening can be observed at 20°C and at 400°C, whereas isotropic softening is characteristic at 550°C and at 650°C [A.1, A.2, A.3, A.9]. It can be noted that cyclic hardening of the specimens is followed by failure of the specimen. The onset of failure corresponds to the cyclic damage evolution. The constitutive material model used here does not take into account the effect of damage.

The hysteresis loops for the LCF tests with hold time in tension [A.3] are presented in Figs. 6.12a, 6.13a and 6.14a for 400°C, 550°C and 650°C, respectively. The stress relaxation during the hold period is presented in Figs. 6.12b, 6.13b and 6.14b for 400°C, 550°C and 650°C, respectively. It can be observed that the relaxed part of the stress becomes more significant with increasing temperature [A.1]. Reasonable correlation was achieved between the predicted results and the observed results for the LCF tests with the hold time. However, some differences can be observed for the peak stress values and in the shape of the hysteresis loops.

The LCF response at 400°C [A.3] for mechanical strain rate 0.00001 s^{-1} is presented in Fig. 6.15. The LCF results at 550°C for mechanical strain rates 0.00001 s^{-1} and 0.0001 s^{-1} are presented in Figs. 6.16a and 6.16b, respectively. Finally, the results at 650°C for mechanical strain rates 0.00001 s^{-1} and 0.0003 s^{-1} are showed in Figs. 6.17a and 6.17b. The

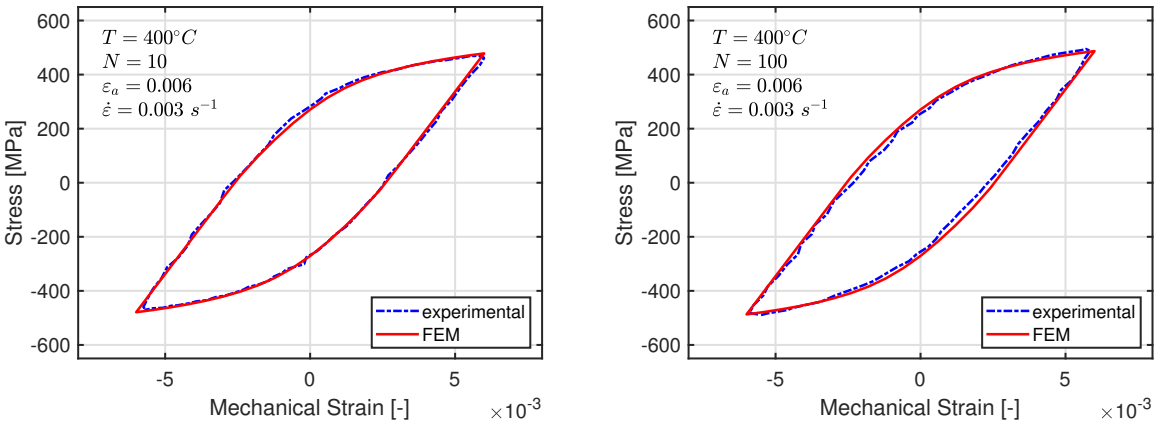

(a) (b)

Figure 6.8: LCF response at 400°C for strain rate 0.003 s^{-1}, hysteresis loop for the 10th cycle (a) and for the 100th cycle (b).

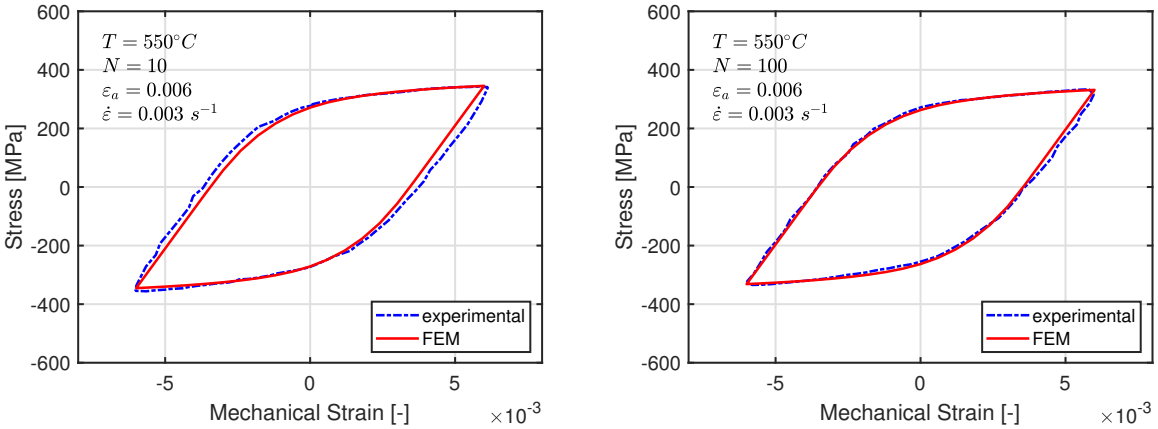

(a) (b)

Figure 6.9: LCF response at 550°C for strain rate 0.003 s^{-1}, hysteresis loop for the 10th cycle (a) and for the 100th cycle (b).

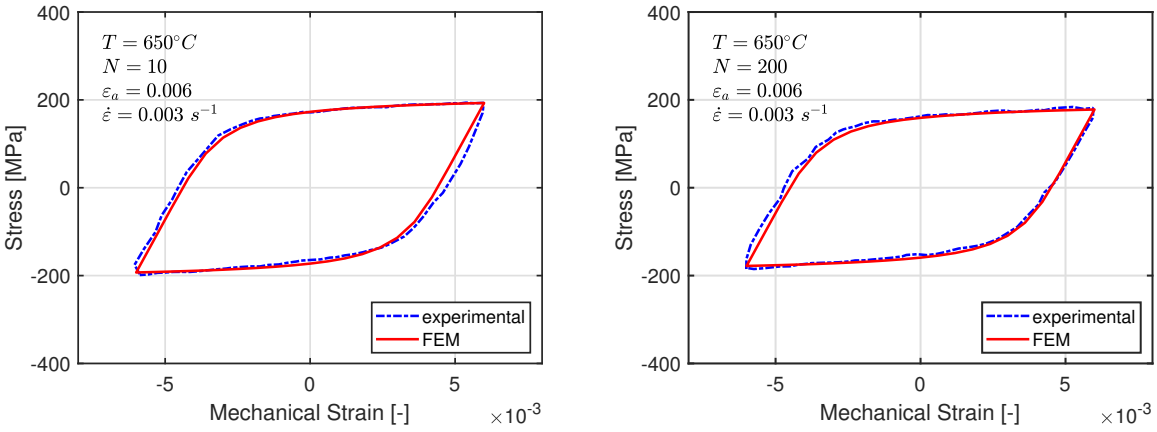

Figure 6.10: LCF response at 650°C for strain rate 0.003 s^{-1}, hysteresis loop for the 10th cycle (a) and for the 200th cycle (b).

used hyperbolic sine flow rule results in good prediction of viscous stress, which can be observed in the form of relaxation or strain-rate sensitivity [A.3, A.5]. However, small differences in hysteresis loop shapes can be observed for lowest studied strain rate 0.00001 s^{-1}.

Finally, the unified viscoplastic constitutive material model, which was calibrated from the isothermal LCF tests, is used to simulate the mechanical response of the SiMo 4.06 under out-of-phase thermo-mechanical fatigue (OP-TMF). This test was performed as fully constrained [A.1, A.9, A.14, A.15] between 100°C and 650°C. This means that the mechanical strain, ε_m, was in the opposite phase to the thermal strain, ε_{th}, and the mechanical strain range was equal to the thermal strain range, $\Delta\varepsilon_m = -\Delta\varepsilon_{th}$. The temperature and the mechanical strain loading history are presented in Fig. 6.18a. It can be observed that the loading cycle lasted over 200 s and the strain rate was variable during the loading cycle. The temperature dependent secant thermal expansion coefficient for SiMo 4.06 was determined from thermal strain measurement obtained from four successive thermal cycles, Fig. 6.18a, which were attained with zero load force. This preceded OP-TMF test. The observed hysteresis loop and the simulated hysteresis loop for the 30th cycle are presented in Fig. 6.18b for the OP-TMF test [A.1, A.9, A.14, A.15]. The compression part of the hysteresis loop is well predicted using the calibrated unified viscoplastic model. Small differences between simulation and experiment can be observed in the loading part of the hysteresis loop. The differences correspond to the temperatures around 400°C, and a study of the LCF tests at a lower amplitude of mechanical strain will be probably required.

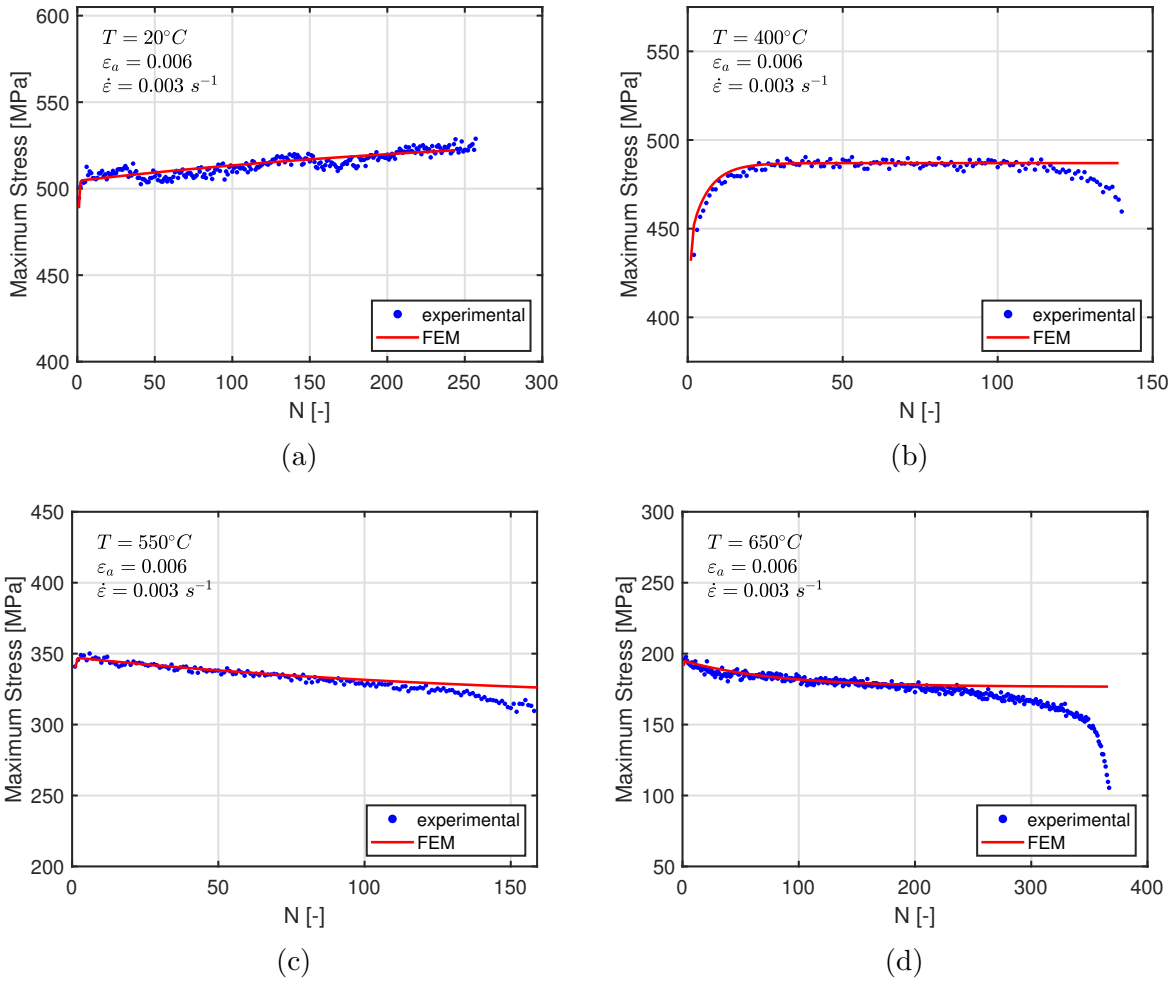

Figure 6.11: Cyclic evolution of the maximum stress during triangular LCF tests at 20°C (a), 400°C (b), 550°C (c) and 650°C (d) for strain rate 0.003 s^{-1}.

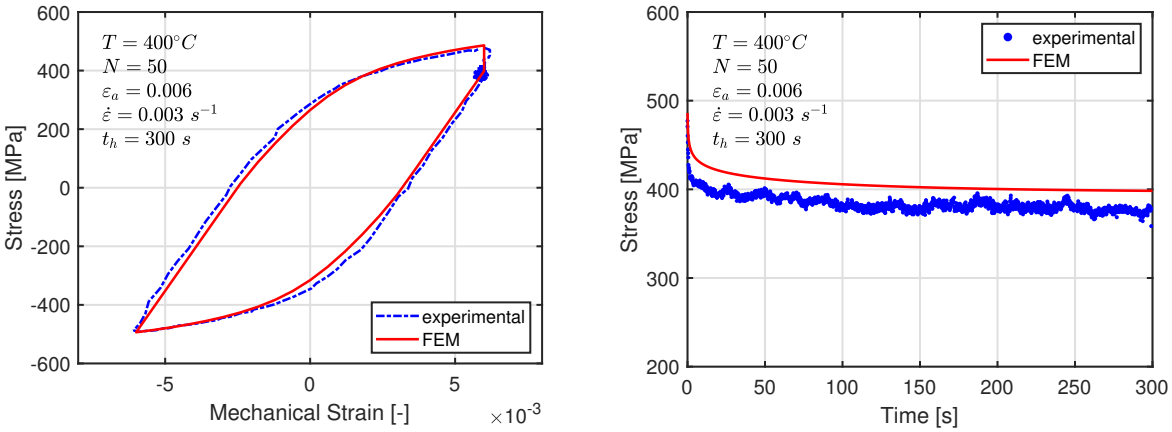

(a) (b)

Figure 6.12: LCF with 300 s hold time at 400°C, hysteresis loop for the 50th cycle (a) and corresponding stress relaxation during the hold time (b).

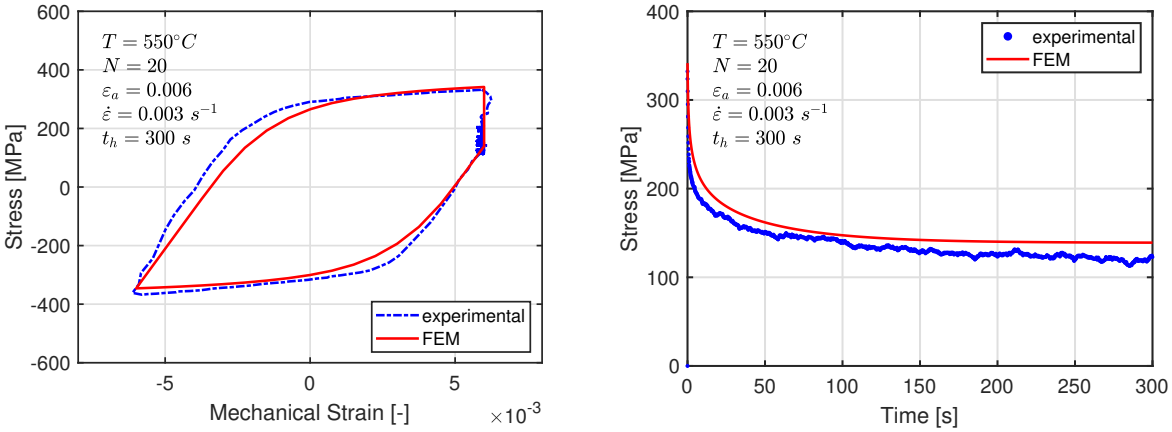

(a) (b)

Figure 6.13: LCF with 300 s hold time at 550°C, hysteresis loop for the 20th cycle (a) and the corresponding stress relaxation during the hold time (b).

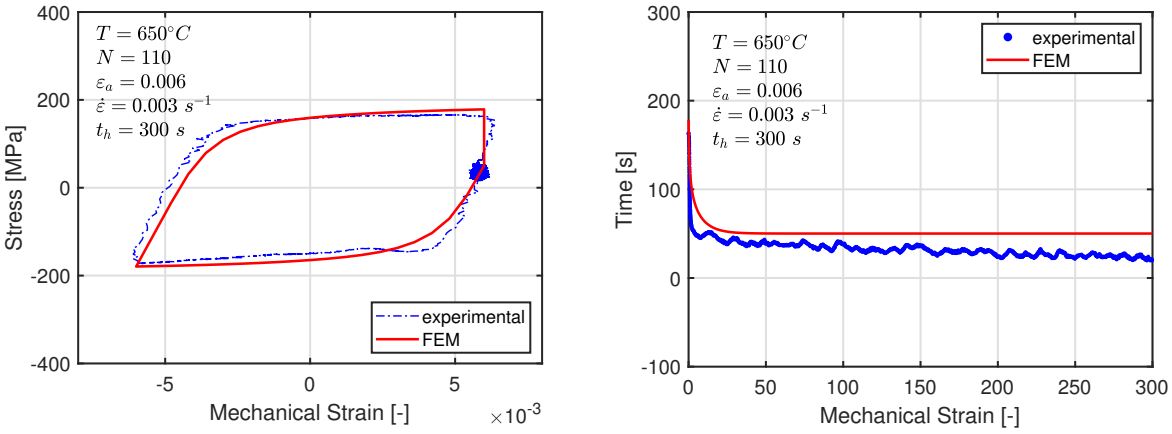

(a) (b)

Figure 6.14: LCF with 300 s hold time at 650°C, hysteresis loop for the 110th cycle (a) and the corresponding stress relaxation during the hold time (b).

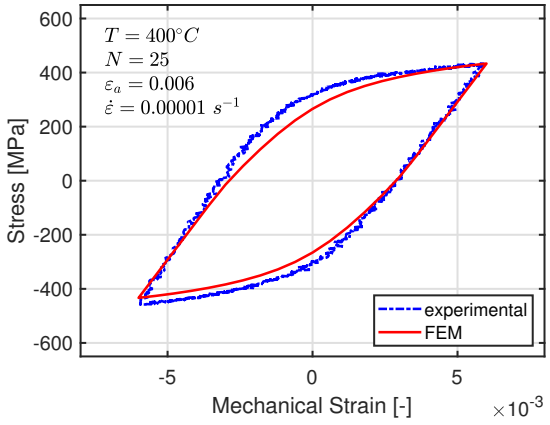

Figure 6.15: LCF response at 400°C, hysteresis loop at 25th cycle for strain rate 0.00001 s^{-1}.

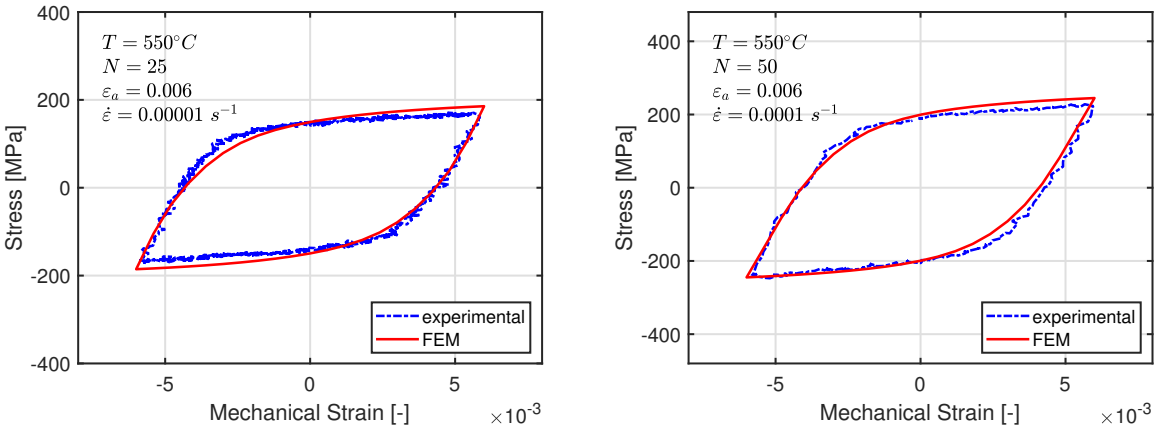

(a) (b)

Figure 6.16: LCF response at 550°C, hysteresis loop for the 25th cycle for strain rate 0.00001 s^{-1} (a) and the hysteresis loop for the 50th cycle for strain rate 0.0001 s^{-1} (b).

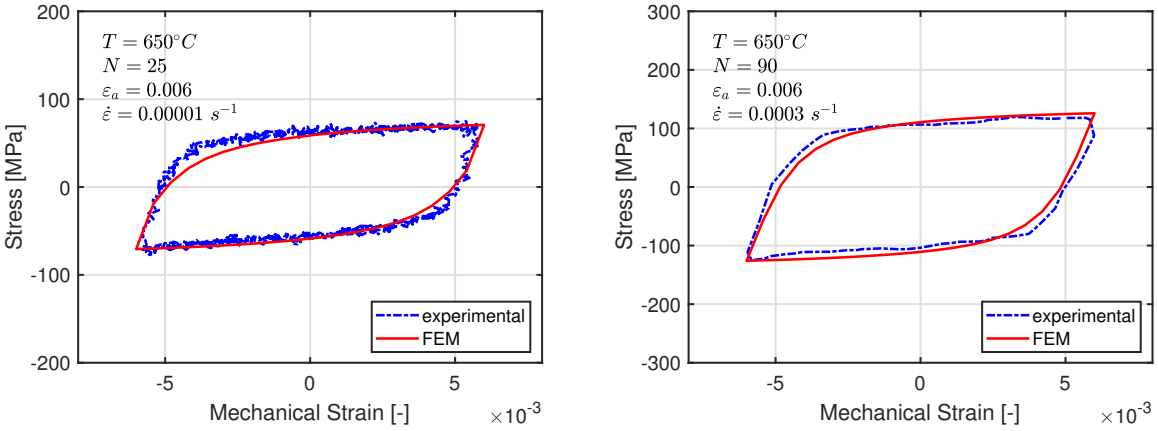

(a) (b)

Figure 6.17: LCF response at 650°C, hysteresis loop for the 25th cycle for strain rate 0.00001 s^{-1} (a) and the hysteresis loop for the 90th cycle for strain rate 0.0003 s^{-1} (b).

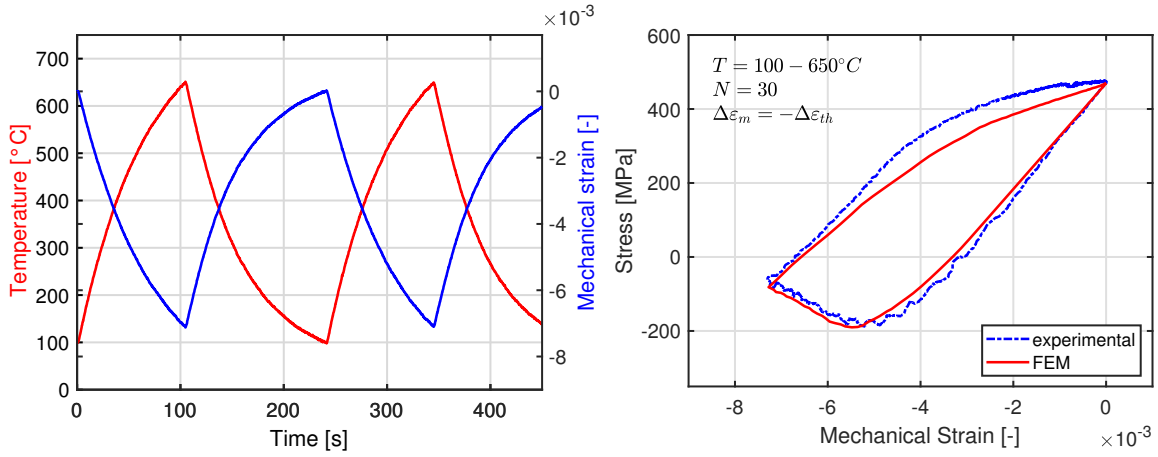

(a) (b)

Figure 6.18: OP-TMF response between 100°C and 650°C, temperature and mechanical strain history during the OP-TMF test (a) and the hysteresis loop for the 30th cycle (b).

6.4.2 Validation of consistent tangent stiffness

A notched cylindrical specimen is chosen as a numerical example in order to study the performance and the speed of convergence of the derived tangent stiffness in Abaqus commercial finite element software [A.3, A.5], under the assumption of small displacements. A finite element model of a notched specimen is presented in Fig. 6.19. The finite element model consists of 241 axisymmetric quadratic quadrilateral elements. The symmetry boundary condition is applied to the bottom of the specimen, and the displacement boundary condition, $u_y = 0.05$, is applied on the top. The temperature of the specimen is constant over the loading step and is set equal to 450°C. The total length of the loading step is 25 s, which corresponds to an averaged strain rate of 0.0004 s^{-1}.

First, the speed of convergence of the consistent tangent stiffness (CTS) is compared with the computations with elastic stiffness. The convergence criterion for the largest residual force of the global Newton method is set to the default value in Abaqus, which is equal to $5.10^{-3}N$. The results of this study are presented in Tab.6.4, where NI is the total number of increments and NEI is the total number of equilibrium iterations. The consistent tangent stiffness needed only one increment to complete the step. If we compare the total number of equilibrium iterations, we can observe a much lower numerical cost for consistent tangent stiffness than for elastic stiffness.

Next, the convergence criterion for the largest residual force of the global Newton method is set to $5.10^{-7}N$ in order to study the speed of convergence for consistent tangent stiffness. The results in terms of the largest residual force for each iteration of the selected increment, are presented in Tab.6.5. The values of the largest residual force, presented in Tab.6.5, show quadratic convergence of the global Newton method [A.3, A.5].

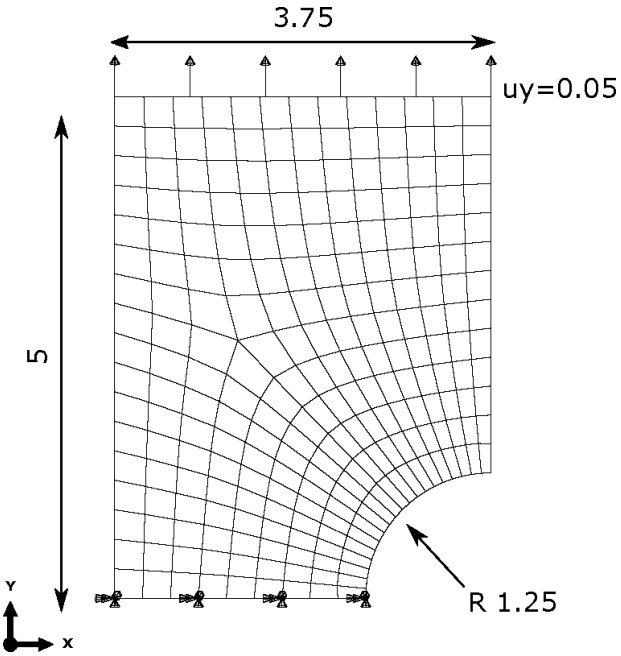

Figure 6.19: Finite element model of a notched cylindrical specimen.

Table 6.4: Number of increments and total equilibrium iterations.

	NI	NEI
CTS	1	9
Elastic stiffness	16	77

Table 6.5: Values of the largest residual force in equilibrium iterations for the selected increment.

Equilibrium iteration	1	2	3	4
Largest residual force [N]	2.88	1.08E-02	2.31E-05	5.30E-08

6.5 Discussion and conclusion

The unified material model that is used can be calibrated only from the isothermal LCF data in the selected temperature range attained as triangular and for LCF loading cycles with hold time [A.3, A.5]. The selected temperature range should fully cover the temperature range during the service life of the investigated components. The choice of the hyperbolic sine flow rule leads to good predictions of the mechanical response for various mechanical strain rates as was shown for LCF tests obtained at different constant mechanical strain rates. The constitutive model was validated for the OP-TMF cycle, and the mechanical strain rate was variable during this test. The constitutive model can be further validated for static loading tests, i.e. for a static creep rupture test and for a tensile test, for LCF tests with longer dwell periods and for TMF loading with a different phase between the mechanical strain and the thermal strain, i.e. temperature.

A unified viscoplastic model with the hyperbolic sine flow rule has been implemented in Abaqus finite element software [A.3, A.5]. The consistent tangent stiffness was analytically derived in order to preserve the quadratic convergence of the global Newton method, which is essential for solving large engineering problems [A.3, A.5]. The material model parameters were determined from triangular isothermal LCF tests with and without the hold time, which were obtained for temperatures between 20°C and 650°C for SiMo 4.06 cast iron. The values of kinematic hardening parameter were calibrated to follow monotonic downward trend on temperature described mathematically as Boltzmann function. A systematic calibration of the other material model parameters as mathematical functions of temperature is possible topic for future research.

The material model was used to simulate the cyclic mechanical behaviour at the investigated temperature for various mechanical strain rates in the LCF tests and for out-of-phase TMF loading. A reasonable correlation was achieved between the predicted results and the observed results [A.3, A.5].

Chapter 7

A novel fatigue criterion

This chapter is divided into three sections. First, initial results and underlying facts about dissipated energy per cycle [A.1] are presented for the investigated material in Section 7.1. Consequently, a novel fatigue criterion [A.1] is proposed in Section 7.2 on the basis of findings in previous section. Finally, the results obtained in this chapter are discussed in Section 7.3.

7.1 Investigation of dissipated energy per cycle

The dissipated energy per cycle, w, versus the number of cycles to failure, N_f, is presented for cylindrical specimens under LCF loading conditions in Fig. 7.1 [A.1], where R^2LCF denotes the coefficient of determination and is computed from the experimental LCF data obtained for all tested temperatures and the regression line, Tab. 5.2. The regression results, described here by the coefficient of determination $R^2LCF = 0.875$, confirm that temperature has no major influence on the dependency between the dissipated energy per cycle and the number of cycles to failure for the investigated material [26, 29]. OP-TMF data are added in Fig. 7.1 to illustrate the shorter lifetime of these specimens in comparison with the LCF results. It should be noted that this difference is also caused by the influence of the positive mean stress in the case of OP-TMF, and for the LCF tests, the mean stress is close to zero. In addition, the OP-TMF lifetime is significantly shorter than the the lifetime predicted by the isothermal LCF tests for the same strain range and for the minimum or the maximum temperature of the OP-TMF cycle [A.1, A.9]. It should be noted that the lifetimes of LCF with a hold time and without a hold time are comparable in terms of dissipated energy versus lifetime, but more tests are required to verify this assumption.

If we compare the strain ranges and the observed cycles to failure for LCF at different temperatures, we can observe that the specimens showed monotonically increasing durability in high strain ranges with increasing temperature. A decrease in lifetime was observed with increasing temperatures for low strain range tests [A.1, A.2, A.9]. In terms of the dissipated energy per cycle versus the number of cycles to failure, no significant difference is observed [A.1]. For the hysteresis loops, one can observe that the yield stress decreases with increasing temperature, and also the hysteresis loops become more flatter with in-

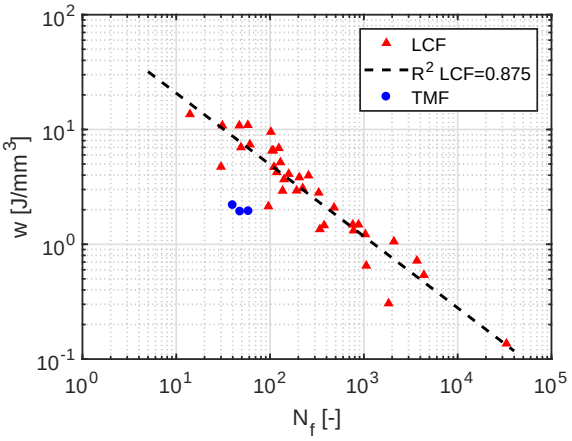

Figure 7.1: Dissipated hysteresis energy versus the number of cycles to failure for LCF and TMF tests.

creasing temperature. At lower temperatures, greater plastic hardening is observed in the corresponding hysteresis loop at mid-life, Fig. 5.8, whereas almost perfect plasticity can be observed at 750°C, Fig. 5.10. This is related to the dissipated energy per cycle. If we compare the LCF data at 20°C, the dissipated energy per cycle for the lowest strain range $\Delta\varepsilon_m = 0.0051$ is equal to 0.14 $J.mm^{-3}$, and for the highest strain range $\Delta\varepsilon_m = 0.0244$ it is 13.57 $J.mm^{-3}$. For the LCF data at 750°C, the dissipated energy per cycle for the lowest strain range $\Delta\varepsilon_m = 0.0047$ is 0.31 $J.mm^{-3}$, for the highest strain range $\Delta\varepsilon_m = 0.0239$ equals to 2.92 $J.mm^{-3}$, the results are less deviated from the mean value than the results obtained at room temperature. These results also justify the assumption that temperature has no major influence on the dependency between the dissipated energy per cycle and the number of cycles to failure for SiMo [A.1]. Therefore, the LCF data, in terms of the dissipated energy and the lifetime, do not additionally have to be splitted by temperature [A.1].

Moreover, the LCF test results presented in Tab. 5.2 also show that for the same strain ranges and temperatures, a difference in the dissipated energy per cycle is observed, which is caused by the differences in mechanical response of a single specimen, as each specimen was cast separately and then machined. However, the dependency between the dissipated energy per cycle and the number of cycles to failure remained same [A.1].

7.2 A novel fatigue criterion

Oxidation, fatigue and creep are often referred to as the main TMF damage mechanisms [64, 65, 74]. Various fatigue criteria for LCF and for TMF life assessment can be found in the literature. Positive or negative mean stress of a loading cycle with variable temperature in out-of-phase or in-phase TMF tests is caused by material parameters that change with temperature. Changes of temperature during a loading cycle and the mean stress effect

can be taken into account in various ways. Energy-based fatigue criteria work well with unified viscoplastic models, e.g. [22], which are characterized by one inelastic strain, i.e. viscoplastic strain. By contrast, the damage operator approach [61–63] separates the total mechanical strain into a viscous part and an elastic-plastic part. The creep and the fatigue damage are then calculated separately. The oxidation effect is usually taken into account indirectly.

Moreover, several energy-based fatigue criteria from literature were tested for experimental results presented here. However, for example, modified energy based criterion modified by hydrostatic pressure [3, 4], which requires all material parameters to be calibrated from isothermal LCF data, has shown poor correlation for the material investigated here, even for isothermal LCF results. These results stimulated development of a new criterion for predicting LCF and TMF lifetime.

In this work, a energy-based criterion is proposed for predicting LCF and TMF [A.1]. The LCF results presented here show that temperature has no major influence on the dependency between the dissipated energy per cycle and the number of cycles to failure for SiMo, Fig. 7.1. Therefore, no temperature term is included in the proposed criterion [A.1]. The oxidation effect is taken into account indirectly in the following dissipated energy criterion, as the material tests were performed under ambient conditions [A.1]. The mean stress effect is taken into account by means of the modified dissipated energy per cycle, $\widetilde{w}$, as follows:

$$\widetilde{w} = AN_f^B, \tag{7.1}$$

where A and B are the material parameters obtained by the least squares method from the LCF test data from all temperatures that were performed on the cylindrical specimens, Tab. 5.2, and correspond to the regression line in Fig. 7.1. The effect of mean stress on lifetime for the OP-TMF test is considerable for SiMo. To improve the predictions, we suggested the modified dissipated energy per cycle $\widetilde{w}$, including the mean stress term, defined as follows:

$$\widetilde{w} = w + \alpha(-1 - R_\sigma^{-1}), \tag{7.2}$$

where α is an additional material parameter, which is obtained by the least squares method from the results of the TMF tests, and w is the cycle dissipated energy (Eq. 5.1):

$$w = \int_{cycle} \boldsymbol{\sigma} : \dot{\boldsymbol{\varepsilon}}_m dt. \tag{7.3}$$

The stress ratio R_σ is defined as:

$$R_\sigma = \frac{\sigma_{min}}{\sigma_{max}}, \tag{7.4}$$

where σ_{min} and σ_{max} are the minimal and the maximal principal stress over the loading cycle, respectively.

For the LCF tests, the mean stress is close to zero, i.e. $R_\sigma = -1$. Therefore, the mean stress term in Eq. 7.2 vanishes, and the modified dissipated energy per cycle is equal

to the dissipated energy per cycle for the LCF tests. The stress ratio was approximately $R_\sigma = -0.4$ in the OP-TMF tests. The mean stress term for OP-TMF increases the modified dissipated energy per cycle. Therefore, the modified dissipated energy per cycle criterion predicts a shorter lifetime in the OP-TMF tests, assuming positive parameter α. It should be noted that the modified dissipated energy per cycle criterion presented here predicts a longer lifetime for cases, where negative mean stress is present, as in the case of IP-TMF.

The model parameters and the corresponding coefficient of determination are presented in Tab. 7.1 [A.1], where results are also presented for a criterion with no additional terms corresponding to the classical dissipated energy per cycle criterion, i.e. $\widetilde{w} = w$, this criterion doesn't render the role of the mean stress. If we compare the obtained R^2, one can note that the modified dissipated energy per cycle fits the OP-TMF experimental results better. The predicted number of cycles to failure versus the observed number of cycles to failure is plotted in Fig. 7.3 [A.1] for the modified dissipated energy per cycle criterion, and in Fig. 7.2 for the dissipated energy per cycle criterion [A.1]. The dashed lines denote the prediction interval with 95% confidence level. The 95% prediction interval almost coincides with a two times band for the proposed model. This indicates a reliable fatigue predictions. The OP-TMF tests on cylindrical specimens showed a good correlation between prediction and experiment. It can be observed that R^2 obtained for TMF and LCF data for the modified dissipated energy criterion is even higher than R^2LCF, which is computed only from the LCF data, Fig. 7.1 [A.1]. This is due to the introduction of additional variable R_σ and the calibrated material-dependent parameter α.

Table 7.1: Damage model parameters obtained by regression from the LCF and the TMF test data.

Criterion	A	B	α	R^2
w	87.096	-0.624	-	0.740
$\widetilde{w}$	87.096	-0.624	4.239	0.882

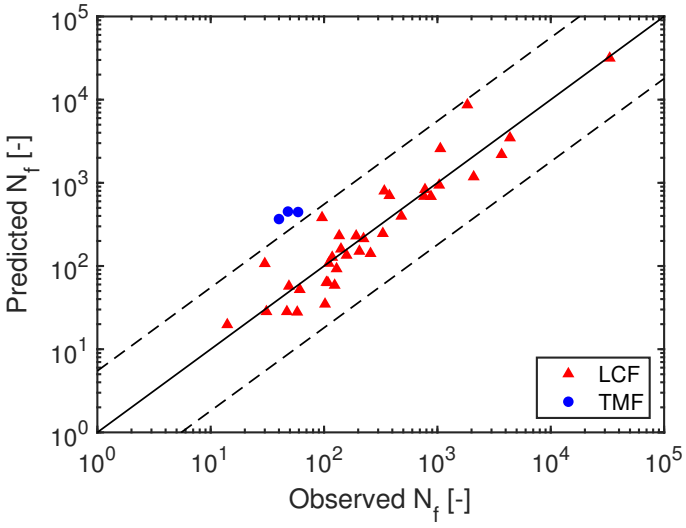

Figure 7.2: Dissipated energy per cycle criterion. Observed and predicted lifetime for specimens under TMF and LCF loading conditions.

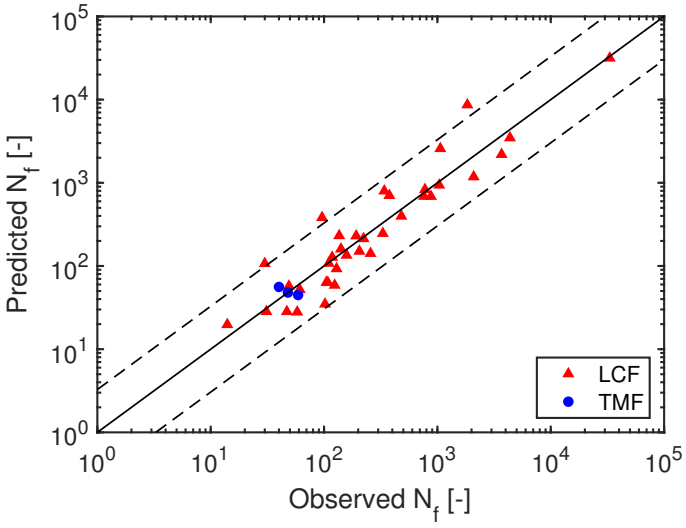

Figure 7.3: Modified dissipated energy per cycle criterion. Observed and predicted lifetime for specimens under TMF and LCF loading conditions.

7.3 Discussion and conclusion

One of the key assumptions here is that lifetime prediction is based on data from the stabilized state. If stabilization does not occur, e.g. in the case of a very short lifetime, the lifetime prediction may be inaccurate. Moreover, the time factor is not explicitly taken into account in the proposed criterion. The modified dissipated energy per cycle criterion is based on the coupled plasticity and creep formulation, as they occur simultaneously. Therefore, creep and fatigue damage are not calculated separately and the time factor is implicitly taken into account as the energy is also dissipated during the creep periods. In the case of dwell period, the overall shape of the hysteresis loop is changed, and the dissipated energy per cycle is different from the case of a test without a dwell period [A.1, A.3].

The LCF tests showed that the dependency between the dissipated energy per cycle and the number of cycles to failure does not depend on the temperature at which the test is performed [A.1]. The proposed fatigue criterion [A.1] based on the dissipated hysteresis energy takes into account the effect of the mean stress of the loading cycle, which is caused by changes in temperature during the loading cycle. The oxidation effect was taken into account indirectly, because the tests were performed under ambient conditions. A reasonable correlation between the observed lifetime and the predicted lifetime was achieved for the LCF and TMF tests [A.1]. Simplicity and robustness is characteristic for the proposed criterion. The criterion can be implemented as a post-processing program for finite-element software [A.6, A.17, A.18]. The proposed criterion can easily be modified, for example, by replacing linear term by a different function, or by replacing round brackets with Macaulay brackets, if no positive effect of negative mean stress on lifetime is observed. However, there is a need for TMF tests with various phases between the mechanical strain and the thermal strain, primarily IP-TMF tests.

Chapter 8

Outcomes

8.1 Theoretical outcomes

High temperature data LCF and TMF data are mostly not published in its raw form and therefore may not be re-used by other researchers for their work. The presented experimental data for SiMo 4.06 in this work have been published in its raw form in [A.1, A.3]. Specifically, the stress-strain hysteresis loops obtained at different temperatures and for the different mechanical strain rates can be used together with the cyclic relaxation test data for a calibration of material model. This can be used in order to study material models without the need to obtain own original experimental data. Furthermore, the published experimental results represented by amplitude of the strain and number of cycles to a failure for five different temperatures together with the OP-TMF test results can be used for fatigue analysis by other authors.

The implementation of a unified viscoplastic model in the framework of finite element method and consistent tangent stiffness was published in [A.3]. This will allow another researchers to speed up the development of their own modifications of material models, especially the derivation of consistent tangent stiffness, which is usually the hardest part of the work and its needed in order to solve large scale problems with acceptable numerical costs. Furthermore, the used hyperbolic sine flow rule can be used for wide range of strain rates more reliably in comparison with widely used power-law flow rule in the framework of unified viscoplastic material models.

The proposed energy based fatigue criterion can be used for fatigue predictions of metal materials under LCF and TMF loading conditions. The criterion can be further studied and modified if needed. The proposed criterion develops the interesting concept of dissipated hysteresis energy that is alternative to complicated phenomenological lifetime prediction models. The energy based fatigue criteria do not partition strain into plastic and creep part, the criteria are suitable to be used for the unified viscoplastic material models.

8.2 Practical outcomes

The introduced newly in-house designed test can be used for performing LCF and TMF uniaxial tests on specimens. The obtained results can be used in order to calibrate most commonly used engineering material model [A.2, A.10] that are usually implemented in commercial finite element software by default.

The selected unified viscoplastic material model is implemented as a user material subroutine for Abaqus commercial finite element software, so that it can be used for solving practical problems. The material model can be used for simulation of mechanical response under the complex anisothermal loading conditions. The formulated consistent tangent stiffness is a key point for solving large-scale engineering problems.

The proposed energy based fatigue criterion can be used for fatigue analysis with the advantage of low numerical costs in comparison with the methods assuming critical plane approach. The calibration of the criterion does not require expensive test stands, such as those with climatic chamber. The presented results may be used for damage assessment method of complex engineering components that are subjected to high temperature LCF and TMF loading conditions.

Chapter 9

Conclusions and future work

9.1 Conclusions

The aims of the thesis were accomplished with the following comments:

1. A novel energy based fatigue criterion was proposed in order to predict LCF/TMF lifetime for specimens and for complex engineering structures. A reasonable correlation was achieved between the observed results and the predicted results. The proposed fatigue criterion was published in [A.1]. The development of the criterion was published in [A.11] and its possible implementation in commercial finite-element software packages was discussed in [A.6].

2. The proposed control and control algorithms for the new in-house designed test stand enable strain-controlled high temperature uniaxial LCF and TMF tests performed on specimens. The results were given in Chapter 5 and published in [A.1, A.9, A.12].

3. Large amount of new experimental data was generated for SiMo 4.06. Obtained data for temperatures between 20°C and 750°C can be used for calibration of constitutive material models and for fatigue analysis. The experimental results were presented in Chapter 5 and used in Chapters 6 and 7, and were published in [A.1, A.9, A.13, A.14, A.15]. Selected experimental data were also published together with computations in [A.2]-[A.12].

4. A unified viscoplastic material model was implemented as user material subroutine for Abaqus commercial finite element software. The consistent tangent stiffness was derived on the basis of numerical integration scheme that was used for implicit integration of constitutive model equations. The consistent tangent stiffness was verified on the numerical example. The results were described in Chapter 6. The implementation of material model and its calibration were published in [A.3, A.5].

5. The temperature dependent unified viscoplastic material model was calibrated from the obtained experimental data. The non-linear kinematic hardening model param-

eters were newly calibrated systematically with temperature, mathematically represented as a Boltzmann function. A reasonable correlation was achieved between the observed results and the predicted results. The calibration of the viscoplastic model was published in [A.3, A.5]. The calibration of temperature dependent kinematic hardening parameters was also included in [A.2, A.4, A.7, A.8, A.10]. The systematically calibrated temperature dependent kinematic hardening parameters were used for a engineering failure analysis of turbine housing in [A.2].

9.2 Future work and outlook

In the framework of SiMo 4.06, possible topics for future research are mechanical behaviour and lifetime for IP-TMF tests, strain range dependency behaviour and mechanical behaviour for long dwell time during LCF tests. IP-TMF loading will probably lead to longer lifetimes in comparison with OP-TMF due to compressive mean stress during the IP-TMF loading, however, verification of the fatigue proposed criterion should be done in terms of IP-TMF tests. Strain range dependency, if occurs, should be study in order to validate isotropic and kinematic hardening equations. This may lead to a need of a memory surface model. Next, longer dwell times during the LCF or TMF may introduced changes in mechanical behaviour, such as additional softening. Moreover, the plasticity-creep interaction in terms of lifetime and constitutive mechanical behaviour is another possible subject of future research. The possible need of modifications may arise, for the used unified material model and for the proposed fatigue criterion.

Furthermore, most of the published research in the framework of high temperature LCF and TMF is carried out on uniaxial material tests. The mechanical behaviour of metal materials subject to proportional, and in particular non-proportional, multiaxial thermo-mechanical loading is generally a subject of future interest and research. This covers validation of commonly used constitutive material models and as well as validation of commonly used damage models. However, this will require multiaxial thermo-mechanical fatigue test stands, which are very expensive in general.

References

[1] *ABAQUS/Standard User's Manual, Version 6.14*. Dassault Systèmes, 2014.

[2] Ahmed, R., Barrett, P. R., and Hassan, T. Unified viscoplasticity modeling for isothermal low-cycle fatigue and fatigue-creep stress–strain responses of haynes 230. *International Journal of Solids and Structures 88* (2016), 131–145.

[3] Amiable, S., Chapuliot, S., Constantinescu, A., and Fissolo, A. A computational lifetime prediction of a thermal shock experiment. part i: thermomechanical modelling and lifetime prediction. *Fatigue & Fracture of Engineering Materials & Structures 29*, 3 (2006), 175–182.

[4] Amiable, S., Chapuliot, S., Constantinescu, A., and Fissolo, A. A computational lifetime prediction of a thermal shock experiment. part ii: discussion on difference fatigue criteria. *Fatigue & Fracture of Engineering Materials & Structures 29*, 3 (2006), 219–227.

[5] Armstrong, P. J., and Frederick, C. *A mathematical representation of the multiaxial Bauschinger effect*, vol. 731. Central Electricity Generating Board [and] Berkeley Nuclear Laboratories, Research & Development Department Berkeley, 1966.

[6] Barrett, R., Farragher, T., Hyde, C. J., O'Dowd, N., O'Donoghue, P., and Leen, S. B. A unified viscoplastic model for high temperature low cycle fatigue of service-aged p91 steel. *Journal of Pressure Vessel Technology 136*, 2 (2014), 021402.

[7] Barrett, R. A., O'Donoghue, P., and Leen, S. B. An improved unified viscoplastic constitutive model for strain-rate sensitivity in high temperature fatigue. *International Journal of Fatigue 48* (2013), 192–204.

[8] Beck, T., Pitz, G., Lang, K.-H., and Löhe, D. Thermal-mechanical and isothermal fatigue of in 792 cc. *Materials Science and Engineering: A 234* (1997), 719–722.

[9] Beck, T., and Rau, K. Temperature measurement and control methods in tmf testing–a comparison and evaluation. *International journal of fatigue 30*, 2 (2008), 226–233.

[10] Bodner, S. Review of unified elastic-viscoplastic theory. in unified constitutive equations for plastic deformation and creep of engineering alloys. *Elsevier Applied Science* (1987).

[11] Bodner, S., and Partom, Y. Constitutive equations for elastic-viscoplastic strain-hardening materials. *Journal of Applied Mechanics 42*, 2 (1975), 385–389.

[12] Brokate, M., Dressler, K., and Krejci, P. Rainflow counting and energy dissipation for hysteresis models in elastoplasticity. *European journal of mechanics A/Solids 15*, 4 (1996), 705–737.

[13] Brokate, M., and Sprekels, J. *Hysteresis and phase transitions*, vol. 121. Springer Science & Business Media, 2012.

[14] Brookes, S.-P., Kühn, H.-J., Skrotzki, B., Klingelhöffer, H., Sievert, R., Pfetzing, J., Peter, D., and Eggeler, G. Axial–torsional thermomechanical fatigue of a near-γ tial-alloy. *Materials Science and Engineering: A 527*, 16-17 (2010), 3829–3839.

[15] Byrd, R. H., Gilbert, J. C., and Nocedal, J. A trust region method based on interior point techniques for nonlinear programming. *Mathematical Programming 89*, 1 (2000), 149–185.

[16] Byrd, R. H., Hribar, M. E., and Nocedal, J. An interior point algorithm for large-scale nonlinear programming. *SIAM Journal on Optimization 9*, 4 (1999), 877–900.

[17] Cailletaud, G., and Sai, K. Study of plastic/viscoplastic models with various inelastic mechanisms. *International Journal of Plasticity 11*, 8 (1995), 991–1005.

[18] Cernocky, E., and Krempl, E. A theory of thermoviscoplasticity based on infinitesimal total strain. *International Journal of Solids and Structures 16*, 8 (1980), 723–741.

[19] Chaboche, J., and Nouailhas, D. A unified constitutive model for cyclic viscoplasticity and its applications to various stainless steels. *Journal of Engineering Materials and Technology 111*, 4 (1989), 424–430.

[20] Chaboche, J., Van, K. D., and Cordier, G. Modelization of the strain memory effect on the cyclic hardening of 316 stainless steel.

[21] Chaboche, J.-L. Time-independent constitutive theories for cyclic plasticity. *International Journal of plasticity 2*, 2 (1986), 149–188.

[22] Chaboche, J.-L. Constitutive equations for cyclic plasticity and cyclic viscoplasticity. *International journal of plasticity 5*, 3 (1989), 247–302.

[23] Chaboche, J.-L. On some modifications of kinematic hardening to improve the description of ratchetting effects. *International journal of plasticity 7*, 7 (1991), 661–678.

[24] Chaboche, J.-L. A review of some plasticity and viscoplasticity constitutive theories. *International journal of plasticity 24*, 10 (2008), 1642–1693.

[25] Chaboche, J.-L., and Gallerneau, F. An overview of the damage approach of durability modelling at elevated temperature. *Fatigue & Fracture of Engineering Materials & Structures 24*, 6 (2001), 405–418.

[26] Charkaluk, E., Bignonnet, A., Constantinescu, A., and Dang Van, K. Fatigue design of structures under thermomechanical loadings. *Fatigue & Fracture of Engineering Materials & Structures 25*, 12 (2002), 1199–1206.

[27] Charkaluk, E., and Constantinescu, A. An energetic approach in thermomechanical fatigue for silicon molybdenum cast iron. *Materials at high temperatures 17*, 3 (2000), 373–380.

[28] Coffin Jr, L. F. A study of the effects of cyclic thermal stresses on a ductile metal. *Transactions of the American Society of Mechanical Engineers, New York 76* (1954), 931–950.

[29] Constantinescu, A., Charkaluk, E., Lederer, G., and Verger, L. A computational approach to thermomechanical fatigue. *International Journal of fatigue 26*, 8 (2004), 805–818.

[30] Contesti, E., and Cailletaud, G. Description of creep-plasticity interaction with non-unified constitutive equations: application to an austenitic stainless steel. *Nuclear engineering and design 116*, 3 (1989), 265–280.

[31] Corum, J., and Blass, J. Rules for design of alloy 617 nuclear components to very high temperatures. Tech. rep., Oak Ridge National Lab., 1991.

[32] Dunne, F., and Petrinic, N. *Introduction to computational plasticity*. Oxford University Press on Demand, 2005.

[33] Feltner, C. E., and Morrow, J. D. Microplastic strain hysteresis energy as a criterion for fatigue fracture. *Journal of Basic Engineering 83*, 1 (1961), 15–22.

[34] Gustafsson, D., Moverare, J., Johansson, S., Simonsson, K., Hörnqvist, M., Månsson, T., and Sjöström, S. Influence of high temperature hold times on the fatigue crack propagation in inconel 718. *International Journal of Fatigue 33*, 11 (2011), 1461–1469.

[35] Guth, S., Petráš, R., Škorík, V., Kruml, T., Man, J., Lang, K.-H., and Polák, J. Influence of dwell times on the thermomechanical fatigue behavior of a directionally solidified ni-base superalloy. *International Journal of Fatigue 80* (2015), 426–433.

[36] Hähner, P., Affeldt, E., Beck, T., Klingelhöffer, H., Loveday, M., and Rinaldi, C. Validated code-of-practice for strain-controlled thermo-mechanical fatigue testing. *Institute for Energy, Petten* (2006).

[37] Hähner, P., Rinaldi, C., Bicego, V., Affeldt, E., Brendel, T., Andersson, H., Beck, T., Klingelhöffer, H., Kühn, H.-J., Köster, A., et al. Research and development into a european code-of-practice for strain-controlled thermo-mechanical fatigue testing. *International Journal of Fatigue 30*, 2 (2008), 372–381.

[38] Halama, R., Fusek, M., and Poruba, Z. Influence of mean stress and stress amplitude on uniaxial and biaxial ratcheting of st52 steel and its prediction by the abdelkarim–ohno model. *International Journal of Fatigue 91* (2016), 313–321.

[39] Halford, G., and Manson, S. Life prediction of thermal-mechanical fatigue using strainrange partitioning. In *Thermal fatigue of materials and components*. ASTM International, 1976.

[40] Hebák, P., Hustopeckỳ, J., and Malá, I. *Vícerozměrné statistické metody 2*. Informatorium, 2005.

[41] Heitmann, H., Vehoff, H., and Neumann, P. Life prediction for random load fatigue based on the growth behavior of microcracks. In *Fracture 84*. Elsevier, 1984, pp. 3599–3606.

[42] Hosseini, E., Holdsworth, S., Kühn, I., and Mazza, E. Temperature dependent representation for chaboche kinematic hardening model. *Materials at High Temperatures 32*, 4 (2015), 404–412.

[43] Jiang, Y., and Sehitoglu, H. Modeling of cyclic ratchetting plasticity, part i: development of constitutive relations. *Journal of Applied Mechanics 63*, 3 (1996), 720–725.

[44] Kadioglu, Y., and Sehitoglu, H. Modeling of thermomechanical fatigue damage in coated alloys. In *Thermomechanical Fatigue Behavior of Materials*. ASTM International, 1993.

[45] Kawai, M., and Ohashi, Y. Couple effect between creep and plasticity of type 316 stainless steel at elevated temperature. Tech. rep., Los Alamos National Lab., NM (USA); Nagoya Univ.(Japan); Aichi Inst. of Tech ..., 1987.

[46] Kichenin, J. *Comportement Thermomecanique du Polyethylene—Application aux Structures Gazieres*. PhD thesis, Ecole Polytechnique, Palaiseau, France, 1995.

[47] Kullig, E., and Wippler, S. Numerical integration and fem-implementation of a viscoplastic chaboche-model with static recovery. *Computational Mechanics 38*, 6 (2006), 1–13.

[48] Lemaitre, J., and Chaboche, J.-L. *Mechanics of solid materials*. Cambridge university press, 1994.

[49] Manson, S. S. Behavior of materials under conditions of thermal stress.

[50] Mao, J., Engler-Pinto Jr, C. C., Li, T., Hsieh, J., and Su, X. Effect of constitutive model on thermomechanical fatigue life prediction. *Procedia Engineering 133* (2015), 655–668.

[51] MATLAB. *MATLAB R2018b Documentation*. The MathWorks Inc., Natick, Massachusetts, 2018.

[52] Miller, A. An inelastic constitutive model for monotonic, cyclic, and creep deformation: Part i—equations development and analytical procedures. *Journal of Engineering Materials and Technology 98*, 2 (1976), 97–105.

[53] Minichmayr, R., Riedler, M., Winter, G., Leitner, H., and Eichlseder, W. Thermo-mechanical fatigue life assessment of aluminium components using the damage rate model of sehitoglu. *International Journal of Fatigue 30*, 2 (2008), 298–304.

[54] Moré, J. J., and Sorensen, D. C. Computing a trust region step. *SIAM Journal on Scientific and Statistical Computing 4*, 3 (1983), 553–572.

[55] Moverare, J. J., and Gustafsson, D. Hold-time effect on the thermo-mechanical fatigue crack growth behaviour of inconel 718. *Materials Science and Engineering: A 528*, 29-30 (2011), 8660–8670.

[56] Murakami, S., and Ohno, N. A constitutive equation of creep based on the concept of a creep-hardening surface. *International Journal of Solids and Structures 18*, 7 (1982), 597–609.

[57] Nagesha, A., Kannan, R., Parameswaran, P., Sandhya, R., Rao, K. B. S., and Singh, V. A comparative study of isothermal and thermomechanical fatigue on type 316l (n) austenitic stainless steel. *Materials Science and Engineering: A 527*, 21-22 (2010), 5969–5975.

[58] Nagode, M. Continuous damage parameter calculation under thermo-mechanical random loading. *MethodsX 1* (2014), 81–89.

[59] Nagode, M., and Fajdiga, M. Temperature–stress–strain trajectory modelling during thermo-mechanical fatigue. *Fatigue & Fracture of Engineering Materials & Structures 29*, 3 (2006), 183–189.

[60] Nagode, M., and Fajdiga, M. Coupled elastoplasticity and viscoplasticity under thermomechanical loading. *Fatigue & Fracture of Engineering Materials & Structures 30*, 6 (2007), 510–519.

[61] Nagode, M., Hack, M., and Fajdiga, M. Low cycle thermo-mechanical fatigue: damage operator approach. *Fatigue & Fracture of Engineering Materials & Structures 33*, 3 (2010), 149–160.

[62] Nagode, M., Längler, F., and Hack, M. A time-dependent damage operator approach to thermo-mechanical fatigue of ni-resist d-5s. *International Journal of Fatigue 33*, 5 (2011), 692–699.

[63] Nagode, M., Šeruga, D., Hack, M., and Hansenne, E. Damage operator-based lifetime calculation under thermomechanical fatigue and creep for application on uginox f12t en 1.4512 exhaust downpipes. *Strain 48*, 3 (2012), 198–207.

[64] Neu, R., and Sehitoglu, H. Thermomechanical fatigue, oxidation, and creep: Part i. damage mechanisms. *Metallurgical and Materials Transactions A 20*, 9 (1989), 1755–1767.

[65] Neu, R., and Sehitoglu, H. Thermomechanical fatigue, oxidation, and creep: Part ii. life prediction. *Metallurgical Transactions A 20*, 9 (1989), 1769–1783.

[66] Norman, V., Skoglund, P., Leidermark, D., and Moverare, J. Damage mechanisms in silicon-molybdenum cast irons subjected to thermo-mechanical fatigue. *International Journal of Fatigue 99* (2017), 258–265.

[67] Nouailhas, D., Chaboche, J., Savalle, S., and Cailletaud, G. On the constitutive equations for cyclic plasticity under nonproportional loading. *International Journal of Plasticity 1*, 4 (1985), 317–330.

[68] Nouailhas, D., Policella, H., and Kaczmarek, H. On the description of cyclic hardening under complex loading histories. *ONERA, TP*, 1983 (1983), 6.

[69] Ohno, N., and Wang, J.-D. Kinematic hardening rules with critical state of dynamic recovery, part i: formulation and basic features for ratchetting behavior. *International journal of plasticity 9*, 3 (1993), 375–390.

[70] Ostergren, W. A damage function and associated failure equations for predicting hold time and frequency effects in elevated temperature, low cycle fatigue. *Journal of Testing and Evaluation 4*, 5 (1976), 327–339.

[71] Petráš, R., Škorík, V., and Polák, J. Thermomechanical fatigue and damage mechanisms in sanicro 25 steel. *Materials Science and Engineering: A 650* (2016), 52–62.

[72] Prager, W. Recent developments in the mathematical theory of plasticity. *Journal of applied physics 20*, 3 (1949), 235–241.

[73] Robinson, D. Unified creep-plasticity model for structural metals at high temperature.[lmfbr]. Tech. rep., Oak Ridge National Lab., TN (USA), 1978.

[74] Sehitoglu, H. Thermo-mechanical fatigue life prediction methods. In *Advances in fatigue lifetime predictive techniques*. ASTM International, 1992.

[75] Sehitoglu, H., and Boismier, D. Thermo-mechanical fatigue of mar-m247: Part 2—life prediction. *Journal of Engineering Materials and Technology 112*, 1 (1990), 80–89.

[76] Šeruga, D., Hansenne, E., Haesen, V., and Nagode, M. Durability prediction of en 1.4512 exhaust mufflers under thermomechanical loading. *International Journal of Mechanical Sciences 84* (2014), 199–207.

[77] Simo, J. C., and Hughes, T. J. *Computational inelasticity*, vol. 7. Springer Science & Business Media, 2006.

[78] Simo, J. C., and Taylor, R. L. Consistent tangent operators for rate-independent elastoplasticity. *Computer methods in applied mechanics and engineering 48*, 1 (1985), 101–118.

[79] Skelton, R. Energy criterion for high temperature low cycle fatigue failure. *Materials science and technology 7*, 5 (1991), 427–440.

[80] Skelton, R., Vilhelmsen, T., and Webster, G. Energy criteria and cumulative damage during fatigue crack growth. *International journal of fatigue 20*, 9 (1998), 641–649.

[81] Smith, K. N. A stress-strain function for the fatigue of metals. *Journal of materials 5* (1970), 767–778.

[82] Tabibian, S., Charkaluk, E., Constantinescu, A., Szmytka, F., and Oudin, A. Tmf–lcf life assessment of a lost foam casting a319 aluminum alloy. *International Journal of Fatigue 53* (2013), 75–81.

[83] Taira, S. Relationship between thermal fatigue and low-cycle fatigue at elevated temperature. In *Fatigue at elevated temperatures*. ASTM International, 1973.

[84] Waltz, R. A., Morales, J. L., Nocedal, J., and Orban, D. An interior algorithm for nonlinear optimization that combines line search and trust region steps. *Mathematical programming 107*, 3 (2006), 391–408.

[85] Wu, X., Quan, G., MacNeil, R., Zhang, Z., Liu, X., and Sloss, C. Thermomechanical fatigue of ductile cast iron and its life prediction. *Metallurgical and Materials Transactions A 46*, 6 (2015), 2530–2543.

Publications of the author related to topic of the thesis

Reviewed papers

[A.1] Bartošák, M., Novotný, C., Španiel, M., Doubrava K. Life assessment of SiMo 4.06 cast iron under LCF and TMF loading conditions. *Materials at High Temperatures* (2018), DOI 10.1080/09603409.2018.1542825.

[A.2] Bartošák, M., Španiel, M., Doubrava K. Thermo-Mechanical Fatigue of SiMo 4.06 Turbocharger Turbine Housing: Damage Operator Approach. Under review in journal *Engineering Failure Analysis*.

[A.3] Bartošák, M., Španiel, M., Doubrava K. FEM Implementation of a unified viscoplastic model and its application to modelling cyclic mechanical behaviour of ductile cast iron under LCF and TMF loading conditions. Under review in journal *Materials at High Temperatures*.

Conference contributions

[A.4] Bartošák, M., Španiel, M., Černý, J. Lifetime calculation for turbine housing of turbocharger under thermo-mechanical loading: damage operator approach. In: *LCF 8, Eighth International Conference on Low Cycle Fatigue*, Dresden: The German Association for Materials Research and Testing, 2017, 93–98. ISBN 978-3-9814516-5-8.

[A.5] Bartošák, M., Španiel, M. Implementation of Unified Viscoplastic Chaboche Model. In: *33rd conference with international participation Computational Mechanics 2017 - Extended Abstracts*, Pilsen: University of West Bohemia, 2017, 5–6. ISBN 978-80-261-0748-4.

[A.6] Bartošák, M., Španiel, M. POST-PROCESSING PROGRAM FOR THERMO-MECHANICAL FATIGUE. In: *21st Workshop of Applied Mechanics - Proceedings*, Praha: České vysoké učení technické v Praze, Fakulta strojní, 2016, 5–8. ISBN 978-80-01-06085-8.

[A.7] Bartošák, M. LIFETIME CALCULATION FOR TURBINE HOUSING OF TURBOCHARGER UNDER THERMOMECHANICAL LOADING. In: *20th Workshop*

of Applied Mechanics - Book of Papers, Praha: České vysoké učení technické v Praze, Fakulta strojní, 2016. ISBN 978-80-01-05975-3.

[A.8] Bartošák, M., Španiel, M. Thermomechanical Fatigue and Creep of Turbine Housing of Turbocharger: Damage Operator Approach. In: *Studentská tvůrčí činnost 2016*, Praha: České vysoké učení technické v Praze, Fakulta strojní, 2016. ISBN 978-80-01-05929-6.

[A.9] Bartošák, M., Španiel, M., Doubrava K., Novotný, C. Isothermal LCF, relaxation and thermomechanical fatigue tests of Si-Mo based cast iron. In: *Experimental Stress Analysis 2016*, Plzeň: Západočeská universita, Fakulta aplikovaných věd, 2016. ISBN 978-80-261-0624-1.

[A.10] Bartošák, M., Španiel, M., Nesládek M. THERMO-MECHANICAL FATIGUE OF SI-MO 4.06 TURBINE HOUSING OF TURBOCHARGER - DAMAGE OPERATOR BASED LIFETIME PREDICTIONS. In: *Engineering Mechanics 2016 - Book of full texts*, Prague: Institute of Thermomechanics, AS CR, v.v.i., 2016, 46–49. ISSN 1805-8248. ISBN 978-80-87012-59-8.

[A.11] Bartošák, M. LOW-CYCLE THERMO-MECHANICAL FATIGUE OF DUCTILE CAST IRON. In: *Workshop of Applied Mechanics 2015 (19-th WAM)*, Praha: České vysoké učení technické v Praze, Fakulta strojní, 2015.

[A.12] Bartošák, M. THERMOMECHANICAL FATIGUE EXPERIMENTS. In: *18th Workshop of Applied Mechanics*, Praha: České vysoké učení technické v Praze, Fakulta strojní, 2015. ISBN 978-80-01-05746-9.

Research reports

[A.13] Španiel, M., Bartošák, M. *Experimentální stanovení Manson-Coffinovy křivky materiálu skříní turbodmychadel.* [Research report]. Praha: ČVUT v Praze, FS, 2014. 12105/2014/27. [in Czech].

[A.14] Bartošák, M., Španiel, M. *Material model for assessment of low-cycle thermomechanical fatigue.* [Research report]. Praha: ČVUT FS, Ústav mechaniky, Odbor pružnosti a pevnosti, 2015. 12105/15/25.

[A.15] Bartošák, M., Španiel, M. *Implementation of material model for low-cycle thermomechanical fatigue.* [Research report]. Praha: ČVUT FS, Ústav mechaniky, Odbor pružnosti a pevnosti, 2016. 12105/16/27.

Functional specimens

[A.16] Španiel, M., Novotný, C., Bartošák, M. *Přípravek pro zkoušky teplotně-mechanické únavy dle Coffina.* [Functional specimen]. 2013.

Software

[A.17] Bartošák, M., Španiel, M. *Software routines for material model of low-cycle thermo-mechanical fatigue in Abaqus FEM software.* [Software]. 2016.

[A.18] Bartošák, M., Španiel, M. *Software routines for material model of low-cycle thermo-mechanical fatigue in Abaqus FEM software. Visco-plastic approximation.* [Software]. 2017.